Hot-electron transport in the spin-valve transistor

Ruud Vlutters

2001

Ph.D. thesis
University of Twente

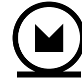

Twente University **Press**

Also available in print:
www.tup.utwente.nl/uk/catalogue/technical/spin-valve

Contents

1	**Introduction**	**3**
1.1	Spin-electronic materials	5
1.2	Spin-electronic devices	7
1.2.1	Spin Valves	7
1.2.2	Magnetic tunnel junctions	8
1.2.3	Spin-Valve Transistor	9
1.3	Spin-electronic applications	10
1.3.1	Magnetic read heads	10
1.3.2	MRAM	11
1.4	Thesis outline	12
1.5	Conclusions	12
2	**Theory of the spin-valve transistor**	**13**
2.1	Electron transport in the emitter and collector	15
2.1.1	Conduction electrons in silicon	15
2.1.2	Schottky diodes	17
2.1.3	Schottky emitter	19
2.1.4	Schottky collector	22
2.2	Electron transport in the metallic base	26
2.2.1	Scattering of Fermi-electrons in a spin valve	26
2.2.2	Hot-electron scattering	28
2.2.3	Hot-electron transport in a spin valve	34
2.2.3.1	The Boltzmann equation in a single layer	34
2.2.3.2	The Boltzmann equation in a magnetic multilayer	38
2.2.3.3	Numerical results	39
2.3	Theory overview: a simple model	43
2.4	Conclusions	46
3	**Experimental procedures**	**49**
3.1	Deposition setup	51
3.2	Spin-valve transistor processing	52
3.3	Electrical transport measurement setup	57
3.4	Conclusions	59
4	**Experimental results**	**61**
4.1	Current transport in Schottky diodes	63
4.2	Hot-electron emission and collection in metal base transistors	65
4.3	Hot-electron transport in the spin-valve transistor	69
4.3.1	Spin-wave scattering in magnetic materials	72
4.3.2	Hot-electron scattering in $Ni_{80}Fe_{20}$	73

4.3.2.1 Spin-dependence of hot-electron scattering in $Ni_{80}Fe_{20}$ at low temperatures 74
4.3.2.2 Thermal hot-electron scattering in $Ni_{80}Fe_{20}$ 79
4.3.3 Hot-electron scattering in Co 81
4.4 Modeling the experimental results 84
4.5 Conclusions 86

5 Conclusion and Recommendations 87
5.1 Conclusions 89
5.2 Recommendations and Discussion 90

Bibliography 93

Appendices 101
A.1 Transport over the Schottky barriers 101
A.1.1 Energy emission spectrum 101
A.1.2 Angular emission spectrum 102
A.1.3 Angular acceptance spectrum 103
A.1.4 Temperature dependent current transfer 106
A.1.4.1 Emission energy-Acceptance cone effects 106
A.1.4.2 Schottky barrier distribution effects 107
A.2 Transport through the base 109
A.2.1 Analytical solution of the 3-D Boltzmann equation 110
A.2.2 Numerical solution of the 3-D Boltzmann equation 111
A.2.3 1-D transport model including spin-wave scattering. 114
A.3 Magnetic switching of a spin valve 116
A.4 Processing schemes 118
A.5 Sample overview 126
A.6 Material parameters 127

Summary 129

Résumé 131

Samenvatting 133

Acknowledgements 135

About the author 137

List of publications 139

Chapter 1

Introduction

Electrons have spin as well as charge, and this may make all the difference in future electronics.

G. A. Prinz [1]

This thesis deals with the hot-electron transport in the spin-valve transistor [2]. This device is a typical example of spin-electronics in which both spin and charge of the electron are essential for its operation.
The spin (σ) is like mass (m_e) and charge (q) an intrinsic property of an electron and can be either up ($\sigma = +1/2\ \hbar$) or down ($\sigma = -1/2\ \hbar$). In most electronic devices, the motion of electrons is only controlled by its charge (Coulomb force), and there are as many spin-up as spin-down electrons that react in exactly the same way on the applied electrical field. In the field of spin-electronics[1], the dynamics and transport of electrons are studied in materials and devices in which the material properties are different for the two types of spin.
Although it was already mentioned in the 1960's [3, 4] that the spin could be used in solid-state devices to control the electron's motion. It finally took until 1988 when it was shown that in multi-layers of alternating Fe and Cr, the electrical resistance is strongly dependent on the magnetic orientation of adjacent Fe layers. The observed effect could be 'easily' explained by the difference in scattering for spin-up and spin-down electrons in the ferromagnetic layers, this is called the giant magnetoresistance (GMR) effect [5, 6].
The discovery of this effect has triggered a search for new materials and devices. In this first chapter a brief overview will be given of the various materials and devices that are used in the field of spin-electronics. At the end of this chapter, the most important applications will be mentioned and an outline of the rest of this thesis will be given.

1.1 Spin-electronic materials

In the field of spin-electronics a wide range of solid-state materials are used, which can be classified into 3 different types based on their electrical conductivity. The metals, with a high conductivity, the semiconductors, in which the conductivity can be controlled over a wide range by impurity doping, and insulators with a very low conductivity.
For a spin-electronic material it is important that there are more spin-up electrons than spin-down electrons. This imbalance results in a magnetic moment (1 uncompensated spin results in 1 Bohr magneton), this is why many magnetic materials can be used in spin-electronics. The degree of imbalance is expressed in the polarization [7, 8], which is defined as the difference in number of spin-up electrons minus the number of spin-down electrons divided by the total number of electrons.

1 Sometimes, this field is also called magneto-electronics, but this refers to the field where magnetic elements are included into the electronics . In this field there is not necessarily a difference between the transport mechanisms of spin-up and down electrons.

- Metals
  In metallic materials, electrons are shared between the different atoms in a conduction band which has its minimum under the Fermi level extending to above it. Because electrons at the Fermi level can easily find new empty states this results in a high electrical conductivity. In most metals there are as many spin-up as down electrons with identical properties for the two types of spin, so for spin-electronics these are less interesting.
  In the ferromagnetic transition metals (Fe, Co and Ni and their alloys) the 3d conduction bands are exchange splitted and filled up to the Fermi level. This results in more spin-up electrons (also called the majority electrons) than spin-down electrons (minority electrons) and this imbalance make these materials magnetic. Because these 3d bands are hybridized with the s-bands, these bands can influence the electrical conductivity. These materials are often used in spin-electronic applications.
  In the rare-earth magnetic materials (Gd, Tb, Dy, etc.), a quite similar splitting of the 4f bands results into magnetism, but these bands are highly localized, and so can't contribute directly to the conductivity. The electrical conductivity in these materials is due to the electrons in the 5d and 6s bands, that become slightly polarized by the 4f electrons, and so the electrical conduction is slightly different for spin-up and down electrons. Due to this small difference in transport properties for the different spins, these materials are limited in their use for spin-electronics.
  Very interesting for spin-electronics are the half-metallic ferromagnets, like for example CrO_2 [9] and Fe_3O_4, NiMnSb and PtMnSb [10]. In these materials there are only conduction bands around the Fermi level for spin-up electrons and not for spin-down. This results in 100% polarization of the conduction electrons, but experimentally these materials are not easily fabricated and only a small fraction of impurities or growth defects can destroy the 100% polarization.
  Furthermore, there are the materials that show colossal magneto resistance (CMR), like the perovskite: $La_{0.7}Sr_{0.3}MnO_3$ (LSMO), the double perovskite: Sr_2FeMoO_6 [11] or the perochloride: $Tl_2Mn_2O_7$ [12] in which below the Curie temperature, the current transport is largely influenced by the relative orientations between the magnetization of the various magnetic atoms. Although the resistance of these materials can change over several orders of magnitude, their low Curie temperature (often below 250K) and high saturation fields (several Tesla) make these materials unpractical.
  Although the metals Ag, Au, Cr, Cu and Ru aren't magnetic, these materials are often used as spacer between ferromagnetic layers. With these materials, ferromagnetic layers can be coupled in an anti-ferromagnetic way, as in the case of Fe/Cr multilayers with the invention of GMR. But one can also uncouple two magnetic layers with different switching properties while maintaining the GMR effect, as done in spin valves.

- Semiconductors
  In intrinsic semiconductor materials (like pure Si, Ge or GaAs) there exists a

valence band below the Fermi level in which all electrons are (at T=0K), and an empty conduction band which is above the Fermi level with a bandgap of roughly less than 3eV between the valence and conduction band. At room temperature electrons are thermally excited into the conduction band, resulting in the typical increase of conductivity with higher temperatures. By doping these materials, electrons can be taken from the valence band, resulting in holes (p-type), or electrons can be added to the conduction band (n-type). Furthermore, this doping can be done very controllably and locally, by which p/n diodes and transistors can be made, the building blocks of modern integrated circuits (IC's). Furthermore, there exist also ferromagnetic semiconductors, like the III-V semiconductors GaAs, InAs or GaSb, which are doped with Mn [13]. In these magnetic semiconductors, Mn acts as magnetic p-type dopant, and a long range coupling [14, 15] results in a ferromagnetic ground state with a Curie temperature upto $\approx$ 110K. Furthermore, it appears to be possible to make spin valves [16] and magnetic tunnel junctions [17] with these materials.

- Insulators
  These materials are like semiconductors, but their bandgap is larger than $\approx$ 3eV, and due to this, almost no electrons are thermally excited into the conduction band, resulting in a low conductivity. Furthermore, electron transport through very thin layers (several Å's, 1Å$\equiv 1 \cdot 10^{-10}$m) of insulator material can be by quantum mechanical tunnelling [18], a mechanism that is sensitive to the density of states near the Fermi level. By sandwiching an insulator between two ferromagnetic contacts, this tunnelling becomes spin-dependent, as will be shown in the next section.

1.2 Spin-electronic devices

In order to exploit the spin-dependent effects, it is often needed to make stacks of different spin-electronic materials, because the current outside the spin-electronic device has as many spin-up as spin-down electrons. So first electrons have to be polarized, which is done in a first magnetic layer and after that, these polarized electrons are analyzed by a second magnetic layer. By measuring the current through the device, the relative orientation between polarizer and analyzer can be determined. This relative orientation can often be controlled by a magnetic field, so that the device can work as a magnetic field sensor.
All the devices that will be mentioned in this section work on the above principle. First, we explain a normal spin valve, which is based on the GMR effect. Next, the principles behind the magnetic tunnel junction and the spin-valve transistor are briefly discussed.

1.2.1 Spin Valves

In these devices two ferromagnetic layers with different magnetic switching properties are separated by a non-magnetic layer that decouples the two magnetic layers

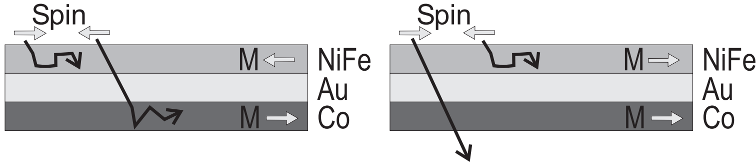

Figure 1.1: *The two magnetic states of a spin-valve. On the left is the anti-parallel state resulting in a high resistance, and on the right the parallel state with a lower resistance.*

(as for example, the NiFe/Au/Co layers in Fig. 1.1). By applying a magnetic field, the two magnetic layers respond 'independently' and switch at a different switching field. In this way, the relative magnetic orientation between the two magnetic layers can be controlled between the parallel and the anti-parallel state.
These two states have a different electrical resistance, because in the ferromagnetic layers and at the magnetic/non-magnetic interfaces, the electron transport is spin-dependent. Electrons with their spin aligned to the ferromagnet's magnetization (the majority electrons) scatter less than electrons (minority) with their spin opposite to it, this is called the GMR effect [5, 6]. This difference in scattering for the two types of spin results in a high resistive state (R^{AP}) when the two magnetic layers are magnetized anti-parallel, because both types of spin do scatter a lot. When a high enough magnetic field is applied to switch both layers, the parallel state is obtained and a lower resistance (R^{P}) is measured, because electrons with their spin aligned to both magnetic layers can now travel through the stack while having a much lower scattering probability. The relative change in resistance ($= (R^{AP} - R^{P})/R^{P}$), also called the magnetoresistance, can be up to 19% [19] in well engineered spin valves.
The current inside a spin valve can be in two principle directions. The Current can be In the Plane of the layers (CIP) or Perpendicular to the Plane (CPP). In applications, like magnetic field sensors the CIP geometry is generally used, because it can be measured easily by two or four point contacts several μm-mm's apart. Measuring in the CPP geometry is much more cumbersome due to the low resistance [20] of a thin metallic stack (typical thickness $\approx$ 30-100nm), but the magnetoresistance is higher in the CPP geometry, because all electrons have to pass through all magnetic layers and no shunting through the non-magnetic layers can happen. So many different methods were investigated and reported in literature on how to measure the CPP magnetoresistance [21], but until now there are few that can work at room temperature [22].

1.2.2 Magnetic tunnel junctions

In a magnetic tunnel junction [23, 24], as shown schematically in Fig. 1.2, there are also two magnetic layers with different magnetic switching properties, like in spin valves. But these two magnetic layers are separated by a very thin oxide layer ($\approx$ 10-20Å), through which a current is driven in a perpendicular fashion. The possibility to make this oxide layer so thin without pinholes by in-situ plasma oxidation of Al [25, 26] has triggered research all over the world on these devices.

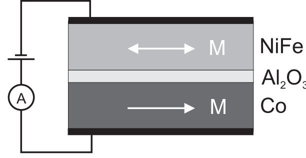

Figure 1.2: *The schematic structure of a magnetic tunnel junction, which consists of two magnetic contacts (NiFe and Co) with different switching fields and a tunnel barrier of* Al_2O_3.

The electron transport through the insulator is by quantum mechanical tunnelling, a mechanism that conserves spin and that depends on the number of filled states on one side of the insulator and the number of empty states to tunnel into on the other side. Because ferromagnetic materials are used, these filled and empty states are different for the spin-up and down electrons, and so the total tunnelling current will be different when the electrodes are magnetized parallel or anti-parallel, resulting in a tunnelling magnetoresistance (TMR). The sign of the TMR can be either positive or negative based on the combination of tunnelbarrier materials and magnetic layers [27]. This is most probably related to which conduction bands (s, p or even d) contribute to the tunnelling current and what are the exact interface density of states.
Because the quantum mechanical tunnelling probability from one electrode to the other reduces exponentially with increasing separation, the resistance of a tunnel junction is very sensitive to the barrier thickness. Although the TMR can be upto +50%, spin valves are still used in magnetic read heads, because they have a lower resistance, and so a lower resistance noise resulting in a better signal to noise ratio. But for MRAM applications, as will be explained in the next section, these tunnel junctions are ideally suited due to their perpendicular current flow, making a higher integration possible.

1.2.3 Spin-Valve Transistor

The spin-valve transistor (SVT, [2]) is a 3-terminal device that consists of a spin valve layer which is sandwiched between two semiconductors (see Fig. 1.3). Due to this hybrid structure, it is possible to inject electrons perpendicular through the spin valve and measure the traversing (collector) current at room temperature [28, 29]. Electrons are injected from the silicon emitter into the spin valve over a Schottky diode of 0.9eV (Si/Pt). This results in *hot*-electrons with an excess energy (above the Fermi-level) of $\approx$ 0.9eV in the base. Only electrons that arrive at the collector with enough energy and the right momentum can finally come over the Schottky barrier of 0.8eV (Au/Si) and contribute to the collector current. This makes the collector current very sensitive to scattering in the base.
Like in a normal spin valve, the magnetic layers in the base can be in the parallel or anti-parallel state. For a constant emitter current, the collector current in the parallel state (I_c^P) is higher than in the anti-parallel state (I_c^{AP}), and this is due to the spin-dependent scattering in the magnetic layers. The relative change in collector current is expressed by the magnetocurrent (MC$\equiv (I_c^P - I_c^{AP})/I_c^{AP}$) and can be huge (up to

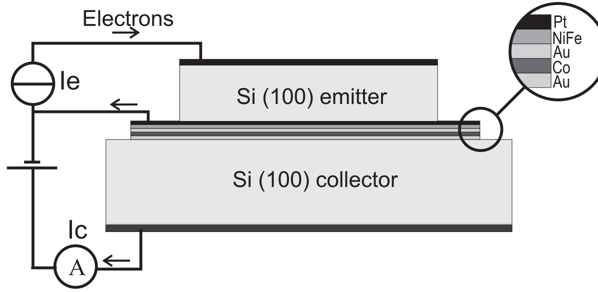

Figure 1.3: *The schematic structure of a spin-valve transistoris made of a silicon emitter and collector and a Pt/NiFe/Au/Co/Au base.*

several hundred %). This makes the spin-valve transistor a very promising device for sensor applications, although the absolute collector current is low.
Using a Schottky barrier on the emitter side is not the only way to obtain hot-electrons, by using a ballistic electron emission microscope (BEEM) [30, 31], by using polarized electrons emitted from a GaAs source [32] or by using a tunnel junction [33, 34] one can also obtain hot-electrons, and this has been proven to result in the same high values of the magnetocurrent.

1.3 Spin-electronic applications

Spin-electronic materials and devices can be used in various applications [35], which can all be divided into two groups. Those in which the device is used as a sensor of magnetic fields, like position and rotation sensors [36] and of course the magnetic read heads inside a hard disk. And those in which the parallel and anti-parallel state of a spin valve are used to represent a logical 0 or 1. With this method it is possible to make solid-state memory devices and logical circuits [37]. Below we will briefly show the most important application, the magnetic read head, and one of the most promising applications, the magnetic random access memory (MRAM).

1.3.1 Magnetic read heads

One of the most demanding applications in terms of magnetic field detection is the reading of data from a magnetic hard disk. Data is stored in transitions, that is where the magnetization of the medium reverses [38]. At these transitions, magnetic strayfields emerge from the storage medium and can be picked up by the read head. By increasing the storage density over the last 40 years, the size of a transition has become very small, and also the thereby belonging strayfields. In order to measure these small magnetic fields, spin valves are used today, and recently densities of upto 35Gbit/inch^2 were reported in a laboratorium demonstrator [39]. It is expected that further improvements in the read/write heads [40], electronics [41], storage media and drive mechanics can finally result into areal densities in excess of 100-150Gbit/inch^2,

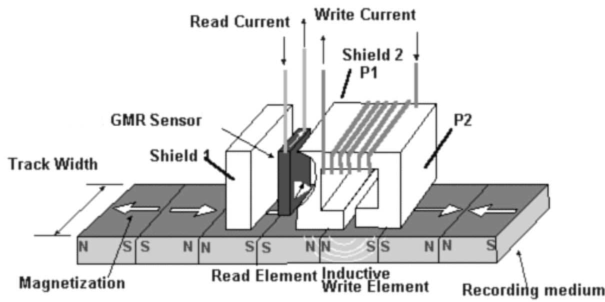

Figure 1.4: *A schematic view of a integrated read/write head above a recording medium as can be found inside a hard disk [39].*

above this there are serious problems with the thermal stability of the magnetic domains, known as the superparamagnetic limit.

1.3.2 MRAM

A new application for spin valves and magnetic tunnel junctions is the Magnetic Random Access Memory (MRAM, see Fig. 1.5, [42]). A single spin valve or MTJ can represents a 1 when it is magnetized parallel or a 0 when anti-parallel. By making an array of these elements and by connecting them in an appropriate way, every cell can be addressed individually. Data can be read by applying a small current (I) through the selected element, as shown in Fig. 1.5 and by measuring the resistance of that cell. Data can be written with a magnetic field that is created by a higher write current in both the word- and bitline that intersect each other above/below the selected cell, resulting in a locally strong enough field to switch the underlying magnetic element. Although no commercial MRAM's with several megabytes of storage can be bought today, it has the potential to become the main memory element in future electronics [44], because it is non-volatile, it has fast access times, and can be fully integrated with other CMOS circuitry. A weak point might be its price per bit, because its based on the same expensive lithography technology, as CMOS does.

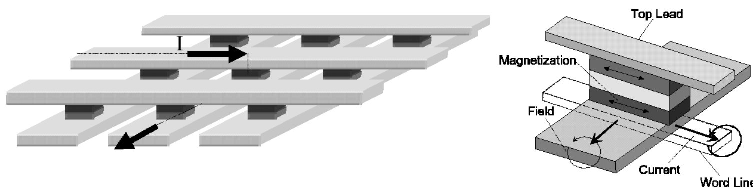

Figure 1.5: *In an MRAM a matrix of magnetic tunnel junctions are connected in such a way that a single element can be addressed as shown on the left. Every element of the matrix consists of a MTJ as shown on the right [43].*

1.4 Thesis outline

Now a brief overview over the large field of spin-electronics and its applications has been given, the rest of this thesis will focus on the electron transport in the spin-valve transistor. In the next chapter we will theoretically analyze the current transport over Schottky barriers and model the transport of hot-electrons through the base. Next, in chapter 3, the experimental procedures to make and characterize the spin-valve transistor are explained. This includes all the processing schemes to obtain two silicon wafers with a spin valve in between and how these are processed into spin-valve transistors. In the experimental results chapter, different aspects of the spin-valve transistor are compared with theory and from these analyzes, physical quantities relevant for the electron transport will be extracted. Finally in the last chapter, the conclusions will be drawn and recommendations on how to improve the spin-valve transistor will be given.

1.5 Conclusions

The motion of electrons cannot only be controlled by its charge, but also by its spin, this is done in the field of spin-electronics. There are many different materials that are used, in which it is important that the electrical properties are different for spin-up and spin-down electrons. With these materials, devices can be made, of which spin valves and magnetic tunnel junctions are the most widely known. The first is based on the spin-dependent scattering in ferromagnetic transition metals and the second on spin-dependent tunneling through an insulating barrier. Also the spin-valve transistor is based on spin-dependent scattering, but due to the combination of metals with semiconductors, hot-electrons are involved. These devices can be applied in many different products where magnetic fields should be measured and one can even make solid-state memories with them.

Chapter 2

Theory of the spin-valve transistor

As explained in the introduction, the spin-valve transistor (SVT) has an emitter and collector made of semiconducting material with in between a base consisting of a metallic spin valve (as shown in Fig. 1.3). From the emitter side, electrons are injected (I_e) into the base over a Schottky barrier. This results in hot-electrons with an excess energy of ≈ 1.0 eV, that scatter in the base dependent on their spin. When the electrons arrive at the collector, only those electrons with enough energy and the right momentum can pass the collector Schottky barrier and contribute to the collector current (I_c). This filtering makes the collector current a sensitive function of the scattering in the base and is one of the reasons why such a high magnetocurrent is observed.

In this chapter we describe the underlying theory of electron transport over metal/semiconductor (especially silicon) contacts and the hot-electron transport through a metallic spin-valve layer. With this theory it becomes clear why hot-electrons are injected from the Schottky diode. It explains the specific collection properties and how this results in a collector current that is extremely sensitive to scattering in the base. Finally we discuss the possible hot-electron scattering mechanisms, and present a model that describes the spin-dependent current transport through the base.

With the theory below, more insight in the electron transport in the SVT is gained, and experimental results can be understood. By comparing theory and experiment, fundamental parameters describing the hot-electron transport can be extracted. Furthermore, it shows which parameters can be changed to optimize device operation.

2.1 Electron transport in the emitter and collector

In this theory section, the basic properties of conduction electrons in silicon are discussed, after which the current transport over Schottky diodes is described. These Schottky diodes serve as emitter and collector of the spin-valve transistor. At the emitter, we analyze the hot-electron emission characteristics (energy and momentum distribution) and at the collector we analyze what momentum and energy is needed to pass over the collector barrier and contribute to the collector current.

2.1.1 Conduction electrons in silicon

In the spin-valve transistor, both emitter and collector are made of silicon. Although this can in principle be any type of semiconductor [1], we have focussed on silicon because this semiconductor is widely used in industry and readily available. Silicon is a semiconductor with the diamond structure and a lattice constant of 5.43Å.

1 As long as the electron transport remains by thermionic emission over the Schottky barrier, it can be used in the spin-valve transistor, for example it has been proven that the SVT works also with Ge [45] and GaAs [46].

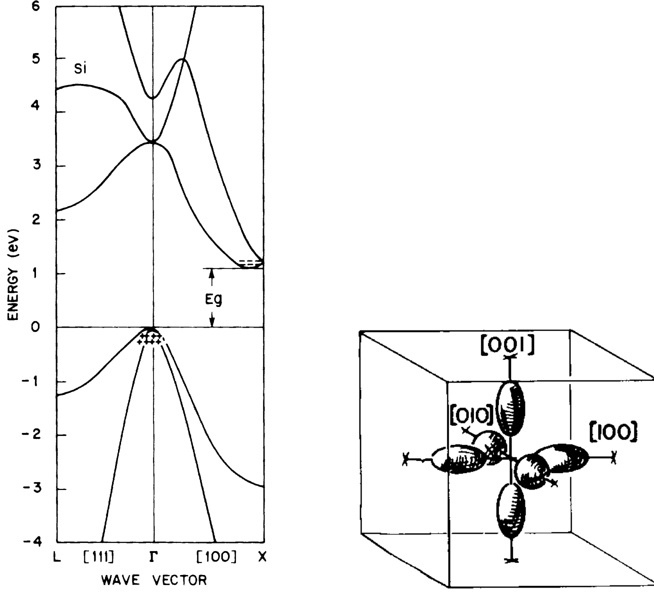

Figure 2.1: *On the left the energy bands in silicon are shown and on the right the constant energy ellipsoids in k-space around the 6 minima in the conduction band.*

Between the valance and the conduction band there is an indirect band gap (E_g) of 1.12eV at room temperature (see Fig. 2.1). In the conduction band there are 6 ($= M_c$) minima at an energy E_C on the positive and negative x, y and z axes in k-space. Around these minima the electron motion can be described by a free electron model, with an effective mass defined as:

$$\frac{1}{m^*_{ij}} \equiv \frac{1}{\hbar^2} \frac{\partial^2 E(k)}{\partial k_i \partial k_j} \tag{2.1}$$

In the case of silicon two different effective electron masses can be defined, the longitudinal mass ($m^*_l = 0.98 m_0$) for electrons with their k-vector in the same direction as the position of the corresponding minimum and the transversal mass ($m^*_t = 0.19 m_0$) for electrons with their k-vector perpendicular to this longitudinal direction. In many calculations the more simple isotropic mass is taken, which is defined as: $m^* = (m^*_l m^{*2}_t)^{1/3} = 0.33 m_0$. In order to calculate how many electrons there are in the conduction band of undoped silicon, we have to calculate how the electrons are distributed (energy and momentum) and fill the possible states. The energy distribution of the electrons is given by the Fermi-Dirac distribution:

$$F(E) = \frac{1}{1 + \exp\left(\frac{E - E_F}{kT}\right)} \tag{2.2}$$

When $(E - E_F) > 3kT$ this distribution can be approximated by:

$$\exp\left(-\frac{(E - E_F)}{kT}\right) \tag{2.3}$$

The density of states in the 6 parabolic bands is given by:

$$N(E) = M_c \frac{4\pi \left(E - E_C\right)^{1/2}}{h^3} \left(2m^*\right)^{3/2} \tag{2.4}$$

In order to calculate the total number of electrons (n) in the conduction band, we have to multiply the distribution function with the density of states and integrate them from the bottom of the conduction band upward, resulting in:

$$n = N_C \exp\left(-\frac{E_C - E_F}{kT}\right) \qquad N_C \equiv 2\left(\frac{2\pi m^* kT}{h^2}\right)^{3/2} M_c \tag{2.5}$$

By doping silicon with atoms with a higher valency (like P, As and Sb) electrons can be added to the conduction band and the silicon becomes n-type. Doping with atoms with a lower valency (like B, Ga and In) results in a not completely filled valence band, called holes, and the silicon becomes p-type. The difference between undoped and doped silicon is the position of the Fermi level. In the case of n-type doping, electrons are added to the conduction band (adding to Eq. 2.5) and this can be seen as like the Fermi level moves closer to the conduction band. When the doping concentration N_D is much larger than N_C, the energy difference qV_n between the Fermi level and the minimum of the conduction band can be written as:

$$qV_n = E_C - E_F = -kT \ln\left(\frac{N_D}{N_C}\right). \tag{2.6}$$

In the valence band a missing electron, called a hole, can be seen as free with a valence band minimum at k=0, but dependent on the band it is in, it can be a light or heavy hole (with the corresponding $m^*_{lh} = 0.16m_0$ and $m^*_{hh} = 0.49m_0$).
For the Schottky diodes in the transistor we only use n-type silicon, with a doping of $N_D \simeq 10^{16}cm^{-3}$ for the Schottky barriers and a doping of $N_D \simeq 10^{21}cm^{-3}$ for the ohmic contacts (see [47]).

2.1.2 Schottky diodes

By contacting a metal to a semiconductor, like the emitter and collector contact with the base in the spin-valve transistor, a Schottky diode is formed.
When a metal is brought in intimate contact with an n-type semiconductor, the Fermi levels of the two materials will align when no external voltage is applied. Because the conduction bands in a semiconductor are above the Fermi level, the electrons can fall into the lower conduction bands of the metal, which are below the Fermi level. This results in a depletion of charge carriers in the semiconductor, bending the conduction band upwards (resulting in a bandbending of qV_{bi}) and creating a Schottky barrier, as can be seen in Fig. 2.2. This barrier will increase up to a dynamic equilibrium value, where electrons moving from the semiconductor to the metal are exactly in equilibrium with the electrons moving from the metal back into the semiconductor. The value of the barrier height ($q\Phi_B$) is dependent on the type of semiconductor and the metal, in Appendix A.6 (page 127) an overview of these barrier heights on Si, Ge and GaAs

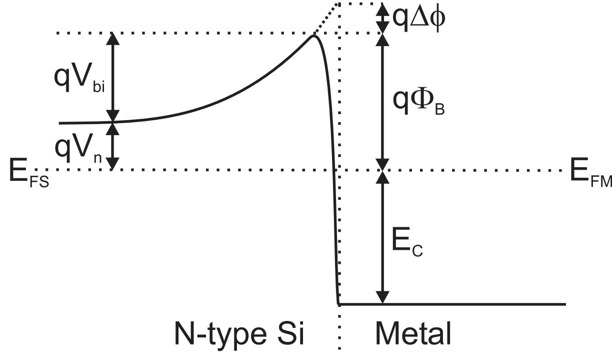

Figure 2.2: *A schematic energy diagram of the conduction band minimum (solid line) in a Schottky barrier (with the image force lowering $q\Delta\phi$).*

is given. Due to the image-force effect [47], the maximum of the Schottky barrier is inside the semiconductor, at a distance x_m ≈10Å and a hugh electrical field in the order of $E_{image} \approx 10^9 V/m$ exists between the maximum of the Schottky barrier and the physical metal/silicon interface.
When a positive voltage (V) is applied over the Schottky barrier, the Fermi level in the silicon becomes higher than in the metal ($E_{FS} = E_{FM} + qV$) and the bandbending reduces to $q(V_{bi} - V)$ (but $q\Phi_B$ and qV_n remain almost constant, see Fig. 2.3). In order to calculate the resulting current density from the silicon into the metal ($J_{s\rightarrow m}$), we apply the thermionic-emission theory [47] in which we have to integrate the current contribution of a single electron over the number of electrons that have enough velocity in the x-direction to overcome the bandbending, so:

$$J_{s\rightarrow m} = \int_{v_x > v_{\min}} q v_x dn \tag{2.7}$$

with the minimum velocity above which the electrons can contribute to $J_{s\rightarrow m}$ as:

$$v_{min} = \sqrt{\frac{2q}{m^*}(V_{bi} - V)} = \sqrt{\frac{2q}{m^*}(\Phi_B - V_n - V)} \tag{2.8}$$

To calculate dn, the distribution function (Eq. 2.2) has to be multiplied by the density of states (Eq. 2.4) in which the kinetic energy ($E - E_C$) has to be written with velocities (i.e. v_x, v_y and v_z), so:

$$dn = 2(\frac{m^*}{h})^3 \exp(-\frac{qV_n}{kT}) \exp(-\frac{\frac{1}{2}m^*(v_x^2 + v_y^2 + v_z^2)}{kT}) dv_x dv_y dv_z \tag{2.9}$$

Resulting in:

$$\begin{aligned} J_{s\rightarrow m} = &\left[2q(\frac{m^*}{h})^3 \exp(-\frac{qV_n}{kT})\right] \int_{v_{\min}}^{\infty} v_x \exp(-\frac{\frac{1}{2}m^* v_x^2}{kT}) dv_x \times \\ &\int_{-\infty}^{\infty} \exp(-\frac{\frac{1}{2}m^* v_y^2}{kT}) dv_y \times \int_{-\infty}^{\infty} \exp(-\frac{\frac{1}{2}m^* v_z^2}{kT}) dv_z \end{aligned} \tag{2.10}$$

By calculating these integrals $J_{s\rightarrow m}$ becomes:

$$J_{s\rightarrow m} = \left[\frac{4\pi q m^* k^2}{h^3}\right] T^2 \exp(-\frac{q\Phi_B}{kT}) \exp(\frac{qV}{kT}) \tag{2.11}$$

The current density from the metal into the semiconductor ($J_{m\rightarrow s}$) is independent of the applied voltage (without taking the slight barrier lowering due to the image force effect into account) and equal to $J_{s\rightarrow m}$ at zero bias, so the total current density through the diode is:

$$J = J_{s\rightarrow m} - J_{m\rightarrow s} = \left[\frac{4\pi q m^* k^2}{h^3}\right] T^2 \exp(-\frac{q\Phi_B}{kT}) \left(\exp(\frac{qV}{kT}) - 1\right) \tag{2.12}$$

In the above calculation we have taken the density of states in only one minimum of the conduction band and used an isotropic mass in all 3 directions. This is correct in the case of GaAs, but in silicon all 6 minima contribute and the effective mass is different in the different directions. A detailed calculation of the integrals like 2.10 for all the 6 minima with their corresponding effective masses was done by Crowell in 1965 [48]. As found by these calculations, we can easily compensate Eq. 2.12 by taking a different Richardson constant (the term in square brackets in 2.12). For Si(100) and Si(111) we have to use:

$$A^*_{Si(100)} = \frac{\left(2m_t^* + 4(m_l^* m_t^*)^{1/2}\right)}{m_0} \left[\frac{4\pi q m_0 k^2}{h^3}\right] = 252\ A/cm^2/K^2 \tag{2.13}$$

$$A^*_{Si(111)} = \frac{6}{m_0} \left(\frac{(m_t^*)^2 + 2(m_l^* m_t^*)}{3}\right)^{1/2} \left[\frac{4\pi q m_0 k^2}{h^3}\right] = 264\ A/cm^2/K^2 \tag{2.14}$$

But in experiments a lower Richardson constants is observed, which can be explained by the more complicated thermionic-emission/diffusion theory [47, 49]. In this theory, back-scattering due to optical-phonons reduces the effective net current over the Schottky barrier and is included by a reduction of the Richardson constant with f_p. Furthermore, the effect of quantum mechanical reflection on the Schottky barrier is taken into account, reducing the Richardson constant with f_Q. Finally this results in a total Schottky current density of:

$$\boxed{J_{Schottky} = A^{**} T^2 \exp(-\frac{q\Phi_B}{kT}) \left[\exp(\frac{qV}{kT}) - 1\right]} \tag{2.15}$$

with an effective Richardson constant for Si of:

$$A^{**}_{Si} = f_p f_Q A^*_{Si} \approx 110\ A/cm^2/K^2 \tag{2.16}$$

2.1.3 Schottky emitter

The Schottky diode current, like explained in the previous section, is calculated by determining how many electrons in the silicon have enough velocity to overcome

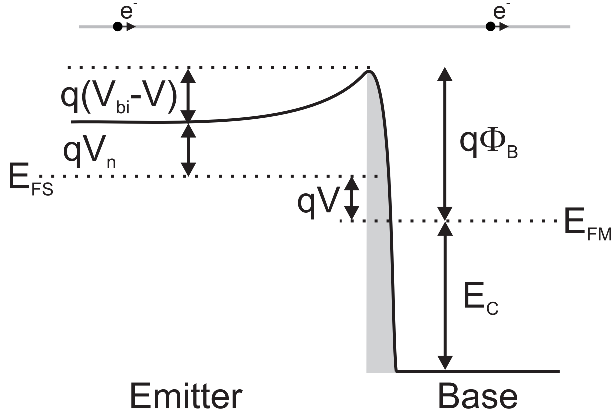

Figure 2.3: *The schematic conduction band minimum in a forward biased Schottky diode, like used as the emitter of the spin-valve transistor.*

the internal bandbending barrier $q(V_{bi} - V)$. In order to determine the emission properties of a Schottky barrier, it is essential to take these electrons and describe their velocity and energy behavior in the small region after the maximum in the conduction band (at x_m) in the silicon and how these electrons propagate into the metal.
Based on energy conservation, electrons that are emitted from the silicon, will have excess energy in the metallic base (see Fig. 2.3, see for other methods to obtain hot-electrons: [50]). These so-called hot-electrons will not all have exactly the same energy. In order to obtain the precise energy distribution, equation 2.10 can be rewritten after which we integrate over only electrons within a certain energy interval. The exact derivation is done in Appendix A.1.1 (page 101), and results in:

$$J_e(E) = \left[\left(\frac{A^* q}{k^2} \right) (E - \Phi_B) \exp\left(-\frac{qE}{kT} \right) \right] \exp\left(\frac{qV}{kT} \right) \tag{2.17}$$

The term between square brackets in 2.17 determines the shape of the emission spectrum, and the last term does the 'scaling' for the applied voltage. The emission curve becomes broader (as shown in Fig. 2.4) at higher temperatures, due to the broader Fermi-Dirac distribution like expected.
Furthermore, the electrons that are injected into the base have most of their velocity in the x-direction and only little in the y- and z-direction. This is because the electrical field in the silicon near the interface (in the gray region of Fig. 2.3) only accelerates the electrons in the x-direction. In order to determine the angle within all electrons are emitted, we assume there is no scattering and a free-electron model with isotropic electron mass can be applied to both the silicon and the metallic base. The velocity of the emitted electrons in the metal (v_{mx}, v_{my} and v_{mz}) can then be related to their initial velocity in the semiconductor (v_{sx}, v_{sy} and v_{sz}) and the angle within which the electrons are injected can be calculated.
Assuming that the parallel momentum is conserved [51] at the silicon-metal interface,

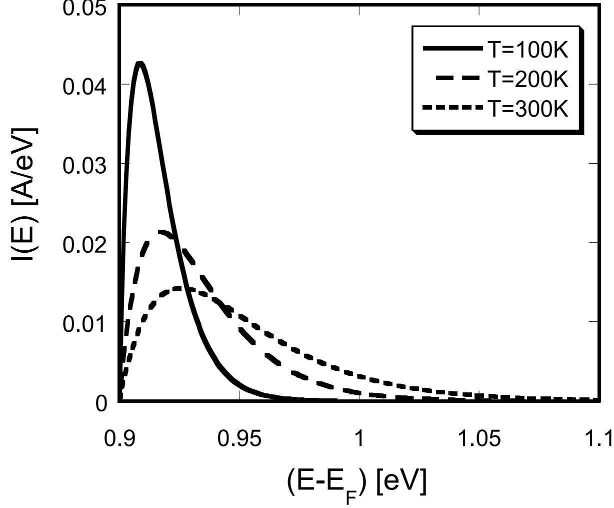

Figure 2.4: *The energy spectrum of the emitted hot-electrons from a Schottky diode with a barrier height ($q\Phi_B$) of 0.9eV for 3 different temperatures while injecting 2mA of current.*

we can write:

$$\begin{aligned} m_{si}^{*} v_{sy} &= m_{m}^{*} v_{my} \\ m_{si}^{*} v_{sz} &= m_{m}^{*} v_{mz} \end{aligned} \tag{2.18}$$

Based on total energy conservation, the sum of potential and kinetic energy has to remain equal while an electron travels from the maximum of the Schottky barrier into the metal (like the schematic electron drawn in Fig. 2.3). So the total energy E compared to the Fermi-level in the metal can be written as:

$$E = \frac{1}{2} m_{si}^{*} v_{sx}^{2} + \frac{1}{2} m_{si}^{*} (v_{sy}^{2} + v_{sz}^{2}) + q\Phi_B = \frac{1}{2} m_{m}^{*} v_{mx}^{2} + \frac{1}{2} m_{m}^{*} (v_{my}^{2} + v_{mz}^{2}) - E_C \tag{2.19}$$

Now it is quite easy to calculate the maximum angle (θ_e) under which an electron with energy E can be emitted into the metal, because these electrons have a maximum amount of velocity in the y- and z-direction while having just enough velocity in order to get over the Schottky barrier, so at the maximum of the Schottky barrier their x-velocity is near 0 ($v_{sx} \approx 0$):

$$\sin(\theta_e)^2 = \frac{v_{my}^{2} + v_{mz}^{2}}{v_{mx}^{2} + v_{my}^{2} + v_{mz}^{2}} = \frac{m_{si}^{*}}{m_{m}^{*}} \left(\frac{E - q\Phi_B}{E + E_C} \right) \tag{2.20}$$

As shown in Fig. 2.5, the emission cone is only several degree and the higher the barrier, the narrower the emission cone. Furthermore, the choice of the contact metal can influence the emission cone angle quite drastically, because not only changes this the Schottky barrier height, but also the much larger energy difference between the conduction band and the Fermi level in the metal (E_C=5.5eV for Au).

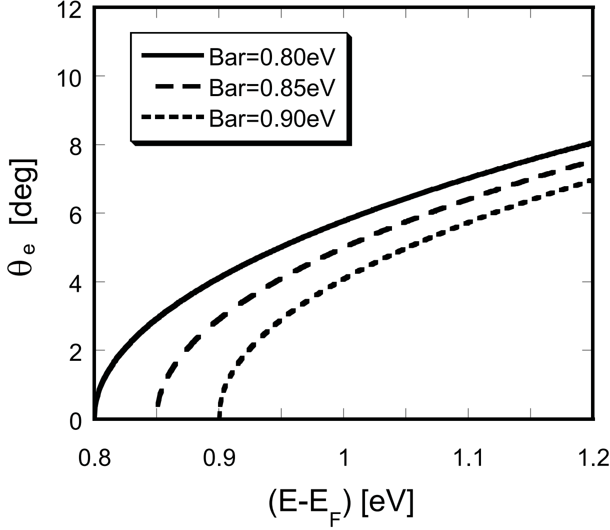

Figure 2.5: *The emission cone angle θ_e for 3 different Schottky barriers, as a function of the energy of the emitted electrons ($q\Phi_B = 0.80, 0.85, 0.9eV$, $E_C = 5.5eV$).*

In Appendix A.1.2 (page 102), a more thorough treatment of the angular distribution is show, in which the current integral (Eq. 2.10) is transformed from an integral over the velocities in the semiconductor to an integral over the velocities in the metal, after which the exact angular dependence of the emitted electrons can be obtained. The results of these calculations will be used as boundary conditions for the transport calculations in the base.
In the above theory no scattering was taken into account. Electrons which are over the maximum of the Schottky barrier can scatter inside the silicon with a phonon after which the electron doesn't have enough energy anymore. Crowell and Sze have analyzed this emitter efficiency [52] with a detailed calculation of the mean free path due to optical-phonon–electron scattering in silicon for electrons with some excess energy (several 0.1eV's). Resulting in an almost constant efficiency of about 90% ($= \alpha_e^{phonon}$).
Electrons can also scatter on the silicon-metal interface, so that their parallel momentum is not conserved anymore, in this case the electrons are injected in a much broader angle.

2.1.4 Schottky collector

When an electron has passed through the base it should be able to get into the collector. Due to the properties of the collector only electrons with enough energy and with the right momentum can be collected, as will be shown below.
As in the emitter, the total energy of an electron moving from the base into the collector is conserved. The potential and kinetic energy relative to the Fermi-level in the

base and at the maximum of Schottky barrier can be written as:

$$E = \frac{1}{2}m_m^* \left(v_{mx}^2 + v_{my}^2 + v_{mz}^2\right) - E_C = \frac{1}{2}m_{si}^* \left(v_{sx}^2 + v_{sy}^2 + v_{sz}^2\right) + q\Phi_B \tag{2.21}$$

and also in this case we assume that parallel momentum is conserved:

$$\begin{aligned} m_m^* v_{my} &= m_{si}^* v_{sy} \\ m_m^* v_{mz} &= m_{si}^* v_{sz} \end{aligned} \tag{2.22}$$

We can now calculate the velocity of an electron at the maximum of the Schottky barrier based on its initial velocity in the metal (v_{mx}, v_{my} and v_{mz}):

$$v_{sx} = \sqrt{\frac{m_m^*}{m_{si}^*}\left[v_{mx}^2 - \left(\frac{m_m^*}{m_{si}^*} - 1\right)\left(v_{my}^2 + v_{mz}^2\right)\right] - \frac{2}{m_{si}^*}\left[E_C + q\Phi_B\right]} \tag{2.23}$$

In order to overcome the barrier, there should remain some positive velocity in the x-direction, otherwise the electron will bounce back into the base (classical reflection). Similar to the emitter, this result in a maximum incidence angle up to where an electron with energy E can be collected, this acceptance cone angle is:

$$\sin(\theta_c)^2 = \frac{v_{my}^2 + v_{mz}^2}{v_{mx}^2 + v_{my}^2 + v_{mz}^2} = \frac{m_{si}^*}{m_m^*}\left(\frac{E - q\Phi_B}{E + E_C}\right) \tag{2.24}$$

So exactly the same as Eq. 2.20. This means that, when the collector barrier is below the emitter barrier (and both have the same E_C), all the emitted electrons can be collected, as long as they have not scattered in the base or in the grey zones of Fig. 2.3 and 2.6. Furthermore, this means that the higher the hot-electron energy is, the larger the acceptance cone.

Although not directly apparent from the above model, there is a difference in a collector made from silicon (100) and silicon (111), which could be understood when we

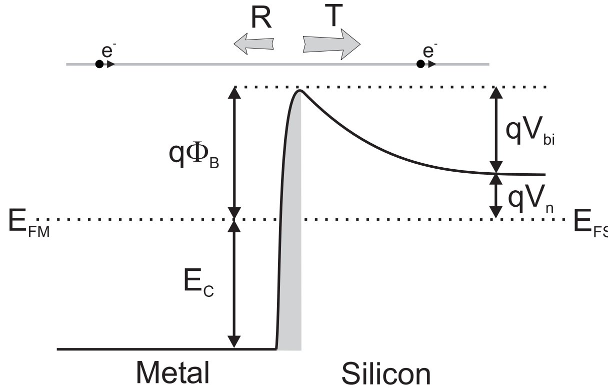

Figure 2.6: *The schematic conduction band minimum for a hot-electron at the collector side of the spin-valve transistor.*

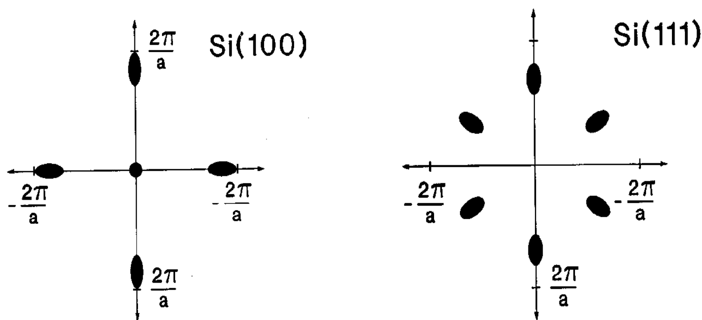

Figure 2.7: *The projection of the 6 band minima in k-space for silicon (100) and (111) [53].*

don't use the isotropic mass assumption, but treat all 6 minima of the conduction band separately. In this case, an incoming electron should find a corresponding state in one of the 6 conduction bands in silicon in order to be collected. This means that there should be a state with the same parallel momentum ($k_{||}$-vector) and positive velocity after de-acceleration like in the isotropic mass model. In Fig. 2.7, the 6 band minima in k-space for silicon are projected on the interface plane as seen in the case of Si (100) and (111). If an electron is coming perfectly perpendicular on the collector (and has enough energy to overcome the Schottky barrier) it needs to go into a state with $k_{||} = 0$ of the silicon. This is only possible in the case of Si (100), but not in Si (111). Although this should give different experimental results in Ballistic Electron Emission Microscopy (see for a review of BEEM [54]), the difference between Si (100) and (111) appears often much less pronounced as a result of elastic scattering on the metal-semiconductor interface [55] or in the metal film.

But even when a possible state can be found with the same parallel momentum and a positive velocity in the x-direction, there is a chance that the electron reflects back into the base . This is a quantum mechanical effect, which is related to the fact that the quantum mechanical wave function of an electron has to be amplitude and phase matched (continuity of the probability density and probability current require that ψ and $\frac{1}{m}\frac{d\psi}{dx}$ should be continuous [56]) on both sides of the barrier. Crowell and Sze have analyzed this quantum mechanical reflection (R) and transmission ($T = 1 - R$) in which they used the exact profile of a Schottky barrier [57], see also [58] for a possible method to calculate this. As can be seen in Fig. 2.8, even when the electron has enough energy and the right momentum, there is only a chance of $\approx 70\%$ ($= \alpha_c^{qm}$) that an electron at 0.9eV within the acceptance cone will be accepted by an 0.8 eV Schottky barrier.

In the above calculations no scattering was taken into account. On the metal-semiconductor interface, electrons can scatter elastically, after which they can fall outside the acceptance cone, but also on the contrary, electrons with their momentum outside the acceptance cone can be scattered back into it.

Similar like on the emitter side, electrons can scatter in silicon with optical-phonons while not yet over the maximum of the Schottky barrier (in the grey zone of Fig. 2.6), after which they don't have enough energy anymore to get over the collector barrier

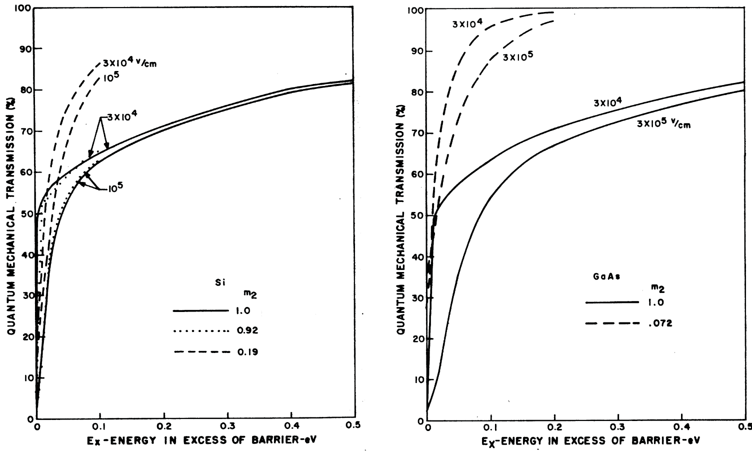

Figure 2.8: *The quantum mechanical transmission as function of Ex, the excess energy in the x-direction above the Schottky barrier, for Si and GaAs [57].*

[52, 56]. By this mechanism only 65% (= α_c^{ph}) of the hot electrons that reached the collector and are not reflected back into the base, will be collected. All these loss factors in the emitter and collector result together in the current transfer for zero base thickness α_0 ($\equiv \alpha_e^{ph} \cdot \alpha_c^{ph} \cdot \alpha_c^{qm}$), which have been calculated [52] and experimentally verified [59] to be $\approx 40\%$ in the case of Si/metal/Si transistors.

2.2 Electron transport in the metallic base

In this theory section the electron transport in the metallic base is discussed. First we will have a look at normal electron transport at the Fermi-level, and how scattering is related to resistance and why this results in giant magnetoresistance in spin valve layers. Next, we explained the scattering possibilities for hot-electrons and how they are different compared to Fermi-electrons. Finally we model the current transport in the base of the spin-valve transistor, in which it is essential that we include the specific emission and acceptance properties of the emitter and collector as described in the previous section.

2.2.1 Scattering of Fermi-electrons in a spin valve

In a perfect crystal an electron can move freely, without any resistance. The normally observed resistance is coming from all deviations from this perfect periodicity of the lattice.
When an electron scatters, it interacts with an other particle or quasi-particle. These particles can be impurity atoms, atoms at crystal dislocations or atoms at interfaces but also on other electrons. Furthermore, electrons can scatter on quasi-particles, like phonons and spin-waves. Phonons are the quasi-particles of the lattice vibrations and spin-waves the quasi-particles of the vibrations of the magnetization. From quantum mechanical perturbation theory the transition time constant (τ) from one initial quantum state (i) into another final quantum state (f) is known as Fermi's Golden rule, and expressed as:

$$\frac{1}{\tau_{i\rightarrow f}} = W_{i\rightarrow f} = \frac{2\pi}{\hbar} H_{fi}^2 \delta(E_f - E_i) \tag{2.25}$$

In which $H_{fi} = \langle \Psi_f \, | H' | \, \Psi_i \rangle$ is the so-called matrix element, that describes how much overlap there is between the initial state of the quantum system (Ψ_i, which describes both interacting (quasi-) particles at the same time) and the final state (Ψ_f) due to the interaction Hamiltonian H'. As shown in Eq. 2.25, any quantum transition from an initial to a final state can only take place when the total energy is conserved, otherwise its transition rate is 0.
Now, we would like to describe with this scattering theory how an electron can scatter from its initial state (E_i, k_i) into some kind of other state (E_f, k_f). In this case, we should not only look at how an electron from its initial state can scatter into a final state, but also how the other particle, with which it interacts, can go from its initial state to an empty final state (we have to describe the total quantum system). So in order to calculate the rate of escape from the initial state, we integrate over all empty states (ρ_{el}^{empty}) for the electron to go into, and have to look with how many particles the electron can interact (ρ_{int}^{filled}) and how many states there are free for these particles to go into (ρ_{int}^{empty})[2]. After that every interaction has to be multiplied with its 'prob-

2 When the interacting particle is absorbed by the interaction, like phonon or spin-wave absorption, no empty final state is needed for the interacting particle. Eq. 2.26 can still be used, but with $\rho_{int}^{empty} \equiv 1$.

ability', the matrix element squared M_{el-int}^2 $(= H_{fi}^2)$, and we have to integrate over all possibilities:

$$\frac{1}{\tau} = \frac{2\pi}{\hbar} \int \rho_{el}^{empty} d\rho_{el} \int M_{el-int}^2 \rho_{int}^{filled} \rho_{int}^{empty} d\rho_{int} \tag{2.26}$$

This integral is very complicated, because we should analyze the exact nature of the scattering mechanism (the E, k relations of both the electron and the interaction particle) and assure that we only integrate over combinations that conserve both momentum and energy. Furthermore, has every combination its own matrix element, which can only be calculated based on the complicated quantum perturbation theory. An example of how we can still use Eq. 2.26, by making several approximations is shown below for the case of in-elastic electron-electron scattering.

For electron transport at the Fermi-level in a metal, the conductivity σ or resistivity ρ can be directly related to the scattering time constant τ, by the semi-classical Drude formula [60]:

$$\sigma = \frac{1}{\rho} = \frac{ne^2\tau}{m^*} = \frac{ne^2\lambda}{m^* v_F} \tag{2.27}$$

In which n is the number of electrons contributing to the electron transport, and $m^* \approx m_{el}$ the effective mass. Instead of using a lifetime τ, it is very common to use a mean free path λ, which is equal to the product of the lifetime τ times the velocity v at the Fermi-level.
Because the scattering rate is dependent on the density of states, and these are exchange splitted in magnetic materials, the scattering for spin-up and spin-down electrons is different. This results in two different resistivities, $\rho^{\uparrow}$ for electrons in the majority band (those with the spin aligned to the net magnetization) and $\rho^{\downarrow}$ for minority electrons for those with their spin opposite to the magnetization.
Valet and Fert [61] have solved the semi-classical Boltzmann equation for Current Perpendicular to the Plane (CPP) transport through a magnetic multi-layer. Their full model includes spin-dependent resistivities in both the bulk and the interfaces, and can take spin-mixing into account, but a more simple model is also presented that applies in the limit when spin-mixing can be neglected. In this case, the total current constitutes of the spin-up and down electrons that carry the current independently in parallel.
If we apply this model to a NiFe/Au/Co spin valve, as shown in Fig. 2.9, we can define two resistances, a low resistance r (voltage drop V over the magnetic layer divided by the current I for a *single* spin channel) when the spin is aligned with the magnetization (for the majority electrons) and a high resistance R when the electron's spin is opposite to the magnetization (for the minority electrons). The resistance in the parallel and anti-parallel state in this simplified model are given by:

$$\frac{1}{R_P} = \frac{1}{2r} + \frac{1}{2R} \Longrightarrow R_P = \frac{2rR}{r+R} \tag{2.28}$$

$$\frac{1}{R_{AP}} = \frac{1}{r+R} + \frac{1}{R+r} \Longrightarrow R_{AP} = \frac{r+R}{2} \tag{2.29}$$

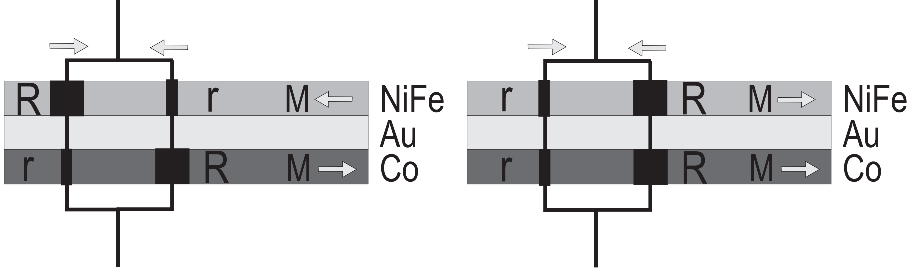

Figure 2.9: *The schematic model of a CPP spin-valve, in which the current is carried independently by the 2 spin-channels in parallel.*

And so the absolute difference in resistance between these two states is:

$$R_{AP} - R_P = \frac{1}{2}\frac{(R-r)^2}{R+r} \tag{2.30}$$

and the relative difference (the magnetoresistance) is expressed by:

$$MR = \frac{R_{AP} - R_P}{R_P} = \frac{\left[\frac{1}{2}\frac{(R-r)^2}{R+r}\right]}{\left[\frac{2rR}{(r+R)}\right]} = \frac{(R-r)^2}{4rR} \tag{2.31}$$

From these formula it is clear that the resistance in the anti-parallel state is higher than the parallel state, and that this results in a positive magnetoresistance. It should be noted that no resistance in the non-magnetic layers was taken into account, the inclusion will reduce the magnetoresistance, because a spin-independent resistance will be added to both the parallel and anti-parallel state.

2.2.2 Hot-electron scattering

The difference between electron scattering in a CPP spin valve and the spin valve in the base of the spin-valve transistor is coming from the energy at which the electron transport takes place.
In a CPP spin valve, the electrons near the Fermi-level contribute to the conductivity, and these electrons scatter on defects, impurities, phonons and spin-waves. But due to Fermi's golden rule they should find also an empty state to scatter into, and these might be rare because all bands are filled up to the Fermi-level as described by the Fermi-Dirac distribution:

$$F(E) = \frac{1}{1+\exp\left(\frac{E-E_F}{kT}\right)}. \tag{2.32}$$

This does mean that the maximum interaction energy is $\approx 3kT = 0.078eV$, because otherwise there are no empty states left to scatter into. So at the Fermi-level most

scattering will be elastic or quasi-elastic. Elastic scattering will only change the momentum (k-vector), but no energy will be lost or gained (for example, by impurity and defect scattering). Quasi-elastic scattering, like for example with phonons or spin-waves, will change both momentum and energy, but only small changes ($\approx kT$) of the energy are allowed.
The electron transport in the spin-valve transistor takes place at about 1.0eV above the Fermi-level, this means that the Fermi-Dirac distribution is nearly 0 at this energy, and so all states are empty for elastic and quasi-elastic scattering. Furthermore, hot-electrons can loose large parts of their excess energy in so-called inelastic scattering events. This inelastic scattering is done through a Coulomb interaction with other electrons from below the Fermi-level that scatter to above it, this mechanism is called a Stoner excitation (see Fig. 2.10). When the momentum space is averaged out, Fermi's golden rule can be written as an integral over all the energies to scatter the hot-electron in [62]:

$$\frac{1}{\tau(E)} = \frac{2\pi}{\hbar}\int_{E_F}^{E} dE'\rho^{>}(E')\int_{0}^{E_F} d\varepsilon\left[{}'\rho^{<}(\varepsilon)\rho^{>}(\varepsilon+E-E')\right]\left|M(E-E')\right|^2 \tag{2.33}$$

In which $\rho^{<}(E') = f(E')\rho(E')$ is the number of electrons that can be excited at energy E' and $\rho^{>}(E') = \left[1 - f(E')\right]\rho(E')$ describes the number of empty states for the interacting electron to scatter into. This integral can be very easily calculated for T=0K when we assume that the matrix element M is constant and the density of states is given like shown in Fig. 2.11, because the distribution function f will then be 0 when E is above the Fermi-level and 1 when below. For noble metals, which have a schematic bandstructure as depicted in Fig. 2.11, this results in an inelastic lifetime for hot-electrons around 1eV given by:

$$\frac{1}{\tau(E)} = \frac{\pi}{\hbar}\rho_s^3\left|M_{ss}^{ss}\right|^2(E-E_F)^2 = a_0(E-E_F)^2 \tag{2.34}$$

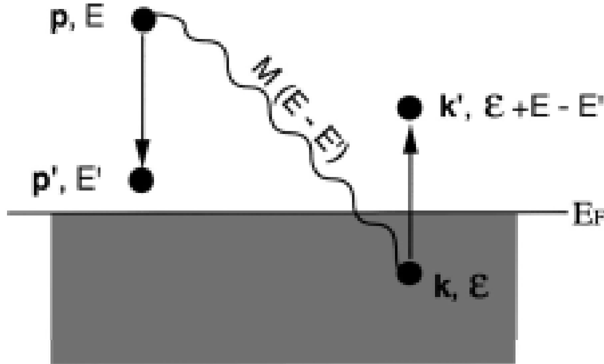

Figure 2.10: *Schematic representation of a Stoner excitation [62]. On the left, the hot-electron that scatters to a lower energy above the Fermi-level. On the right the interaction electron, which comes from below the Fermi-level and scatters into an empty state above it.*

Because at this energy no d-electrons can be excited yet, and so only s-states are involved, resulting in the same energy dependence as the Fermi-liquid theory [60] from Landau. Furthermore, Drouhin has recently published similar type of formula for Stoner-excitations in the noble and transition metals [64, 65]. From time-resolved 2-photon photoemission experiments (2PPE), in which an electron is excited by one laser pulse and probed by a second laser pulse several femtoseconds later, the inelastic lifetime can be measured as function of the hot-electron's energy. These measurements can be fitted with the above theory, and the following constants were obtained, for Cu: $a_0 \approx 2.3 \cdot 10^{-2} fs^{-1} eV^{-2}$ and for Ag: $a_0 \approx 5.7 \cdot 10^{-2} fs^{-1} eV^{-2}$ [62].
In the case of Cobalt, the situation is different, because electrons can be excited from both the s and d-bands, and these d-bands are exchange splitted, as shown schematically in Fig. 2.12 (for comparison, the calculated density of states for Fe, Co, Ni and Ni_3Fe are shown in Fig. 2.13). Because the density of d-states is about 5 times as high as the s-states, we will only analyze processes with the highest order of d-states.
A hot spin-up electron, with its spin aligned to the magnetization, can scatter only in s-states above the Fermi-level. When the hot-electron energy E is below $\omega^{\uparrow}$, the hot electron will mainly excite spin-down [3] electrons from a d-state below the Fermi to above in another d-state. When the hot-electron energy is above $\omega^{\uparrow}$, there are additional scattering processes in which spin-up electrons excite spin-up electrons from the spin-up d-band into an empty s-state. The resulting inelastic lifetime for $E > \omega^{\uparrow}$ due to these two contributions can be written as:

$$\begin{aligned} \frac{1}{\tau^{\uparrow}(E)} &\simeq \frac{2\pi\rho_d^3}{\hbar}\left[\frac{1}{2}\left(\frac{\rho_s}{\rho_d}\right)\left|M_{sd}^{sd}\right|^2 (E-E_F)^2 + \frac{1}{2}\left(\frac{\rho_s}{\rho_d}\right)^2\left|M_{ss}^{sd}\right|^2 (E-E_F-\omega^{\uparrow})^2\right] \\ &= a_0^{\uparrow}(E-E_F)^2 + a_1^{\uparrow}(E-E_F-\omega^{\uparrow})^2 \end{aligned} \tag{2.35}$$

Hot spin-down electrons have more scattering possibilities, these electrons can directly scatter into the more abundant d-states, while exciting an other d-state electron below the Fermi-level to above into another d-state. Also here we can excite above

3 A hot up-electron can interact with a spin-down electron from below the Fermi-level, because the interaction force is the Coulomb force, which is only dependent on charge, not on spin. It should be noted that the spin of the *individual* electrons is always conserved in a Stoner excitation.

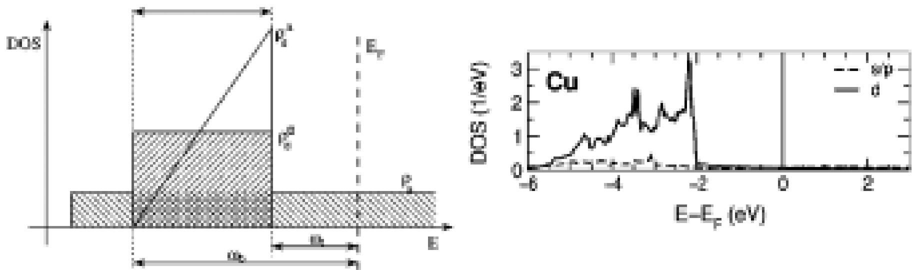

Figure 2.11: *On the left, the schematic densities of states for nobel metals (like for Cu, Ag and Au) [62] and on the right for comparison, the calculated density of states of Cu taken from [63].*

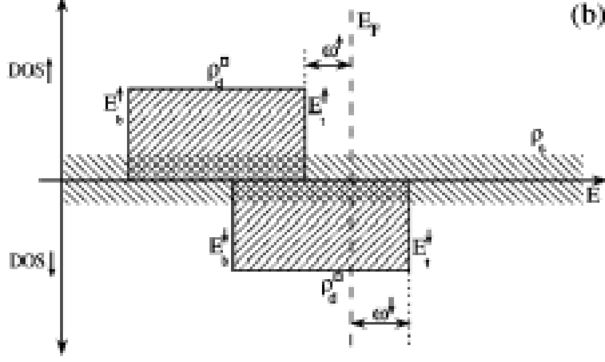

Figure 2.12: *The schematic densities of states for Co, as used below in the calculations of the lifetime τ. $\omega^{\uparrow} \simeq 0.6eV$, $\omega^{\downarrow} \simeq 1.3eV$ and $\rho_s/\rho_d \simeq 0.2$. Taken from [62].*

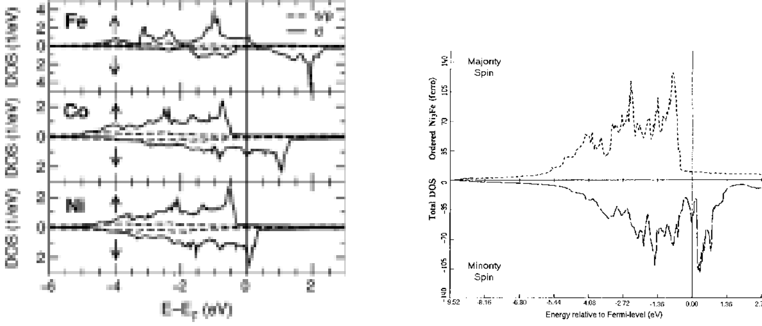

Figure 2.13: *On the left, the calculated density of states for Fe, Co and Ni [63]. And on the right, the calculated density of states of the ordered Ni_3Fe alloy (almost permalloy), adapted from [66].*

$\omega^{\uparrow}$ electrons from the spin-up (and down of course) d-band and so the lifetime can be written as:

$$\frac{1}{\tau^{\downarrow}(E)} \simeq \frac{2\pi\rho_d^3}{\hbar}\left[\frac{1}{2}\left|M_{dd}^{dd}\right|^2(E-E_F)^2 + \frac{1}{2}\left(\frac{\rho_s}{\rho_d}\right)\left|M_{ds}^{dd}\right|^2(E-E_F-\omega^{\uparrow})^2\right]$$
$$= a_0^{\downarrow}(E-E_F)^2 + a_1^{\downarrow}(E-E_F-\omega^{\uparrow})^2 \quad (2.36)$$

Aeschlimann et. al. [67] has measured the spin-dependent inelastic lifetime in Co by 2PPE, and the energy dependence was fitted by Zarate et. al. [62] to the above theory as shown in Fig. 2.14, resulting in: $a_0^{\uparrow} = 0.14$, $a_1^{\uparrow} = 0.04$ for spin-up electrons and $a_0^{\downarrow} = 0.17$, $a_1^{\downarrow} = 0.65 fs^{-1}eV^{-2}$ for spin-down electrons.
It should be noted that the inelastic lifetime/scattering length as important for the spin-valve transistor is slightly longer, because it is related to the rate at which electrons at about 0.9eV (as emitted by the Si/Pt Schottky barrier) can reduce their energy to below 0.8eV (Si/Au collector barrier height). This is only a small correction, because

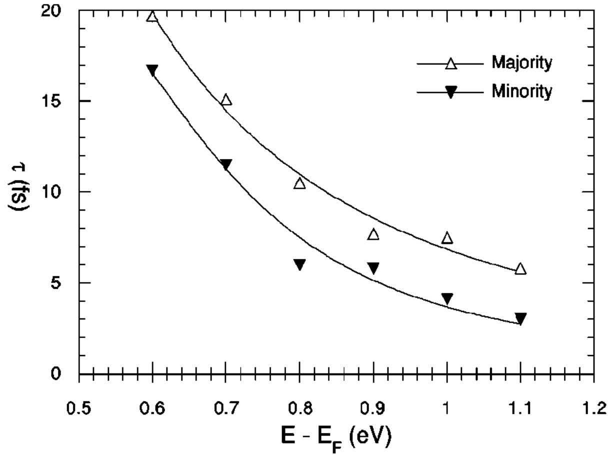

Figure 2.14: *The in-elastic lifetimes for Co measured by spin-dependent 2PPE (dots) and the fit (line) based on the discussed theory [62].*

the average Stoner excitation will divide the hot-electron energy by 1.5∼2.
In a recent experiment [68] with spin-polarized electron energy loss spectroscopy (SPEELS) it has been shown that that hot-electrons can also interact with spin-waves, also known as magnons. In a ferromagnetic material at T=0K, all the magnetic spins of the atoms in the lattice are aligned (within a domain) due to the exchange interaction. When such a material is heated up, all the magnetic spins of the atoms start to precess around the net magnetization vector in collective modes, called spin-waves [69]. In Fig. 2.15 (a), this collective precession is depicted, and when viewed from above (b), it is clear why we talk about a spin-wave.
A spin-wave has both energy and momentum and its dispersion relation is given by $E \approx Dq^2$, in which D is the spin-stiffness constant (≈ 281, 400 and 555 meV Å^2 for Fe, Co and Ni, respectively [70]). Furthermore, a spin-wave has spin $\sigma = -1\,\hbar$ (reduces the magnetization), making it only possible to interact with an electron by flipping the electron spin. Due to this, spin-up electrons ($\sigma = 1/2\,\hbar$) can only absorb a spin-wave, after which they become spin-down ($\sigma = -1/2\,\hbar$) electrons. This means that spin-up electrons can only scatter on thermal spin-waves, but at T=0K there are no spin-waves available to scatter with. For spin-down electrons ($\sigma = -1/2\,\hbar$) the sit-

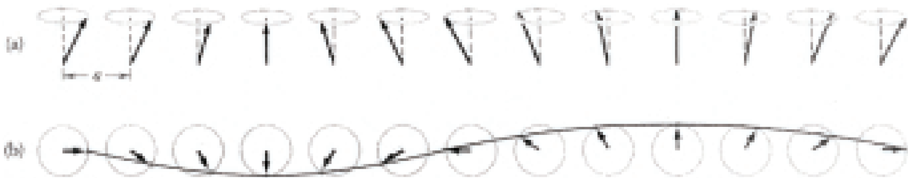

Figure 2.15: *A 1-dimensional lattice of spins with a spin-wave, viewed in perspective (a) and from above (b) . Taken from [69].*

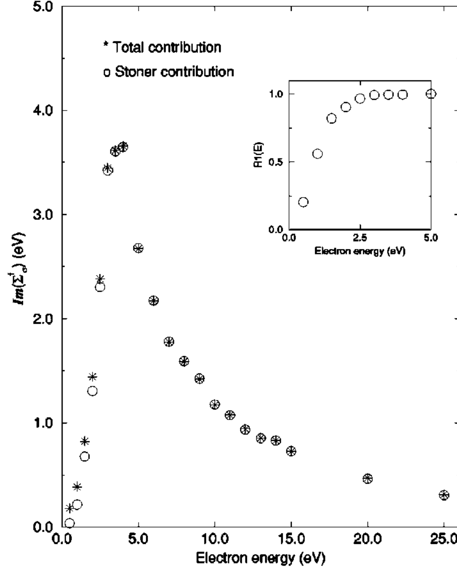

Figure 2.16: *The imaginary part of the self-energy ($Im(\Sigma_{\downarrow}) = -\hbar/2\tau_{\downarrow}$) due to spin-wave emission and Stoner excitations as a function of the hot-electron energy for spin-down electrons in Fe. The inset shows the partial contribution of the Stoner excitations compared to the total self energy. For further details, see [72].*

uation is different, because spin-down electrons can spontaneously emit spin-waves, even at T=0K. In this process a spin-wave with $\sigma = -1\,\hbar$ is created and the spin-down electron ($\sigma = -1/2\,\hbar$) becomes a spin-up electron ($\sigma = 1/2\,\hbar$). This process is not only limited to small energies (about kT), as do thermal spin-waves, but larger energy losses might also be possible for hot-electrons. In the spin-valve transistor these high energy loss processes will contribute to the inelastic scattering length, because these will lower the electrons energy to below the collector barrier. Hong and Mills have done calculations on the spin-wave emission by hot spin-down electrons [71, 72]. In Fig. 2.16, a result of their calculation for Fe shows that spin-wave scattering can be about as strong as electron-electron scattering for spin-down (minority) electrons around 1eV.
Furthermore, spin-down electrons can also emit thermal spin-waves (so-called stimulated emission), which happens with the same rate as for spin-up electrons (so for thermal spin-waves, $\tau^{\uparrow}_{sw} = \tau^{\downarrow}_{sw}$, [71]).
The thermal excitation of spin-waves reduces the magnetization of a material with one unit of spin ($\hbar$). Therefore, at low temperatures ($T \leq 0.4T_c$) the reduction of the magnetization with temperature is mainly due to spin-waves, above $0.4T_c$, the quantum mechanical Weiss theory predicts the loss of magnetization.
So if we want to calculate the relative decrease in magnetization due to spin-waves, we first have to calculate the number of thermal spin-waves, which can be calculated by an integration over the frequencies (ω) of the density of states (first term in square

brackets) times the Planck distribution (second term) [69]:

$$N_{SW} = \int_0^\infty \left[\frac{1}{4\pi^2} \left(\frac{\hbar}{2JSa_0^2} \right)^{3/2} \omega^{1/2} \right] \left[exp\left(\frac{\hbar\omega}{kT} \right) - 1 \right]^{-1} d\omega = \zeta(\frac{3}{2}) \left(\frac{kT}{8\pi JSa_0^2} \right)^{3/2} \tag{2.37}$$

In which J is the exchange coupling between neighboring atoms, S the magnetic spin per atom, a_0 the lattice parameter and $\zeta(3/2) = 2.61237$. When the number of spin-waves is divided by the total number of magnetic spins per volume (SQ/a_0^3, in which Q denotes the number of atoms per unit cell, sc:1, bcc:2 and fcc:4), this ratio will be equal to the relative change of magnetization:

$$\frac{\Delta M}{M(0)} = \frac{N_{SW}}{N_{MAG}} = \frac{\zeta(3/2)}{SQ} \left(\frac{kT}{8\pi JS} \right)^{3/2} \tag{2.38}$$

This formula can be rewritten in a more convenient way:

$$\frac{\Delta M}{M(0)} = \frac{N_{SW}}{N_{MAG}} = A \left(\frac{T}{T_c} \right)^{3/2} \tag{2.39}$$

Because the exchange energy J is proportional to the Curie temperature ($J \propto T_c$). From experiments, the constant A can be extracted and appears to be almost identical (law of corresponding temperatures) for fcc-Ni (A=0.1177) and bcc-Fe (A=0.1145).[4]

2.2.3 Hot-electron transport in a spin valve

After having described the scattering mechanisms for hot-electrons in the base of the spin-valve transistor, we will discuss in this section how the hot-electron transport is affected by these scattering events. It should be remembered that the hot-electrons are coming from Schottky diodes and these are known to inject and collect in a very narrow angle (typically less than $10°$, see section 2.1.3 and 2.1.4). This is why a detailed analysis of the momentum distribution will become important, when describing the electron transport through the base.

This section is divided into three parts. In the first part we describe the hot-electrons transport in a single base layer. Next, we explain how this result can be used to calculate the current transport through magnetic multilayers. Next, we will show numerical results that show how the collector current changes due to scattering in the bulk and at the interfaces. And finally, the dependence of the collector current (and magnetocurrent) with magnetic layer thickness will be investigated.

2.2.3.1 The Boltzmann equation in a single layer

In order to describe the hot-electron transport in the base, we will use the semi-classical Boltzmann equation in the metallic base. After that, we will include the

4 So the number of thermal spin-waves per volume can also be written as: $N_{SW} = \frac{SQA}{a_0^3} \left(\frac{T}{T_c} \right)^{3/2}$.

influence of the Schottky barriers in the boundary conditions (a detailed derivation of these boundary conditions can be found in Appendix A.1.2 and A.1.3). This approach gives the flexibility to incorporate various physical scattering mechanisms, and gives good insight into their effect on the transport. Other methods to describe the non-equilibrium transport of hot-electrons are the Wigner approach [73, 74, 75], which is based on quantum mechanical density functions or the Keldysh approach [76, 77], which is based on non-equilibrium Green functions.
We start from the general Boltzmann equation [60]:

$$\frac{\partial f(\overrightarrow{x},\overrightarrow{v},t)}{\partial t}+\frac{\partial f(\overrightarrow{x},\overrightarrow{v},t)}{\partial \overrightarrow{x}}\cdot\frac{\partial \overrightarrow{x}}{\partial t}+\frac{\partial f(\overrightarrow{x},\overrightarrow{v},t)}{\partial \overrightarrow{v}}\cdot\frac{\partial \overrightarrow{v}}{\partial t}= -\sum_{v'}\left[W_{vv'}f(\overrightarrow{x},\overrightarrow{v},t)-W_{v'v}f(\overrightarrow{x},\overrightarrow{v}',t)\right], \quad (2.40)$$

in which $f(\overrightarrow{x},\overrightarrow{v},t)$ is the Boltzmann distribution function describing the number of electrons in a certain phase-space with position $\overrightarrow{x}$ and velocity $\overrightarrow{v}$ at time t. $W_{vv'}$ is the transition rate from velocity v to v' and $W_{v'v}$ vise versa.
We can make several simplifications based on the type of current transport for hot-electrons in the base. First, we seek a stationary solution and so the first term in Eq. 2.40 can be ignored. Second, the electrons need to travel through the base without the help of an electrical field, i.e., there is no acceleration ($\frac{\partial \overrightarrow{v}}{\partial t}=0$) and so, the third term can be ignored. After these simplifications Eq. 2.40 reduces to:

$$\frac{\partial f(\overrightarrow{x},\overrightarrow{v})}{\partial \overrightarrow{x}}\cdot\overrightarrow{v}=-\sum_{v'}\left[W_{vv'}f(\overrightarrow{x},\overrightarrow{v})-W_{v'v}f(\overrightarrow{x},\overrightarrow{v}')\right]. \quad (2.41)$$

By using Mathiesen's rule [60] ($W_{vv'}=\sum_s W^s_{vv'}$) we can now include all scattering mechanisms, each with their own scattering rate. Here we will include isotropic elastic and inelastic scattering. But spin-flip scattering is not taken into account, in order to simplify the calculations, because without spin-mixing the two spin channels (spin-up and spin-down) can be treated separately. Let us define the exact nature of the elastic and inelastic scattering mechanisms as included in the model.
Inelastic scattering (W^i), is modelled as a process which lowers the energy of an electron to below the collector barrier (see Fig. 2.17), resulting in an effective loss for the collector current. This gives only out-scattering ($W_{vv'}$), and thus:

$$-\sum_{v'}\left[W^i_{vv'}f(\overrightarrow{x},\overrightarrow{v})-W^i_{v'v}f(\overrightarrow{x},\overrightarrow{v}')\right]=-\frac{f(\overrightarrow{x},\overrightarrow{v})}{\tau_i\left(\overrightarrow{v}\right)}. \quad (2.42)$$

It should be noted that this makes the inelastic lifetime (τ_i), as relevant for the SVT, dependent on the maximum allowed energy loss and thereby on the difference between emitter and collector Schottky barrier height. In general, inelastic scattering by electron-hole pair creation (electron-electron interaction) involves large energy loss. However, for large Schottky barrier difference, part of the inelastic scattering events may not lower the electron energy to below the collector barrier maximum.
Elastic scattering (W^e) can remove (out-scattering) an electron from the state with velocity/direction v with timeconstant τ_e, but can also scatter an electron from the state

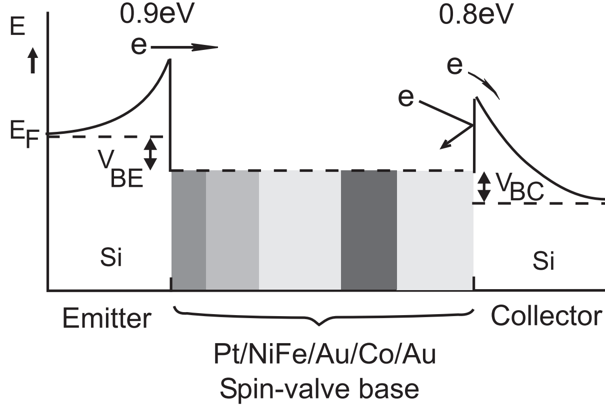

Figure 2.17: *The schematic energy diagram of the SVT. The electrons are injected from the Si-Pt Schottky diode with a barrier height of 0.9eV. Electrons are collected after passing the Au-Si Schottky barrier (0.8eV) on the collector side.*

with velocity v' into one with velocity v (in-scattering). For the elastic scattering we thus have:

$$-\sum_{v'}[W^{e}_{vv'}f(\overrightarrow{x},\overrightarrow{v})-W^{e}_{v'v}f(\overrightarrow{x},\overrightarrow{v}')]=$$
$$-\frac{f(\overrightarrow{x},\overrightarrow{v})}{\tau_e(\overrightarrow{v})}+\frac{1}{4\pi|v|^2\tau_e(\overrightarrow{v})}\int f(\overrightarrow{x},\overrightarrow{v}')\delta(|\overrightarrow{v}|-|\overrightarrow{v}'|)d\overrightarrow{v}', \quad (2.43)$$

where the first term on the right hand side describes the out-scattering and the second, the in-scattering. As included into this model, elastic scattering can remove an electron from the acceptance cone, but it can also scatter an electron that was already outside the acceptance cone back into it (see Fig. 2.18). It should be noted that elastic scattering in this model includes all scattering events after which the electron still has enough energy to overcome the collector barrier, that is, quasi-elastic scattering mechanisms are included as purely elastic.
These definitions simplify the numerical calculation significantly, as one does not have to calculate the evolution of the *energy* distribution of the hot electrons. After including the elastic and inelastic scattering mechanisms in Eq. 2.41 we obtain:

$$\frac{\partial f(\overrightarrow{x},\overrightarrow{v})}{\partial\overrightarrow{x}}\cdot\overrightarrow{v} = -\left[\frac{1}{\tau_e(\overrightarrow{v})}+\frac{1}{\tau_i(\overrightarrow{v})}\right]f(\overrightarrow{x},\overrightarrow{v}) + \frac{1}{4\pi|v|^2\tau_e(\overrightarrow{v})}\int f(\overrightarrow{x},\overrightarrow{v}')\delta(|\overrightarrow{v}|-|\overrightarrow{v}'|)d\overrightarrow{v}'. \quad (2.44)$$

In order to reduce the number of calculations and to facilitate the integral calculation we will assume that all the hot electrons have the same magnitude of velocity [5]. Using

5 It is also possible to describe the absolute velocity/energy dependence in more detail and use only a 1-directional "angular momentum distribution" as done by Mahan [78], but in the case

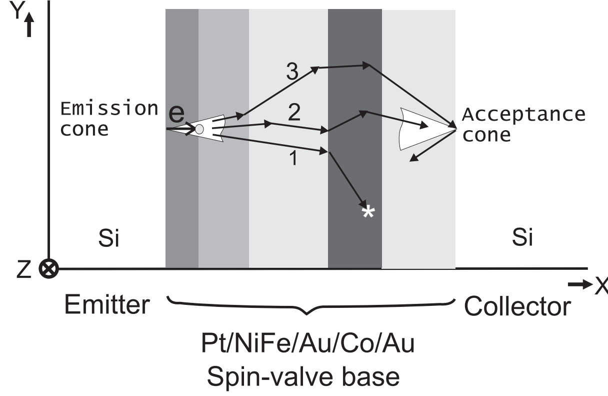

Figure 2.18: *A schematic cross-section of the SVT. Three possible paths of an electron travelling through the base of the SVT are drawn: 1) an electron scatters inelastically (as indicated by *) after which it is lost, 2) an electron scatters elastically several times, but still arrives within the acceptance cone of the collector, 3) an electron scatters elastically and arrives at the collector outside the acceptance cone, and thus will be reflected back into the base.*

this simplification we can convert the lifetimes into mean free paths ($\lambda = v\tau$) and transform the integral in Eq. 2.44 to an integration over the surface of a sphere. Making use of the cylindrical symmetry of the SVT (equivalence of y- and z-axis, see Fig. 2.18), we obtain:

$$\boxed{\mu \frac{\partial f(x,\mu)}{\partial x} = - \left[\frac{1}{\lambda_e} + \frac{1}{\lambda_i} \right] f(x,\mu) + \frac{1}{2\lambda_e} \int_{-1}^{1} f(x,\mu) d\mu.} \tag{2.45}$$

Here, $f(x, \mu)$ is the Boltzmann distribution function describing the number of electrons *per second* at position x with momentum in the direction μ, where μ is defined as the cosine of θ, the solid angle between the velocity vector and the x-axis of the transistor. After solving Eq. 2.45 numerically, which will be explained in Appendix A.2.2 (page 111), we can calculate the current in the positive x-direction from the distribution function using:

$$I_x(x) = q \int_0^1 \mu f(x,\mu) d\mu. \tag{2.46}$$

Equations (2.45) and (2.46) form the basis of our model calculations. However, it is instructive to compare with a purely one-directional model in which only electrons with their momentum parallel to the x-axis ($\mu = 1$) are considered. In this case, any elastic or inelastic scattering event removes an electron from the collector current and no correct treatment of elastic in-scattering can be made. Eq. 2.45 can be written in

of the spin-valve transistor it seems more appropriate to calculate the full angular distribution due the momentum selection (acceptance cone) of the collector.

this one-directional approach as:

$$\frac{\partial f(x)}{\partial x} = -\left[\frac{1}{\lambda_e} + \frac{1}{\lambda_i}\right] f(x). \tag{2.47}$$

This can easily be solved, resulting in:

$$f(x) = f_0 \exp(-\frac{x}{\lambda_{eff}}). \tag{2.48}$$

Here, f_0 is the distribution at the emitter-base interface ($x = 0$) and $f(x)$ is the position dependent distribution function that decays exponentially with the characteristic length λ_{eff}, as will do the current. In this case, λ_{eff} is simply $(\lambda_e^{-1} + \lambda_i^{-1})^{-1}$.
Considering all possible angles and including in-scattering events, as we will do in the calculations below, results in a longer λ_{eff} as compared to that of the one-directional case. This is, because electrons which were scattered elastically to directions outside the acceptance cone, can still scatter back into the acceptance cone. In this case an exponential decay is still observed, but with a different value of λ_{eff} that is not only a function of λ_e and λ_i, but also of the local angular distribution and the collector properties.
Having derived the Boltzmann equation (Eq. 2.45), we have to solve it. Only for two simple cases we can find an analytic solution, the first case is the one-directional as already mentioned above. Furthermore, it is possible to find an analytic solution for the 3-dimensional case when we search for a distribution function which exponentially attenuates with a single attenuation length λ_{eff} (i.e. $f(x, \mu) = A(\mu)exp(-x/\lambda_{eff})$). How to find this solution and in which case it applies is explained in Appendix A.2.1 (page 110). In general this solution cannot be used because it only applies to special boundary conditions and is only valid when the scattering properties remain the same in the whole base (no possibility to model a multilayer base as found in the spin-valve transistor). So the only way left is to solve Eq. 2.45 numerically.

2.2.3.2 The Boltzmann equation in a magnetic multilayer

In order to calculate the hot-electron transport through the base of the spin-valve transistor, it is essential that we can model a multilayer. The different materials in this multilayer will all have their own scattering properties, and in between these layers there will be interfaces that will scatter.
Bulk scattering in the different layers can be modeled by using the appropriate scattering parameters based on the current position in the device. At the interfaces there will be elastic scattering, this will occurs at the metal-metal *as well as at the silicon-metal interfaces*. In order to model this we will introduce a parameter D that represents the interface diffusivity. From the incident distribution of electrons, a fraction $(1 - D)$ crosses the interface without being scattered, while a fraction D will be scattered elastically. The elastic interface scattering is assumed to be isotropic, such that a fraction $D/2$ of the electrons will still move in the forward direction, but the other $D/2$ will be scattered in the backward direction.
The last step before we can calculate the current flow through the base of the SVT is

to take into account that in ferromagnetic materials the mean free path is dependent on the relative orientation of the electron spin and the local magnetization. When a spin-up electron travels through a ferromagnet whose magnetization is aligned with the electron's spin, it will scatter relatively little (with longer $\lambda_e^{\uparrow}$ and $\lambda_i^{\uparrow}$), while an electron with spin opposite to the magnetization scatters more strongly (shorter $\lambda_e^{\downarrow}$ and $\lambda_i^{\downarrow}$). Note that in principle also the interface scattering can be spin dependent, but in the numerical calculations we only include spin-independent interface scattering to show the effect of it on the current transfer ratio.
In order to calculate the current through the SVT, we start with 50% spin-up electrons and 50% spin-down electrons, as injected from the non-magnetic emitter. For both these spin-channels, we calculate separately how much current will arrive at the collector, after which the two spin-channels are added to obtain the total collector current. This can be done in the parallel and anti-parallel state of the spin valve, and results finally in the MC.

2.2.3.3 Numerical results

The spin-valve transistor we will consider here, has the same structure as used in our experiments. It consists of two Si wafers with the following base: Pt(20Å) / NiFe(30Å) / Au(35Å) / Co(30Å) / Au(20Å) // Au(20Å) ('//' indicates the bond interface). When injecting an emitter current of 2 mA, a collector current of 11nA was measured with an MC of 200% at room temperature [29].
Essential to any simulation is the use of realistic material parameters. Many of the scattering lengths at 0.9 eV above the Fermi level are not precisely known. In a recent BEEM study [79], the attenuation lengths [6] for electrons at 1eV above the Fermi level in Co were measured ($\lambda_{att}^{\uparrow} \approx 23$Å , $\lambda_{att}^{\downarrow} \approx 8$Å). Both elastic and inelastic scattering contribute to this attenuation length. Inelastic lifetimes have been probed in a recent time- and spin-resolved two photon photoemission experiment [63, 67] for Co. At about 1eV, the measured inelastic lifetimes are $\tau_i^{\uparrow} \approx 8fs$ and $\tau_i^{\downarrow} \approx 4fs$. Based on these inelastic lifetimes we can calculate the inelastic scattering length with $\lambda_i = v\tau_i$ and a velocity of $v \approx 20$Å/fs for the hot electrons in the s-band. This results in $\lambda_i^{\uparrow}$ =160Å and $\lambda_i^{\downarrow}$ =80Å. Thus, inelastic scattering alone is not sufficient to obtain total attenuation lengths of 23 and 8Å, respectively. Therefore, we add elastic scattering with $\lambda_e^{\uparrow}$ =30Å and $\lambda_e^{\downarrow}$ =10Å. For NiFe, no experimental data was available, so we choose the same values as for Co. It should be noted that based on the used elastic and inelastic scattering lengths in Co and NiFe, an electron can on the average scatter elastically ≈ 5 times before it looses its energy in an inelastic scattering event. For gold, there are many BEEM studies [80, 51], all reporting slightly different values, but in general one finds much larger scattering lengths than for Co. Furthermore, the measured values are much larger than the layer thickness, so bulk scattering in the gold layer will have a small influence on the transfer ratio (I_c/I_e). Finally, for the platinum layer an attenuation length on the order of 40Å was measured in a BEEM study on Pt-

6 The attenuation length is the characteristic exponential decay length, with which the current of the **device** reduces. It is not only related to the physical mean free paths for elastic and inelastic scattering, but also experimental details, like the emission and collection method, are important.

Mat	W[Å]	$\lambda_e(\uparrow / \downarrow)$ [Å]	$\lambda_i(\uparrow / \downarrow)$ [Å]	$\left(\lambda_e^{-1} + \lambda_i^{-1}\right)^{-1} (\uparrow / \downarrow)$ [Å]
Pt	20	50	100	33
NiFe	30	30/10	160/80	25/9
Au	35	200	400	133
Co	30	30/10	160/80	25/9
Au	20	200	400	133
Au	20	200	400	133

Table 2.1: *The materials in the base of the SVT, their thickness (W) and the corresponding elastic (λ_e) and inelastic (λ_i) mean free paths used in the calculations. Furthermore, the expected attenuation length based on the one-dimensional model is shown in the last column.*

silicide [81]. Because the elastic and inelastic contributions are not known separately, we have simply chosen values in agreement with this total attenuation. All the used bulk scattering parameters are summarized in table 2.1 and the interface diffusivity D has been set to 0.9 for all interfaces, unless stated otherwise. This was found to result in a collector current similar to the experimental values. We will however also vary the interface diffusivity and examine the influence on the collector current. It should be noted that experimental MC values can be higher than the values calculated here, because no spin-dependent interface scattering was taken into account.
A first important characteristic of the current transport in the SVT is the exponential decay of the current with the position in the base layer. In Fig. 2.19, we have calculated the current carried by electrons with their momentum such that they are within the acceptance cone. This current is given by:

$$I_{coll}(x) \equiv q \int_0^1 \mu T_{collector}(\mu) f(x,\mu) d\mu = q \sum_i a_i \, \mu_i \, T_{collector,i} \, f_i^{>}(x) \tag{2.49}$$

An exponential decrease of the current is obtained for both spin-up and spin-down electrons, and in the parallel (P) as well as the anti-parallel (AP) magnetic state of the spin valve. Needless to say, the exponential decay varies from one layer to the next, and depends on the hot-electron spin in the ferromagnetic layers. Obviously, the spin-dependent exponential decay is one of the factors that facilitates the huge relative magnetic response of the SVT. Compare this to the role of the mean free path in the giant magnetoresistance of a magnetic multilayer, where the resistances are linearly proportional to (the inverse of) the mean free path (see Eq. 2.27).
A further observation in Fig. 2.19 is that step-like current losses occur at each of the interfaces, due to elastic scattering at the interfaces having relatively strong diffusivity (D = 0.9). It is however interesting to note that the current loss is not equal at all interfaces, even though the interface diffusivity D has been set to same value of 0.9 for all interfaces. This illustrates that the effect of elastic scattering on reducing the current depends on factors other than the scattering strength. More precisely, it depends on the angular distribution of hot electrons that is incident on the scattering interface. At the first Pt/NiFe interface, the angular distribution is still strongly forward directed, and so interface scattering will result in a lot of these electrons being deflected and removed from the acceptance cone of the collector. As the hot electrons

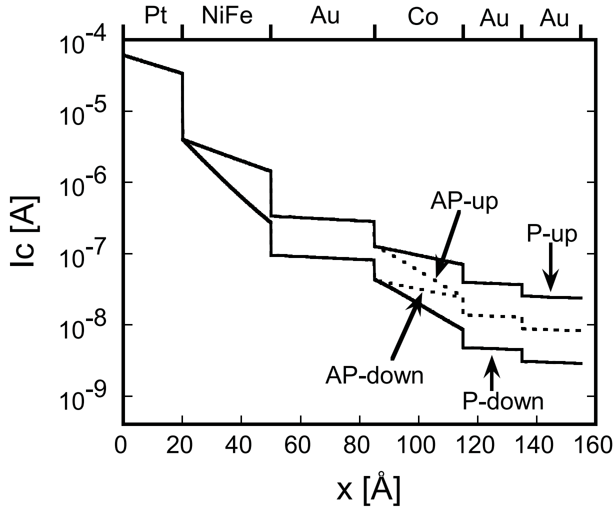

Figure 2.19: *The current within the collector acceptance cone as a function of the position x inside the SVT for the spin-up and spin-down electrons, in the parallel (P) and anti-parallel (AP) magnetic state of the spin valve.*

travel through the base, their angular distribution becomes more and more isotropic due to the cumulative effect of all the elastic scattering. Thus, at interfaces closer to the collector (such as the Au/Au bond interface) the more isotropic distribution reduces the influence of additional elastic scattering. Electrons moving at large angles outside the acceptance cone, and even electrons moving in the wrong direction (to the left) can now be scattered back inside the acceptance cone. Note that elastic interface scattering already has been taken into account for the Si-Pt interface. This is why the curve in Fig. 2.19 starts at $8 \cdot 10^{-5}$A, and not at the emitter current of 1mA (2mA total emitter current=1mA spin-up electrons and 1mA spin-down electrons).

Another important point is that the current decay is found to be stronger in the NiFe layer as compared to that in the Co layer, even though the scattering parameters λ_e and λ_i were chosen to be exactly the same for both materials. This difference is also due to the different angular distribution at different positions in the SVT base. In the NiFe layer, which is closer to the emitter, the electron distribution is more forward directed, while in the Co layer the distribution has become more isotropic. Elastic scattering in the NiFe layer will thus have more effect than in the Co layer, resulting in an effective decay length that is shorter in NiFe than in Co.

In Fig. 2.20 we show the dramatic effect of the interface diffusivity D on the collector current and the magnetocurrent. In Fig. 2.20 (A) we see that as the interface diffusivity is increased from 0 to 1, the collector current is reduced by about 3 orders of magnitude. It thus appears that strong elastic interface scattering can easily account for the low transfer ratios that are experimentally observed. Improving the interface quality therefore seems a promising route for increasing the output current of the SVT. The influence of the interface scattering on the MC, as shown in Fig. 2.20 (B), is quite remarkable since the interface scattering was taken to be independent of spin. In the

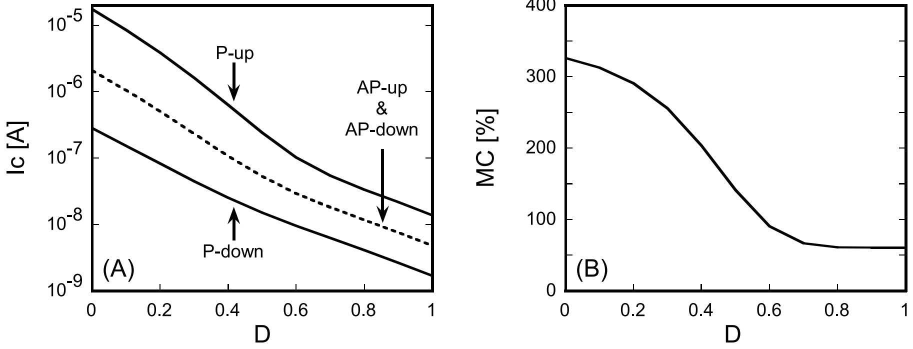

Figure 2.20: *The influence of elastic interface scattering D on: the collector current for the spin-up and down channels in both magnetic configurations (A) and the magnetocurrent (B).*

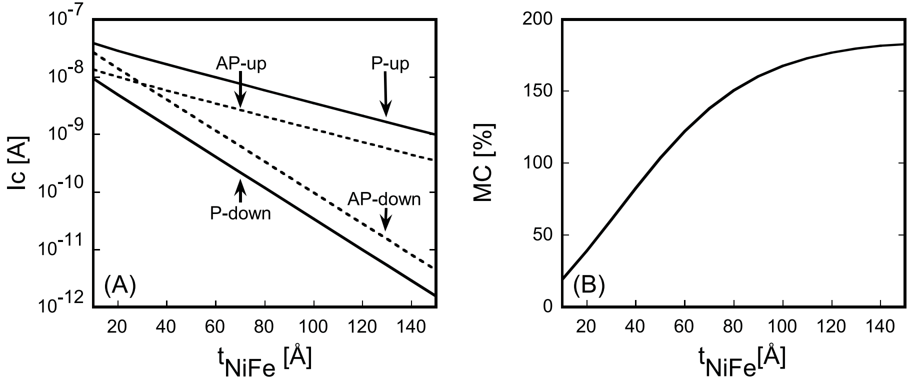

Figure 2.21: *The influence of the NiFe thickness on: the collector current for the spin-up and down channels in both magnetic configurations (A) and the magnetocurrent (B).*

simple one-directional approach it can be easily shown that a spin-independent scattering process cannot lower the MC, as it attenuates both spin currents by the same factor, leaving the ratio unchanged. Again, the explanation has to do with the influence of the angular distribution function on the current decay. For negligible diffuse interface scattering, the angular distribution remains strongly forward directed, such that the spin-dependent elastic bulk scattering in the magnetic layers contributes effectively to the MC. However, when diffuse interface scattering is strong, the role of bulk spin-dependent elastic scattering is diminished and the MC becomes dominated by the spin asymmetry of the inelastic bulk scattering only.
In Fig. 2.21 and 2.22 we show how the MC scales with the ferromagnetic layer thickness (NiFe and Co). First, in Fig. 2.21, we change only the thickness of the NiFe layer, keeping the Co layer thickness fixed at 30 Å. The current of electrons with spin aligned to the NiFe magnetization decreases exponentially with an attenuation length of 38 Å as extracted from Fig. 2.21 and the current of electrons with their spin opposite to the NiFe magnetization attenuates with a characteristic length of 16Å. Hence,

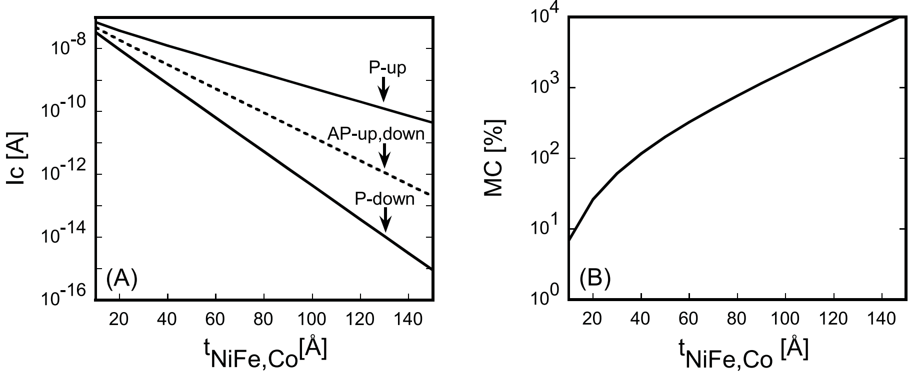

Figure 2.22: *The influence of the thickness of both the NiFe and Co layers on: the collector current for the spin-up and down channels in both magnetic configurations (A) and the magnetocurrent (B).*

for thicker NiFe layers the MC increases and it saturates at a value that is determined by the finite thickness of the fixed Co layer. This saturation occurs at a NiFe thickness of about 100 Å, when the NiFe transmits only majority-spin electrons. When the observed attenuation length in NiFe is compared to the value from the 1-dimensional model (see table 2.1) we see that the inclusion of elastic in-scattering results in a remarkably larger attenuation length (i.e. 38 Å as compared to 25 Å for majority-spin electrons and 16 Å as compared to 9 Å for minority-spin electrons). When we compare the numerically calculated attenuation length with that of the analytical solution of the 3-dimensional equation (as derived in Appendix A.2.1 on page 110), a much better agreement is obtained. The results are the following: analytically 39 Å vs. numerically 38 Å for majority-spin electrons and for minority-spin electrons both the analytical and numerical calculations result in an attenuation length of 16 Å. The good agreement between the numerical calculations and the analytical formula is due to the fact that the angular distribution for the analytic solution for a ratio of $\lambda_i/\lambda_e \approx 5$ is fairly close to the angular distribution as used in the numerical calculations. So this will finally resulting in the same attenuation length.
In Fig. 2.22, we have changed both the NiFe and the Co layer thickness, so that also the filtering properties of the Co layer improve as the layers become thicker. The MC in this situation increases exponentially with magnetic layer thickness, but it does not saturate. Note that there is a trade-off between MC and magnitude of the collector current, the latter goes down seriously as the layers thickness increases.

2.3 Theory overview: a simple model

In this section, we present an overview of the current transport in the spin-valve transistor. This will lead to a model that can be used to compare experiments with.
In the spin-valve transistor, electrons are injected from the emitter into the base. Because these electrons travel over the Schottky barrier, this results in hot electrons with

an excess energy of $\approx$ 1eV ($\geq \Phi_e$) above the Fermi-level (see Fig. 2.17). In the base, these electrons will scatter inelastically (loosing their excess energy) and elastically (only changing their momentum, but not loosing their energy). At the collector only electrons with at least enough energy and the right momentum will be able to come over the collector Schottky barrier. So only a fraction α of the emitter current (I_e) will finally contribute to the collector current (I_c), because the fraction $(1 - \alpha)$ has lost its energy, or doesn't have the right momentum to be collected (resulting in the base current). So the collector current can be written as:

$$I_c = \alpha \cdot I_e \tag{2.50}$$

in which the current transfer ratio $\equiv \alpha$ is the product of different attenuation factors:

$$\alpha = \left[\alpha_e^{phonon}\right] \times \alpha_b \times \left[\alpha_c^{qm} \times \alpha_c^{phonon}\right] \tag{2.51}$$

There is attenuation in the emitter due to phonon scattering (α_e^{phonon}), there is elastic and inelastic scattering in the base resulting in a base attenuation (α_b) and at the collector there is attenuation due to phonon scattering (α_c^{phonon}) and quantum mechanical reflection (α_c^{qm}). By applying a magnetic field, the magnetic state of the spin valve in the base can be controlled between the parallel and anti-parallel state. Because the scattering in ferromagnetic metals like Fe, Co, Ni and their alloys is different for spin-up and down electrons, this will result in a change of the base transmission α_b, similar as the resistance change in a normal spin valve. (all the other α's will remain constant)
A simple model can be made for this base transmission based on the Boltzmann equation. As derived in Eq. 2.48 the Boltzmann distribution decays exponentially as does the current in the 1-directional model. This is not essentially different from the 3-dimensional model, the 1-directional model only predicts a different attenuation length for a given elastic and inelastic mean free path. Based on these calculations, it appears impossible to experimentally extract the elastic and inelastic mean free path independently, in other words we will always observe only one attenuation length (per spin-channel). Furthermore, at the interfaces only the spin-dependent part is interesting, because this simple model cannot explain the current transfer anyway, and so all the spin-independent attenuation will be put into one general non-magnetic factor (α_{nm}).
In order to calculate the current transmission through the base of a NiFe/Co spin-valve transistor, we start with 50% spin-up electrons and 50% spin-down electrons, and multiply both channels with their respective transmission factors through the base (see Fig. 2.23). At the magnetic/non-magnetic interfaces with the NiFe and Co layers we introduce an interface transmission function $\Gamma_{NiFe/Co}^{\uparrow(\downarrow)}$ and in the bulk we use the spin-dependent exponential attenuation. Together with one common non-magnetic attenuation factor α_{nm} we can describe to total base transmission in the parallel state of the NiFe/Co spin valve as:

$$\alpha_b^P = \alpha_{nm} \frac{\left(\Gamma_{NiFe}^{\uparrow}\Gamma_{Co}^{\uparrow}\right)^2 e^{-t_{NiFe}/\lambda_{NiFe}^{\uparrow}} \cdot e^{-t_{Co}/\lambda_{Co}^{\uparrow}} + \left(\Gamma_{NiFe}^{\downarrow}\Gamma_{Co}^{\downarrow}\right)^2 e^{-t_{NiFe}/\lambda_{NiFe}^{\downarrow}} \cdot e^{-t_{Co}/\lambda_{Co}^{\downarrow}}}{2} \tag{2.52}$$

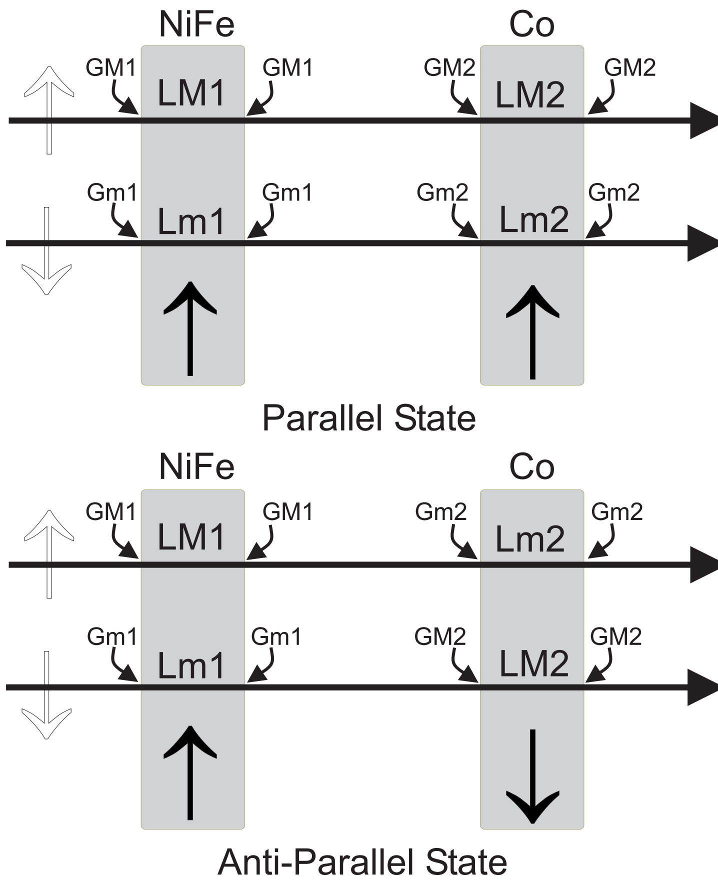

Figure 2.23: *A schematic overview of the used model for the parallel (above) and anti-parallel (below) state. (G stands for* Γ*, M=Majority=*$\uparrow$*, m=minority=*$\downarrow$ *and L denotes* λ*)*

and in the anti-parallel state as:

$$\alpha_b^{AP} = \alpha_{nm} \frac{\left(\Gamma_{NiFe}^{\uparrow}\Gamma_{Co}^{\downarrow}\right)^2 e^{-t_{NiFe}/\lambda_{NiFe}^{\uparrow}} \cdot e^{-t_{Co}/\lambda_{Co}^{\downarrow}} + \left(\Gamma_{NiFe}^{\downarrow}\Gamma_{Co}^{\uparrow}\right)^2 e^{-t_{NiFe}/\lambda_{NiFe}^{\downarrow}} \cdot e^{-t_{Co}/\lambda_{Co}^{\uparrow}}}{2}. \tag{2.53}$$

Due to its simplicity, we will use this model to fit/compare our experiments (see page 69 of the experimental chapter).
In the above models, no spin-flip scattering (due to spin-waves or Stoner spin-flip) was included, just to make the calculations more simple. But in the 1-directional approach, due to its simplicity, we can easily extend the model and include this spin-flip scattering. Until now, the spin-up current was totally independent of the spin-down current. This simplified the calculations, because the two spin channels could be treated separately. Spin-flip scattering removes an electron from spin channel σ and adds this electron to spin-channel $\bar{\sigma}$. So in order to calculate the effects of spin-flip scattering, the distribution function for both spin-up ($\sigma = +1/2\,\hbar$) and spin-down ($\sigma = -1/2\,\hbar$) electrons should be calculated simultaneously. This can be done by writing down the Boltzmann equation for both spin-channels with a coupling term that describes the spin-flip scattering (see Eq. A.50 for spin-up electrons and Eq. A.51 for spin-down electrons) and by solving these coupled differential equations, as shown in Appendix A.2.3 (page 114).

2.4 Conclusions

In this chapter, the theory behind the current transport in the spin-valve transistor is discussed. Due to its hetrostructure in which semiconducting and metallic (magnetic) materials are used, we have analyzed the current transport in two parts.
First, we have dealt with the current transport through silicon/metal contacts. At the emitter side, electrons in the Si have to come over an internal conduction bandbending, after which they are accelerated towards the silicon/metal interface by the image-force. When these electrons come into the metal, they have an excess energy of about 1eV and all of their momentum is highly forward focussed (only in the x-direction). At the collector side, hot-electrons that have passed the metallic base impinge on the silicon collector. Similar to the emitter, there is a Schottky barrier at the collector, and electrons should have enough energy to pass over the top of the barrier. Furthermore, their momentum should lie in the acceptance cone, which can be derived from energy and momentum conservation while the electron travels from the metal into the silicon.
Secondly, the transport of hot-electrons through the base is discussed. The differences between scattering of hot-electrons and electrons at the Fermi-level are analyzed, which mainly differs due to the larger (E, k) phase-space for the hot-electrons to scatter into. Hot-electrons can, for example, scatter with other electrons from below the Fermi-level, in so-called Stoner excitations, after which their excess energy is reduced. Furthermore, recent analyzes show that hot spin-down electrons can also emit spin-waves in magnetic materials. After having described the difference in scattering possibilities, a transport model for hot-electrons is made, based on the Boltzmann equation. With this model that includes both elastic (energy conserving)

and inelastic (energy loosing) scattering mechanisms, we can calculate the amount of hot-electrons with enough energy and the right momentum to pass the collector at any point inside the metallic base. When this model is applied to the spin-valve transistor, in which the scattering in the magnetic layers is spin-dependent and we assume that there is strong elastic interfaces scattering, the experimentally observed low collector current and high magnetocurrent can be explained. This model further predicts exponential attenuation with base layer thickness, but the characteristic attenuation length deviates from the simple $\left(\lambda_e^{-1} + \lambda_i^{-1}\right)^{-1}$ as expected from a one-dimensional approach. The decay is found to depend on the local angular momentum distribution of the hot electrons, which by itself is related to previous (elastic) scattering events, and the emitter and collector properties. Finally, a more simple model for the spin-valve transistor, based on the exponential attenuation, is discussed. This model is ideally suited to make comparisons between theory and experiment.

Chapter 3

Experimental procedures

In this chapter the experimental procedures to make and electrically characterize a spin-valve transistor are briefly summarized. First we describe the molecular beam epitaxy (MBE) system that is used to deposit the Pt/NiFe/Au/Co/Au spin valve and to do in-vacuum metal bonding. Then we explain the necessary processing steps to make a spin-valve transistor. And finally, we describe the measurements setup which is used to electrically characterize the made spin-valve transistors.

3.1 Deposition setup

All the depositions of the metal layers in the base of the transistor are done with a DCA Metal 600 molecular beam epitaxy (MBE) system. MBE is evaporation at ultra high vacuum (10^{-9} to 10^{-12}mbar) and at a very low rate (a rate of 1Å/sec is high and rates of 1 atomic layer/min are more common), so that every atom that comes on the substrate can migrate in order to find the most energetically favorable position. This enables the epitaxial growth of lattice matched multilayers. We have preferred MBE above sputtering, because in evaporation the deposited atoms have less energy, therefore resulting in better Schottky diodes.
The system consists of a growth chamber in which 3 effusion cells and an electron-gun evaporator (e-gun) are installed. We have Au and Cu in the effusion cells, and in the 3 crucibles of the e-gun we have Pt, $Ni_{80}Fe_{20}$ and Co. With these materials we can make: Co/Cu and NiFe/Au GMR multilayers and NiFe/(Au,Cu)/Co spin-valves. Furthermore, Pt can be used as buffer layer with a high Schottky barrier. All the deposition rates have been set to $\approx$ 0.2Å/sec, in order to grow the base layers in a reasonable time. The effusion cells are temperature regulated with a Euroterm temperature controller to $\pm$ 0.1°C, resulting in a constant flux at a certain temperature. The shutter control for the materials in these effusion cells is done on time, based on the constant deposition rate, which is regularly recalibrated. For the E-gun, a Sycon STC-200 deposition rate controller regulates the Telemark TT-6 high-voltage power supply and measures the rate and thickness of the deposited layer with a crystal monitor. The deposition chamber is pumped by an He-cryopump and a Ti- sublimation pump which can achieve a vacuum of $\approx 1 \cdot 10^{-10}$mbar (average deposition pressure $\approx 5 \cdot 10^{-10}$mbar). The double walls of the chamber are cooled with liquid nitrogen (T=77K) to ensure a good vacuum and to prevent the heating of the substrates during the deposition. The load-lock that is used to transport samples to the deposition chamber is pumped by a 75KRPM turbopump with behind that a dry-scroll fore-vacuum pump.
In order to operate the MBE system more easily it is connected to a PC on which a special program was developed under LabView 5 from National Instruments. This program controls the MBE system and has a built-in database of the different materials and their corresponding deposition parameters. Based on these values the program can automatically deposit a selected material with a certain thickness.

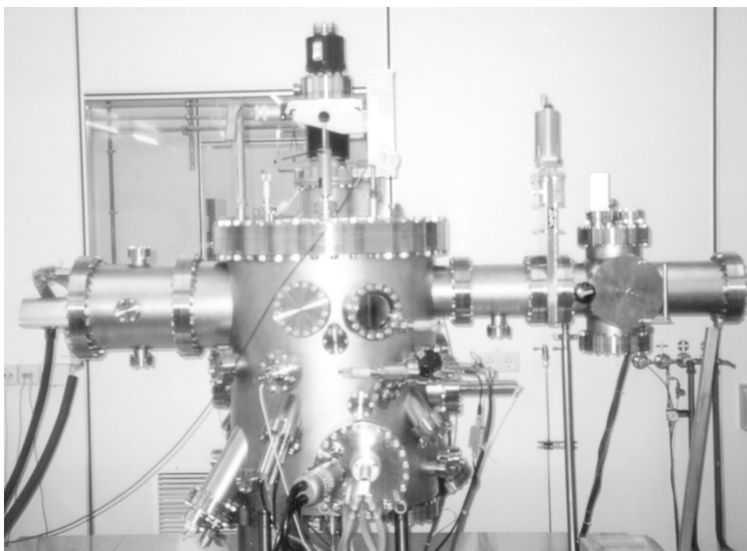

Figure 3.1: *The MBE system showing the deposition chamber with at the bottom the effusion cells and electron gun evaporator and at the right the load-lock.*

3.2 Spin-valve transistor processing

As explained in the theory chapter, the spin-valve transistor relies on good Schottky diodes to inject hot-electrons. Furthermore, it is important that the collector diodes show low leakage. Therefore, we need single-crystalline silicon at both the emitter and collector. In order to obtain this, one can try to grow a silicon layer on top of a metal, but it will grow amorphously. Increasing the temperature is generally the way to get a better silicon growth, because it will give the silicon atoms a higher mobility at the surface, but due to the combination of metal and silicon this will only result in silicide formation[1] and interface diffusion. This is why a bonding technique was developed [83], in which two monocrystalline wafers on which a metal layer is deposited (evaporated/sputtered) are brought together by a bondingrobot (see Fig. 3.2). Because this method operates at ultra-high vacuum, the freshly deposited atoms will make atomic bonds and make the two wafers inseparatable. After this bonding step, several processing steps are needed to make a connectable spin-valve transistor from this bonded structure.
In this section we summarize the steps to make a spin-valve transistor. All the processing steps described below are done in the class 100 cleanroom facility of the MESA$^+$ research institute and a complete step by step processing list can be found in Appendix A.4 (page 118).

1 The only epitaxial transistor that were grown are Si/$CoSi_2$/Si structures [82]. This $CoSi_2$ is metallic, therefore resulting in a type of metal base transistor.

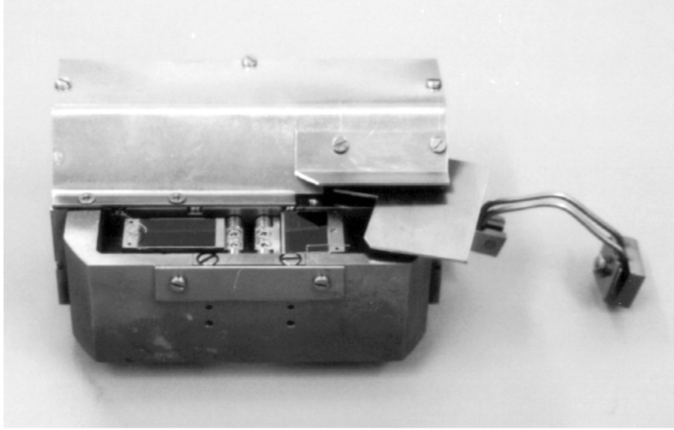

Figure 3.2: *The bondingrobot with its two arms that can move to each other resulting in the in-vacuum metal bonding. Mark the special shutter on the right, which allows us to have a different Schottky barrier at the emitter than at the collector side.*

Wafer preparation

The wafers we use for the emitter are Silicon On Insulator (SOI) wafers, because the built-in oxide layer provides an easy etch stop in the emitter thinning stage. The device layer of these SOI wafers is 2.5μm thick and has a low n-type doping ($N_d \simeq 10^{16}$cm^{-3}, to obtain a good Schottky diode) on the bonding side and a high doping ($N_d \simeq 10^{21}$cm^{-3} to make an ohmic contact) on the other side. The first 30nm of these wafers is oxidized and protected by a 3.5μm thick photoresist before they are sawn into pieces that fit on the bondingrobot.

For the collector we use double sided polished (DSP) Si wafers with a low n-type doping ($N_d \simeq 10^{16}$cm^{-3}). These wafers are oxidized like the emitter wafers and on the backside a $\approx 1\mu$m thick Si_3N_4 protection layer is deposited by plasma enhanced chemical vapor deposition (PECVD). This layer will protect the backside during the thinning stage of the emitter. Finally also these wafers get a photoresist protection layer and will be sawn to fit on the bondingrobot.

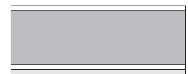

Cleaning and Bonding

Before the two wafers can be bonded, they should be thoroughly cleaned. For this, both wafers are taken from the backside by a vacuum pipet and are chemically cleaned as following. First, the wafers are clean by HNO_3 to remove the protecting photoresist and other organic contaminants. Second, the thin layer of native oxide ($\approx$ 2nm) on the Si particles that emerged at the sawing stage is removed with HF 1%. These Si particles can now be etched away with 5% TMAH (tetramethylammonium hydroxide), an IC-compatible silicon etchant. Finally, the 30nm oxide layer is removed by HF 50% and the samples are mounted on the bondingrobot.

Next, this robot is transferred within 5 minutes into the loadlock of the MBE (molecular beam epitaxy) machine, where we pump down to a pressure of $\approx 1 \cdot 10^{-6}$mbar. At this pressure we open the main valve and transfer the robot to the main deposition chamber with a vacuum of $\approx 5 \cdot 10^{-10}$mbar. Here, the Pt buffer layer and the spin valve (NiFe/Au/Co) are deposited on the emitter wafer. After which we remove the small shutter of the robot and deposit a Au layer on both the emitter and collector wafer, while bringing the two wafers into contact, resulting in the in-vacuum metal bond.

Emitter thinning

After having obtained the bonded structures, we have to thin down the emitter wafer, because in order to make an emitter block with small lateral dimensions, its height should be even smaller. This is due to the limited aspect ratio of the etching procedure that is used to define these emitter blocks. This thinning is done with 10% TMAH, which etches $\approx 1\mu$m/min at T=85°C, so about 6 hours are needed to etch through the SOI handel wafer. During this etch, the backside of the collector is protected by the Si_3N_4 layer. Although the thinning process takes 6 hours, it stops automatically on the buried oxide layer, resulting in a convenient and reliable process.

Emitter definition
Next is to define the emitter by photolithography. The SiO_2 etch stop layer of the SOI wafer is patterned with photoresist around which all the oxide is etched away with BHF. After removing the photoresist, we etch all the unprotected Si around the emitter with 10% TMAH at T=85°C, that stops on the metallic base. This finally results in emitter blocks with on top an oxide layer and a base layer that is ready to be patterned.

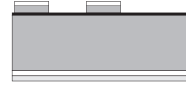

Base definition
The base is defined with photoresist and etched with an ion-beam. We have chosen an ion-beam process, because this can easily etch the various metals in one run. A disadvantage of ion-beam etching is the damage it does to the underlying silicon, which probably becomes highly doped with the metal impurities or amorphous due to the high energy of the ions. This damage results in a high leakage current of the collector diodes and can only be repaired by etching the damaged silicon away.

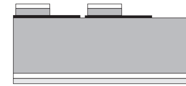

Contact metallization
The final step in the processing is to make the metallizations for the emitter and collector contacts. For the emitter contacts, we define holes in a photoresist layer on top of the emitters, through which we etch with BHF the oxide below. For the collector contact, a hole in the photoresist is left to make an direct 'ohmic' contact on the silicon at the collector side. Next, a Cr/Au metallization layer is deposited by DC-magnetron sputtering followed by a lift-off process of all the Cr/Au with photoresist under it. The remaining Cr/Au inside the hole in the emitter oxide will serve as emitter contact and the big Cr/Au pad as collector contact.

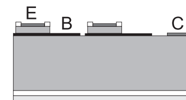

After all these processing steps, a chip with spin-valve transistors like shown in Fig. 3.3 is obtained. These chips are glued on a printed circuit board (PCB) so that we can make wirebonds between the PCB and the emitter, base and collector of the sample. In this way we can conveniently connect a certain spin-valve transistor and measure it. Although, for this thesis only devices made as described above are used, research also focuses on the miniaturization of the spin-valve transistor. Recently, we have succeeded in making spin-valve transistors with an emitter size downto 10$\sim$ 25μm [84]. At these sizes, no wirebonds can be made directly onto the emitter. Therefore, two extra processing steps are needed to deposit an insulating layer and to make contactpads, as can be seen in Fig. 3.4.

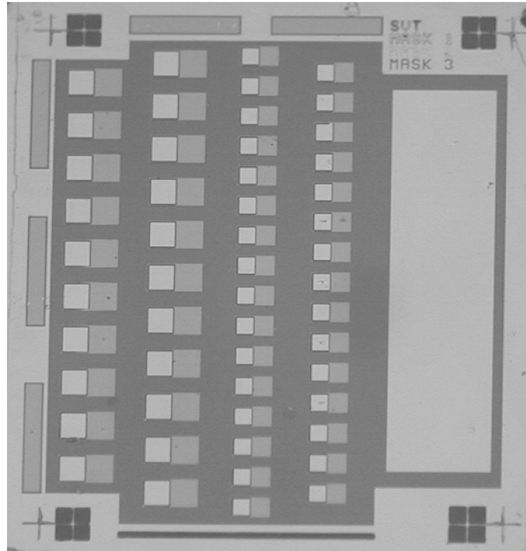

Figure 3.3: *An optical image of a chip with 52 spin-valve transistors. On the left side of the photo, 2 rows of SVT's with 500x500 μm^2 emitters and bases of 1000x500 μm^2 are shown. Right to these, slightly smaller devices with a 350x350 μm^2 emitter and 750x350 μm^2 base are shown. The big pad on the right is the common collector contact.*

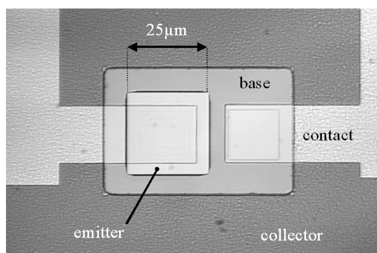

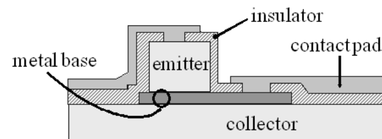

Figure 3.4: *On the left, a microscope image of a spin-valve transistor made with the new processing. On the right, a schematic cross-section of this structure.*

3.3 Electrical transport measurement setup

The measurement setup to characterize the spin-valve transistor consists of different measurement devices, that are controlled by a PC running Labview 5 (see Fig. 3.5). Several programs have been written in Labview to measure the different elements of the spin-valve transistor. The possibilities are: measuring the I-V characteristics of both the emitter and collector Schottky diode, measuring the resistance of a thin film versus magnetic field and of course measuring the collector current vs. magnetic field and the collector current vs. emitter current. All these measurements can be done automatically as function of the temperature, because the sample holder is temperature regulated (see Fig. 3.6) by an Oxford Instruments ITC4 PID controller, which can regulate the sample temperature from 77K to 350K within 1K.
The measurement of a spin-valve transistor is done by connecting a Keithley 2400 between the emitter and base, in order to source a constant emitter current and a Keithley 236 between the base and the collector, in order to measure the collector current (see Fig. 3.6 for a schematic diagram).
The Keithley 2400 is a source/measurement unit capable of sourcing a voltage (from 10μV to 210V) or current (50pA .. 1.05A) and concurrently measuring the resulting current (down to 10 pA) or voltage (down to 1μV). In the case of spin-valve transistor measurements, the Keithley 2400 is used to provide the constant emitter current, but can also be used to characterize the emitter Schottky diode and make 2 or 4-wire resistance measurements with a DC current [85].
The Keithley 236 is a source/measurement unit similar to the Keithley 2400, but more sensitive. It can measure currents down to 10fA. In order to measure these low current levels all connectors are fully guarded and shielded using triax cables. We only use

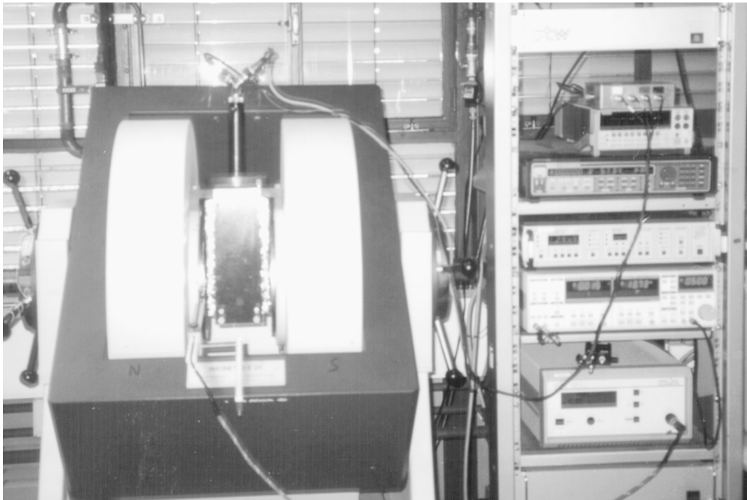

Figure 3.5: *The measurement setup, clearly showing the electromagnet on the left and the measurement equipment on the right. The sample is mounted between the pole shoes of the electromagnet in a small home-build cryostat.*

coax cables in the measurement setup with on the inner wire the signal and on the outer mantle the guard. In this way the buffer amplifier in the Keithley 236 assures the same voltage on the outer mantle as on the signal wire, resulting in a low wire-leakage of 1pA in the 2 meter long cables. This 1pA is the measurement limit down to we can measure the collector current, and suffices for all the different kinds of spin-valve transistors that have been made. Furthermore, the Keithley 236 can also be used to characterize the collector barrier, like the Keithley 2400.
In order to generate a magnetic field, a Bruker electromagnet is used that can sweep the magnetic field from -10.000 to 10.000 Oe with steps of 0.3 Oe. This magnet generates a uniform magnetic field over a large region, providing plenty of space for the cryostat and the sample. The magnetic field generated by the electromagnet is measured by a F.W. Bell model 9500 Gaussmeter with a resolution of 0.1Oe.

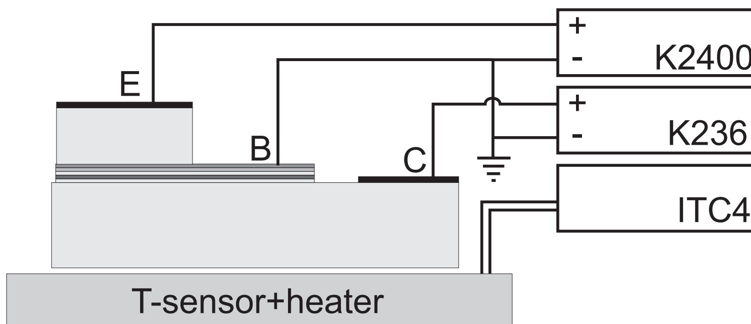

Figure 3.6: *The connections between the spin-valve transistor and both Keithley's with below the temperature controller. Note, in order to inject electrons from the emitter into the base, we have to source a negative current with the Keithley 2400.*

3.4 Conclusions

In this chapter the experimental procedures to make and electrically characterize spin-valve transistors were briefly discussed. Spin-valve transistors are made by bonding two silicon substrates with a robot that brings the substrates into contact while depositing the spin valve. These bonded wafers are patterned and etched in the MESA$^+$ cleanroom, resulting in chips with 52 spin-valve transistors with a yield of over 90%. A DCA 600 metal MBE system is used to deposit the spin valve in the base and is controlled with a deposition program written in Labview. The measurement setup is also controlled by Labview and is capable of measuring all the important parameters of the spin-valve transistor as function of temperature and magnetic field.

Chapter 4

Experimental results

In this chapter we will characterize experimental spin-valve transistors and compare these to the current transport theory. First the I-V characteristics of Schottky diodes are discussed. Next we analyze the hot-electron emission and collection properties of these diodes by comparing different metal base transistors (MBT's), which have the same Si/metal/Si structure as the spin-valve transistor, but without magnetic materials in the base. After that, we show how the collector current of the spin-valve transistor depends on the magnetic field and temperature, and analyze how it is related to the Schottky barriers and to the scattering in the magnetic layers. By making different transistors we were able to measure the spin-dependent scattering lengths in NiFe and Co and their temperature dependence. Finally, we present a new model that perfectly describes the experimental results.
All the transistors as discussed in this thesis are summarized in Appendix A.5 (page 126)

4.1 Current transport in Schottky diodes

As derived in chapter 2, the I-V characteristics of a perfect Schottky diode on Si with an n-type doping of $\approx 10^{16}$ cm^{-3} can be described by Eq. 2.15 from the thermionic emission theory. Experimental I-V characteristics slightly deviate from this theoretical dependence and are generally fitted with [47]:

$$I_{diode} = Area \cdot A^{**} \cdot T^2 \exp(-\frac{q\Phi_B}{kT}) \left[\exp(\frac{qV}{nkT}) - 1 \right] \quad (4.1)$$

In which the ideality factor n, is a measure of how well the current-voltage characteristic follows the thermionic emission theory (an ideal diode will give $n \equiv 1$). Many structural factors at the metal-semiconductor interface and in the bulk of the semiconductor can result in deviations from thermionic emission theory. Electronically, one can divided them into the following effects [86]:

- Change of barrier height with applied voltage.
  Due to the image-force (see page 18), the maximum of the Schottky barrier lies inside the semiconductor and is slightly bias dependent. This results in every Schottky diode for at least an ideality factor of $n \approx$ 1.01-1.02.
  Interfacial layers will result in an extra potential step that makes the barrier height voltage dependent, surface states will reduce this effect slightly, but an above 1 ideality factor will be observed [87, 88].

- Current transport over non-uniform barrier.
  When the barrier height is not uniform, but rather distributed, this will result in different I-V characteristics. A comprehensive model of the current transport over non-homogeneous Schottky barriers has been developed by Tung [89], that assumes a constant barrier with on top of that, patches with lower barriers, resulting in a different voltage dependence with an above 1 ideality factor [90].

- Change of current transport regime.
  When the doping level is too high, the Schottky barrier can become to thin,

resulting in thermionic field emission or even field emission *through* the barrier [91]. This change in current transport regime gives a high n factor.

In Fig. 4.1 (A), the measured I-V characteristic of a Schottky diode is plotted on a semi-log scale. From these measurements, one can determine the barrier height and ideality factor from a fit of the forward characteristics (where $V > 3kT/q$) with a straight line. The Schottky barrier height can be calculated based on the current offset (I_0) at zero applied bias:

$$q\Phi_B = -kT \ln \left[\frac{I_o}{Area \cdot A^{**} \cdot T^2} \right] = 0.805 \pm 0.01 \, eV \tag{4.2}$$

and the ideality factor can be calculated based on the slope of the straight line:

$$n = \left[\frac{kT}{q} \frac{d(\ln I_{diode})}{dV} \right]^{-1} = 1.02 \tag{4.3}$$

Furthermore, one can see in Fig. 4.1 (A) that the forward current is limited by the series resistance of the ohmic contact in region 1 (from 0.35 to 0.72 V) and by the current compliance of the power supply (2mA) in region 2 (from 0.72 to 1V). The reverse characteristics are almost flat, as described by Eq. 2.15, and the slight increase with higher reverse bias comes from the image force lowering. This Schottky barrier behaves quite ideal. Sometimes more leakage is measured in the reverse characteristics when the repairing process (see page 55 and 123) is less successful.
When a Schottky diode is cooled down, the reverse bias current should rapidly decrease ($\approx$ 3 orders of magnitude within 50°C) based on the thermionic-emission theory. In most of the diodes the leakage current drops rapidly to below the detection limit of the measurement setup, but in some, the leakage current drops down to a temperature independent leakage current that is related to defects (most probably at the

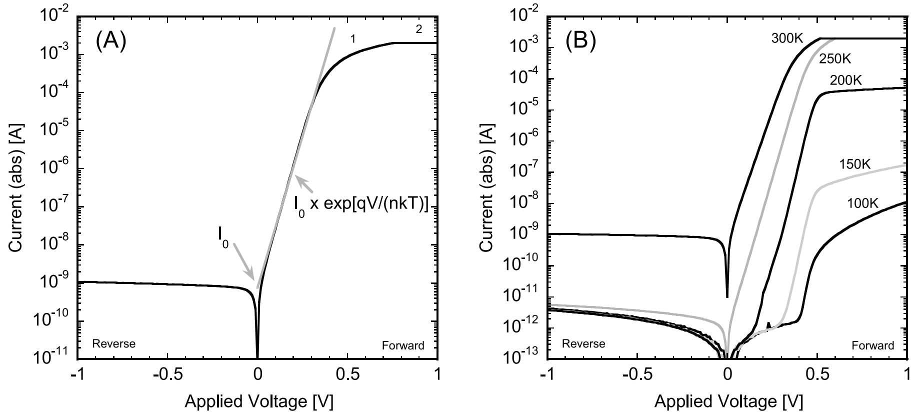

Figure 4.1: *(A) Semi-log plot of the absolute value of the diode current vs. the applied voltage of a typical Si/Au Schottky diode (RSVTN1) with an area of $700 \times 350\mu m^2$ at T=300K. (B) I-V characteristics of a Schottky diode (RSVTN3) at different temperatures (T=100, 150, 200, 250 and 300K).*

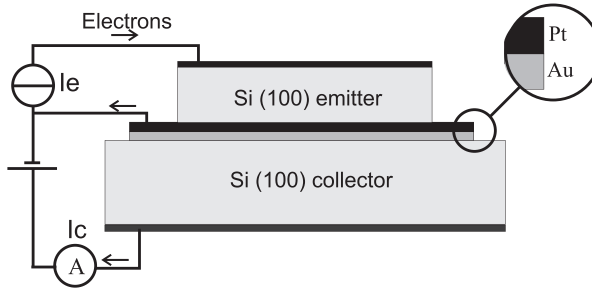

Figure 4.2: *The schematic device structure of a Si/Pt/Au/Si metal base transistor.*

edges due to the ion beam processing), as shown in Fig. 4.1 (B). The I-V characteristics of this defect leakage are linear, so like a resistance that is in parallel with the Schottky diode. The measured forward characteristics in Fig. 4.1 (B) change remarkably at low temperature, due to the ohmic contact (a large Cr/Si contact on a rough surface that is in reverse bias, see contact metallization in the SVT processing section of chapter 3) that limits the current through the Schottky diode [1].
But when the Si/Au Schottky diode of RSVTN1 is cooled down, the current offset and the slope of the forward characteristics remain well explained by the thermionic-emission theory, resulting in a constant barrier height and ideality factor. In some diodes, the barrier height decreases and the ideality factor increases with decreasing temperature, showing a deviation from pure thermionic-emission. It is important that the current transport is by thermionic-emission over the maximum of the Schottky barrier, because we rely on the emission of hot-electrons in the spin-valve transistor.

4.2 Hot-electron emission and collection in metal base transistors

A metal base transistor is a 3-terminal device, with a semiconducting emitter and collector and a metallic base. We have made these devices with a silicon (100) emitter and collector and a Pt/Au base, as schematically depicted in Fig. 4.2. With these metal base transistors, we can analyze the emission and collection of hot-electrons by Si/Pt and Si/Au Schottky diodes and get more insight in the scattering processes in a non-magnetic base.
In normal operation, a voltage is applied over the emitter and base (V_{eb}), in order to inject electrons over the Si/Pt Schottky barrier ($q\Phi_b \approx 0.9$eV) into the base. These electrons are so-called hot-electrons, with an excess energy of about 1eV (0.9eV + 2$\sim$3kT) above the Fermi-level in the base. Next, these hot-electrons travel through the Pt and Au layers of the base, where momentum and energy of the hot-electrons can change in respective elastic and inelastic scattering events. At the Au/Si collector barrier of $\approx$ 0.8eV, which is zero biased ($V_{cb} \approx 0$), only those electrons with enough

1 This Si/Au Schottky diode is used on the collector side of the spin-valve transistor, which is 0 or reverse biased. So the ohmic contact is in this situation forward biased and will not limit the collector current.

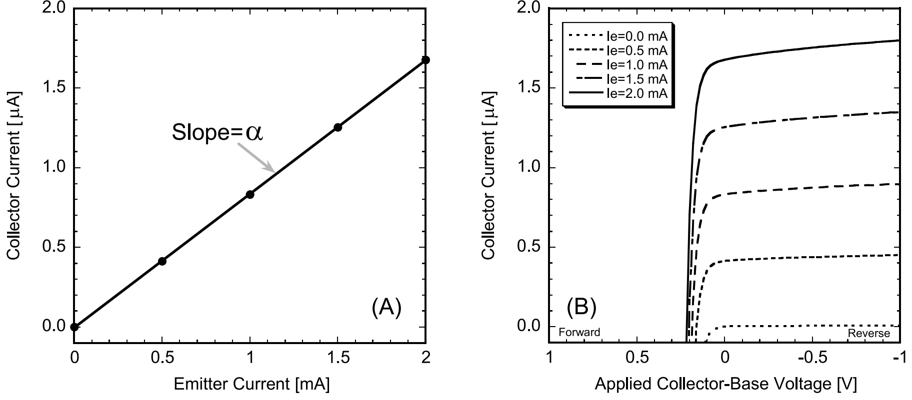

Figure 4.3: *(A) The linear relation between the collector current and the emitter current of a Si(100)/Pt 40Å/Au 20Å//Au 20Å/Si(100) metal base transistor (SVTK6) at room temperature. (B) The common base characteristics of this MBT, in which the collector current is measured as a function of the applied collector-base voltage for different emitter currents.*

energy and the right momentum can come in the collector. So from the emitter current (I_e), only a small fraction contributes to the collector current (I_c), this fraction is called the current transfer ratio (α) and is defined by: $\alpha \equiv I_c/I_e$.
In Fig. 4.3 (A), this current transfer is measured in a Si/Pt/Au/Si transistor by increasing the emitter current and measuring the collector current under zero bias. From the slope of this plot, a current transfer of $\alpha = 8.4 \cdot 10^{-4}$ (I_c=1.67μA at I_e=2mA) is obtained. Furthermore, we can measure the dependence of the collector current on the collector-base voltage in a so-called common base measurement, as shown in Fig. 4.3 (B). When no current is injected at the emitter, only the I-V characteristics of the collector Schottky diode are measured. By injecting an emitter current I_e, a fraction $\alpha \times I_e$ is added to the collector current. The slight increase of the collector current with negative bias voltage (V_{cb}) is due to image force lowering of the collector barrier, letting over more current (making α slightly bias dependent). When the collector diode is positively biased, the forward current of the Schottky diode opposes the hot-electron current and the total is reduced (and changes sign).
So the total collector current can be written (without image force effects) as:

$$I_c^{total} = \alpha \times I_e(V_{eb}) + I_{diode}(V_{cb}) \tag{4.4}$$

In which α is actually a very complicated factor related to the injection characteristics of the emitter, the transport properties in the base and the collection characteristics of the collector:

$$\alpha = \left[\alpha_e^{phonon}\right] \times \alpha_b \times \left[\alpha_c^{qm} \times \alpha_c^{phonon}\right] \tag{4.5}$$

So are α_e^{phonon} and α_c^{phonon} due to optical-phonon scattering (see page 22 and 24) in the respective emitter and collector, and is α_c^{qm} due to quantum mechanical reflections (page 24) at the collector barrier. The α_b is a combination of bulk scattering and

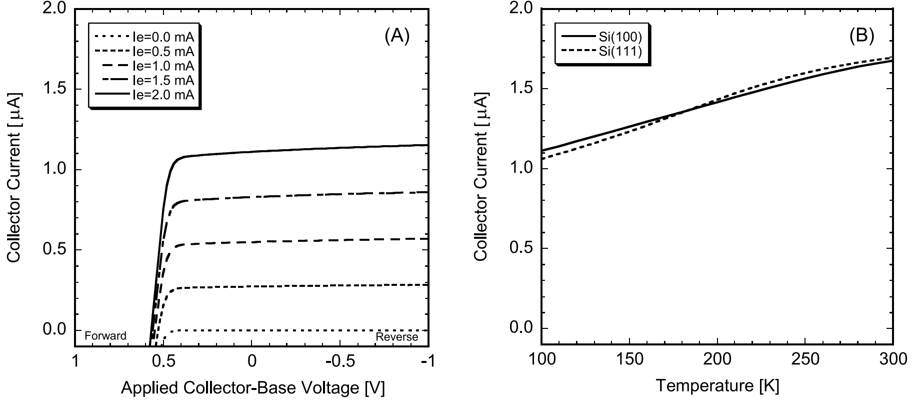

Figure 4.4: *(A) The common base characteristics of SVTK6 at 100 Kelvin. (B) The temperature dependence of the collector current for V_{cb}=0V and I_e=2mA of SVTK6, which has a Si(100) collector and SVTK1, which has a Si(111) collector. Both SVTK1 and 6 have a Si(100) emitter and the same Pt 40Å and Au 20+20Å base.*

interface scattering in the metallic base of the transistor. This scattering lowers the electrons energy below the collector barrier or its momentum outside the acceptance cone, resulting in an attenuation of the collector current, as explained in the theory chapter (see section 2.2.3, page 34).
When the metal base transistor is cooled down to 100K, we measure Fig. 4.4 (A), which is similar to Fig. 4.3 (B), but with a smaller current transfer ($\alpha = 5.6 \cdot 10^{-4}$). This is quite unexpected, because at a lower temperature there is generally less *scattering*[2], and so more current should have come through the metal base transistor. If we look at the temperature dependence, as shown in Fig. 4.4 (B), an about linear increase in current transfer is shown over the T=100 to 300K range. Furthermore, one can see in Fig. 4.4 (B) that there is almost no difference in the collector current between devices made with a Si(100) or Si(111) collector, like in some BEEM experiments [55].
The increase of collector current with temperature should be related to the injection and collection characteristics of hot-electrons by Schottky diodes, because different combinations of Schottky barriers, as shown in Fig. 4.5, result in different slopes in the temperature dependence. In order to compare the temperature dependence of different transistors we have used the normalized current transfer, which is defined as the current transfer relative to the T=100K value: $\alpha^{norm}(T) \equiv \alpha(T)/\alpha(T = 100K)$.

As shown in Fig. 4.5, the temperature dependence is related to the barrier height difference between the emitter and the collector. The Au/Au metal base transistor has the steepest temperature dependence and only a Schottky barrier difference of 0.06eV

2 Reducing the temperature should result in less phonon scattering in the emitter and collector, resulting in a higher α_e^{phonon} and α_c^{phonon}. Furthermore, a higher α_b is expected, due to the longer attenuation lengths at lower temperatures [92]

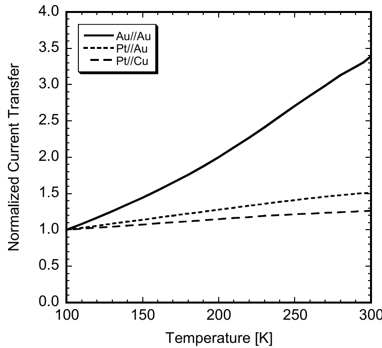

MBT	Au//Au	Pt//Au	Pt//Cu
Sample	OSVT10	SVTK6	OSVT15
$\alpha(100K)$	$3.5 \cdot 10^{-3}$	$5.5 \cdot 10^{-4}$	$3.4 \cdot 10^{-3}$
$q\Phi_e$ [eV]	0.80	0.86	0.86
$q\Phi_c$ [eV]	0.74	0.75	0.72
$\triangle q\Phi$[eV]	0.06	0.11	0.14

Figure 4.5: *On the left, the normalized current transfer (α^{norm}) as function of the temperature for 3 different metal base transistors, with different combinations of the Schottky barriers. On the right the Schottky barrier heights and their differences for the 3 different metal base transistors.*

[3] and the Pt/Cu is almost flat and has the highest Schottky barrier difference (0.14eV). Therefore, this increase of the current transfer should be related to the energy electrons get when injected from the emitter (which depends on temperature, as can be seen in Eq. 2.17 and Fig. 2.4), and how their energy and momentum is changed when these electrons come at the collector side. Two regimes can be easily analyzed, the first without elastic scattering and the second with strong elastic scattering.
In the first case, there is only inelastic scattering in the base and so the angular distribution will remain the same through the base. Therefore, no temperature dependence in the collector current will be observed (related to the Schottky barriers), because every electron is emitted from a state in the Si emitter, and as long as its momentum is not changed, will be able to find a state in the Si collector. Only when the emitter barrier is below the collector barrier, there will be an increase of current transfer with temperature. This effect is also found when the emitter and collector are non-uniform (distributed) Schottky barriers, as is calculated in Appendix A.1.4.2 (page 107).
In the second case, there is a large amount of elastic scattering, resulting in an almost isotropic momentum distribution at the collector. In this case, the electrons can only be collected when their momentum falls within the acceptance cone. Because the acceptance cone angle depends on the hot-electron energy (see Eq. 2.24), this results in an increase of collector current with temperature. In order to calculate the exact temperature dependence of the collector current, a complete momentum analysis, like in the Boltzmann model, has to be done. A more simple way is by assuming that the momentum distribution has become totally isotropic, so that a simple analytic formula can be obtained to describe this effect (see Appendix A.1.4.1 on page 106). Both calculation methods show the typical linear increase of collector current with

3 It should be noted, that the lower barrier height as measured at the collector is probably due to defects at the edges, that change the current transport, resulting in higher n and lower Φ_b. Therefore, the real Schottky barrier height difference in the undamaged regions might even be smaller.

temperature, in which the slope appears to depend on the difference in Schottky barrier height. Furthermore, the Boltzmann model shows that the slope is also related to how isotropic the momentum distribution has become (the more isotropic, the higher the slope, with a maximum slope defined by the analytical model).

Coming back to the measurements, we conclude that the experimental temperature dependence agrees most with the isotropic momentum distribution model (which results in a linear increase with temperature). But, it is possible that both effects are present in experimental metal base transistors [4].

4.3 Hot-electron transport in the spin-valve transistor

In this section, we start explaining the basic spin-valve transistor characteristics, after which in the following sections we go into more detail on how the collector current depends on temperature, layer thickness and how this is related to the various scattering mechanisms in the base.

The spin-valve transistor is, beside the spin valve in the base, quite similar to the metal base transistor. Hot-electrons are injected from the emitter and only electrons with enough energy and the right momentum can contribute to the collector current. This means that the influences of the Schottky barriers and the non-magnetic materials on the current transfer are exactly the same. The inclusion of magnetic materials in the base results in a difference in transport properties for spin-up and spin-down electrons. By including a spin valve, consisting of two magnetic layers that are decoupled by a non-magnetic spacer, these differences result in a high current transfer when the magnetic layers are magnetized parallel (P) and a low transfer when magnetized anti-parallel (AP). The total current transfer in a spin-valve transistor is described by Eq. 4.5, with a different α_b for the parallel state (α_b^P) and the anti-parallel state (α_b^{AP}), which can be modelled (see Eq. 2.52 and 2.53) in the case of a Pt/NiFe/Au/Co/Au transistor as:

$$\alpha_b^P = \alpha_{nm} \frac{\left(\Gamma_{NiFe}^{\uparrow}\Gamma_{Co}^{\uparrow}\right)^2 e^{-t_{NiFe}/\lambda_{NiFe}^{\uparrow}} \cdot e^{-t_{Co}/\lambda_{Co}^{\uparrow}} + \left(\Gamma_{NiFe}^{\downarrow}\Gamma_{Co}^{\downarrow}\right)^2 e^{-t_{NiFe}/\lambda_{NiFe}^{\downarrow}} \cdot e^{-t_{Co}/\lambda_{Co}^{\downarrow}}}{2} \tag{4.6}$$

$$\alpha_b^{AP} = \alpha_{nm} \frac{\left(\Gamma_{NiFe}^{\uparrow}\Gamma_{Co}^{\downarrow}\right)^2 e^{-t_{NiFe}/\lambda_{NiFe}^{\uparrow}} \cdot e^{-t_{Co}/\lambda_{Co}^{\downarrow}} + \left(\Gamma_{NiFe}^{\downarrow}\Gamma_{Co}^{\uparrow}\right)^2 e^{-t_{NiFe}/\lambda_{NiFe}^{\downarrow}} \cdot e^{-t_{Co}/\lambda_{Co}^{\uparrow}}}{2} \tag{4.7}$$

In these equations all the scattering in the non-magnetic Pt and Au layers is expressed by α_{nm}, so that we can focus on the scattering processes on the interfaces and the bulk of the magnetic layers. In these magnetic layers we have to calculate the transmissions for spin-up and down electrons separately (two current model, see page 28) and finally add them to obtain the total current transmission. At the interfaces, $\Gamma^{\uparrow(\downarrow)}$ describes the transmission through a magnetic/non-magnetic interface when the electron spin is in the same (opposite) direction as the layers magnetization. In the bulk of every layer

4 The distribution in Schottky barrier heights results in a larger change of the hot-electron energy with temperature (see Fig. A.4) and so a larger change in acceptance cone angle.

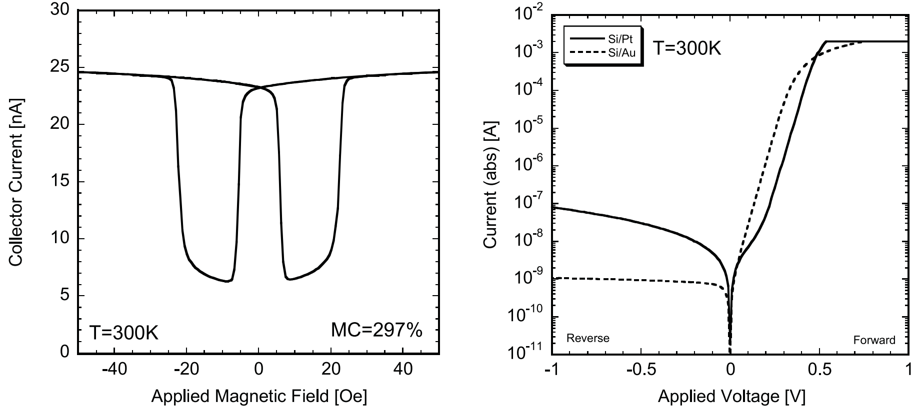

Figure 4.6: *On the left: The collector current vs. applied magnetic field in RSVTN1 resulting in a magnetocurrent of 297% at room temperature (I_e=2mA and V_{cb}=0V). On the right, the I-V characteristics of the Si/Pt emitter diode ($q\Phi_e$=0.87$\pm$0.02eV and n_e=1.06) and Si/Au collector diode ($q\Phi_c$=0.806$\pm$0.01eV and n_c=1.02) of RSVTN1.*

there is exponential attenuation, with a characteristic length $\lambda^{\uparrow(\downarrow)}$ when the spin of the hot-electron is aligned (oppositely) with the magnetization. The relative change in the collector current (I_c) is expressed in the magnetocurrent (MC), which is defined as:

$$MC \equiv \frac{I_c^P - I_c^{AP}}{I_c^{AP}} = \frac{\alpha_b^P - \alpha_b^{AP}}{\alpha_b^{AP}} \tag{4.8}$$

and can be up to several 100%'s at room temperature. It should be noted that the MC in experimental spin-valve transistors is not only sensitive to scattering, but also to parasitic collector diode leakage (leakage current is added to both I_c^P and I_c^{AP}, thus reduces the MC) and to incomplete switching (if the anti-parallel state can not be fully obtained, due to the switching properties of either the soft or hard magnetic layer, a higher I_c^{AP} is measured and so a lower MC is obtained). This explains why we have chosen Pt and Au as the materials for the Schottky diodes, because these result in high Schottky barriers with a low leakage current. Moreover, we have chosen to use an uncoupled spin valve, i.e. NiFe/Au/Co, instead of an anti-ferromagnetically coupled multilayer, $(Co/Cu)_n$ to be sure to have a well defined anti-parallel state.
The dependence of the collector current versus the applied magnetic field in an experimental spin-valve transistor is shown in Fig. 4.6, when a current of 2mA is injected into the base at room temperature. This spin-valve transistor (RSVTN1) consists of a Si(100) emitter and collector and a base consisting of: Pt 30Å/$Ni_{80}Fe_{20}$ 30Å/Au 44Å/Co 30Å/Au 22Å//Au 22Å. The Si/Pt and Si/Au Schottky diodes serve as emitter and collector with a respective barrier height of 0.87 and 0.806 eV, like in a metal base transistor. The NiFe layer is soft magnetic and is magnetically separated from the harder Co layer by a Au spacer layer, making a spin valve that can be switched between the parallel and anti-parallel state. When a magnetic field of -50 Oe is applied, both magnetic layers will point in the applied field direction, and so the spin valve is in the parallel state, resulting in a collector current of 24.6nA. When we reduce the mag-

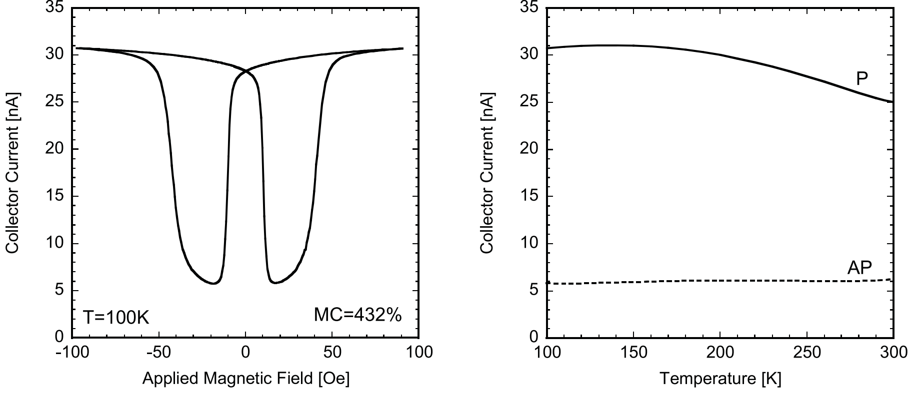

Figure 4.7: *On the left: The collector current vs. applied magnetic field in RSVTN1 when an emitter current of 2mA is injected at T=100K. On the right: The temperature dependence of the collector current in the Parallel and Anti-Parallel state.*

netic field to zero, the spin valve remains in this state, but when a small positive field is applied, the soft magnetic NiFe layer switches at its coercive field of H_c^{NiFe} ≈6 Oe. This results in a decrease in collector current to 6.3nA, because an anti-parallel state is obtained. By further increasing the magnetic field, also the Co layer with its higher coercivity of H_c^{Co} ≈22 Oe will align it self with the applied magnetic field, resulting again in a parallel state. When sweeping back to -50 Oe, the NiFe layer first switches at an applied field of -6 Oe and the Co at a field of -22 Oe. The switching as observed in this NiFe/Au/Co spin valve system can be described reasonably well by a Stoner-Wolhfarth model, as explained in more detail in Appendix A.3 (page 116).
As can be seen, the parallel state can always be obtained in a controllable way, by applying a field above the coercivity of the Co layer. But the anti-parallel state is more difficult to obtain, because the switching field distribution of the NiFe and the Co sometimes overlap. This means that the switching of the Co begins before the NiFe layer is totally switched, resulting in a typically curved[5] 'anti-parallel' state in which the full anti-parallel state is not obtained.
When the spin-valve transistor is cooled down to 100K, the collector current in the parallel state increases to I_c^P=30.6nA and in the anti-parallel state reduces to 5.8nA, as can be seen in Fig. 4.7. This results in a higher MC of 432% compared to the 297% at room temperature. The temperature dependence of the collector current is quite different compared to the observed temperature dependence in the metal base transistors (see section 4.2). Only at low temperatures (T=100-140K) we still observe a slight increase of collector current with temperature, which is also in these spin-valve transistors related to the Schottky barriers. But at higher temperatures the parallel collector current clearly decreases, which should be due to scattering. This scattering should take place in (or on the interfaces of) the magnetic layers, because only when there are magnetic materials in the base such a behavior is observed.

5 If a 100% anti-parallel state is obtained, a flat state (plateau) is observed.

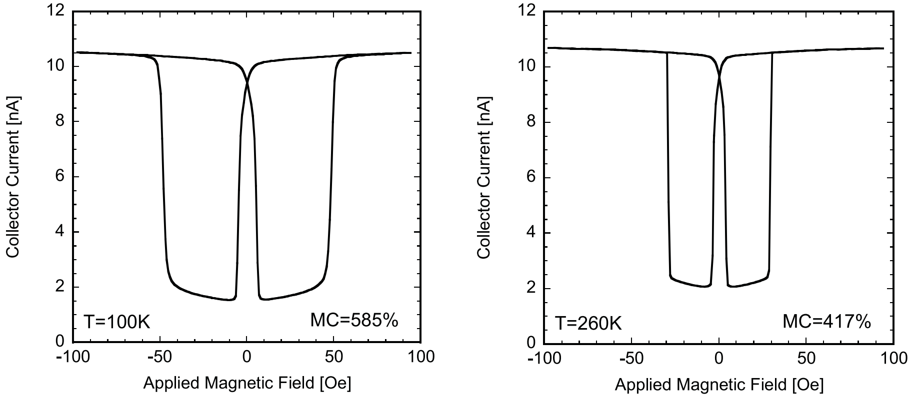

Figure 4.8: *The collector current versus applied magnetic field of RSVT8. I_e=2mA at T=100K (Left) and T=260K (Right)*

4.3.1 Spin-wave scattering in magnetic materials

In order to analyze the scattering mechanisms behind the temperature dependence of the collector current, we have to be sure that no parasitic effects affect the measurement. As shown in Fig. 4.7, the switching properties of NiFe and Co in SVTR1 have changed by cooling it down and result at low temperatures in an incomplete anti-parallel state, thereby reducing the magnetocurrent. (An error of 1nA in the collector current of SVTR1 for the anti-parallel state, increases/reduces the MC with $\approx 100\%$!) Therefore, we have selected RSVT8, a spin-valve transistor with 60Å of NiFe and 30Å of Co which are really well magnetically separated and exhibit a small switching field distribution ensuring a perfect anti-parallel state over the whole temperature range, as shown in Fig. 4.8. This transistor has a much larger increase of collector current with temperature, as can be seen in Fig. 4.9, due to the smaller difference in Schottky barrier heights. The discussed Schottky barrier effects will not influence the MC, because it results in the same proportional increase with temperature for the collector current in the parallel as well as the anti-parallel state.
The decrease of MC with temperature in the range from 100 to 260K (see Fig. 4.9) should be related to a certain scattering mechanism. Inelastic electron-electron and elastic impurity and defect scattering are generally known to be temperature independent, so are excluded. Possible thermal scattering mechanisms are phonon scattering (vibrations of the atoms in the lattice) and spin-wave scattering (vibrations of the magnetization of the atoms in the lattice, see page 32).
It is possible to show (from Eq. 4.6 and 4.7), that a decrease of MC with increased scattering strength is only possible when there is spin-mixing. Additional spin-independent scattering will attenuate both the spin-up and spin-down electron channels with the same factor, leaving the MC unaffected. Additional spin-dependent scattering will only further increase the MC (no thermally excited mechanisms are known that have an opposite spin asymmetry in the scattering parameters compared to T=0K). So, the MC can only reduce due to spin-mixing. This mixing of the spin-

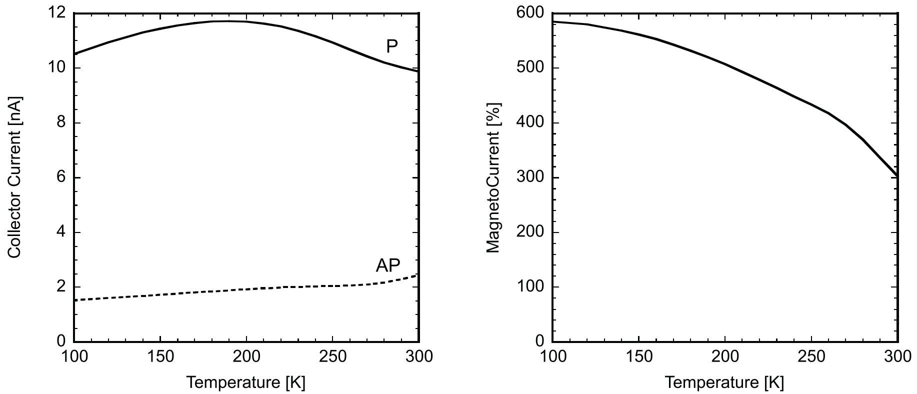

Figure 4.9: *The collector current for the parallel and anti-parallel state (left) and the resulting MC (right) as function of temperature in RSVT8.*

channels is only possible when a hot-electron scatters with a spin-wave (by scattering with a phonon, the spin of the hot-electron is conserved). Therefore, we conclude that the thermal reduction of the MC in the spin-valve transistor is due to spin-wave scattering [93].
It's important to note that the fact that we can measure this spin-wave scattering in the spin-valve transistor, says that hot-electrons that have scattered with a thermal spin-wave still have enough energy to overcome the collector barrier [93]. Furthermore, it is quite well possible that there are also spin-waves scattering events after which the electron can not be collected anymore, this will result in extra attenuation.
The exact temperature dependence of the parallel and anti-parallel collector current can be analyzed much easier in the normalized collector current plot in Fig. 4.10. At low temperatures (T=100∼110K), there is almost no spin-wave scattering. This can also be seen by the saturation of the MC when a spin-valve transistor is cooled down. In this region the increase of collector current is due to the Schottky barrier effects (as in metal base transistors) and is the same for the parallel and anti-parallel state. At higher temperatures (T=120∼210K) only the parallel current appears to decrease due to spin-wave scattering. This is because both the spin-mixing and attenuating part of the spin-wave scattering are reducing the collector current in the parallel state. In the anti-parallel state these work against each other, and so a smaller change is observed. But at high enough temperatures (T=210K∼260K), also the anti-parallel current goes 'down' as result of the spin-wave scattering. The final increase of the collector current (AP) between T=270 to 300K is due to leakage at the collector diode and so the decrease of MC in this region is not related to spin-wave scattering.

4.3.2 Hot-electron scattering in $Ni_{80}Fe_{20}$

In order to analyze the hot-electron scattering in $Ni_{80}Fe_{20}$, we have made a batch of spin-valve transistors, all with a Si(100) emitter and collector and a base consisting

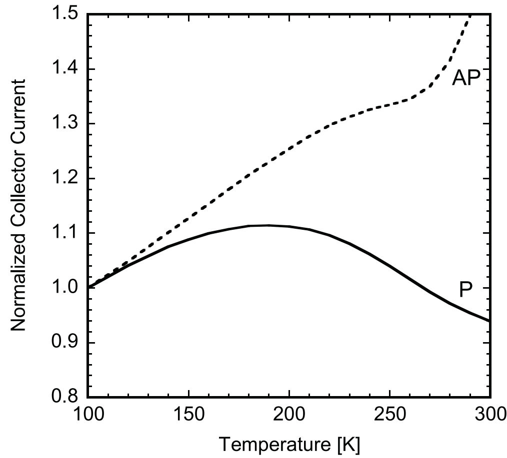

Figure 4.10: *Normalized collector current for the parallel and anti-parallel state. Both curves are normalized to the T=100K values.*

of: Pt 30Å/NiFe xÅ/Au 44Å/Co 30Å/Au 22Å//Au 22Å, with the NiFe thickness (x) ranging from 0 to 100Å. Because all these transistors are made in exactly the same way, as described in chapter 3, all the material properties have been kept reasonably constant, making it possible to make comparisons between the different transistors.
First, we examine the current transport at T=100K. At this temperature we can determine the spin-dependent attenuation lengths for hot-electrons in NiFe. This will be the attenuation lengths without spin-wave scattering (or at least very little). Second, we look at the temperature dependence of the collector current and how this is related to the thermal spin-wave scattering.

4.3.2.1 Spin-dependence of hot-electron scattering in $Ni_{80}Fe_{20}$ at low temperatures

In Fig. 4.11, an overview of the collector current vs. applied magnetic field can be seen of all the different spin-valve transistors at T=100K (except the SVT with 0Å of NiFe). As can be seen, the collector current in the parallel state and anti-parallel state steadily decreases with increasing NiFe layer thickness. Furthermore, the magnetic switching properties change as function of the NiFe layer thickness. At a NiFe thickness of 10Å, the switching field distribution of the soft NiFe layer has become very broad, making it impossible to obtain a full anti-parallel state and so a reduced MC is measured. At thick NiFe layers ($\geq$50Å) the switching is very sharp, and a very well defined anti-parallel state is obtained.
In Fig. 4.12, the collector current vs. NiFe layer thickness is shown. As will be shown, these measurements proof that the collector current is depending both on scattering at the interfaces and in the bulk and that the magnetocurrent is increasing with NiFe layer thickness. It should be remembered that in order to make a spin-valve transistor, many processing steps (cleaning / layer growth / temperature steps etc.) are needed, which

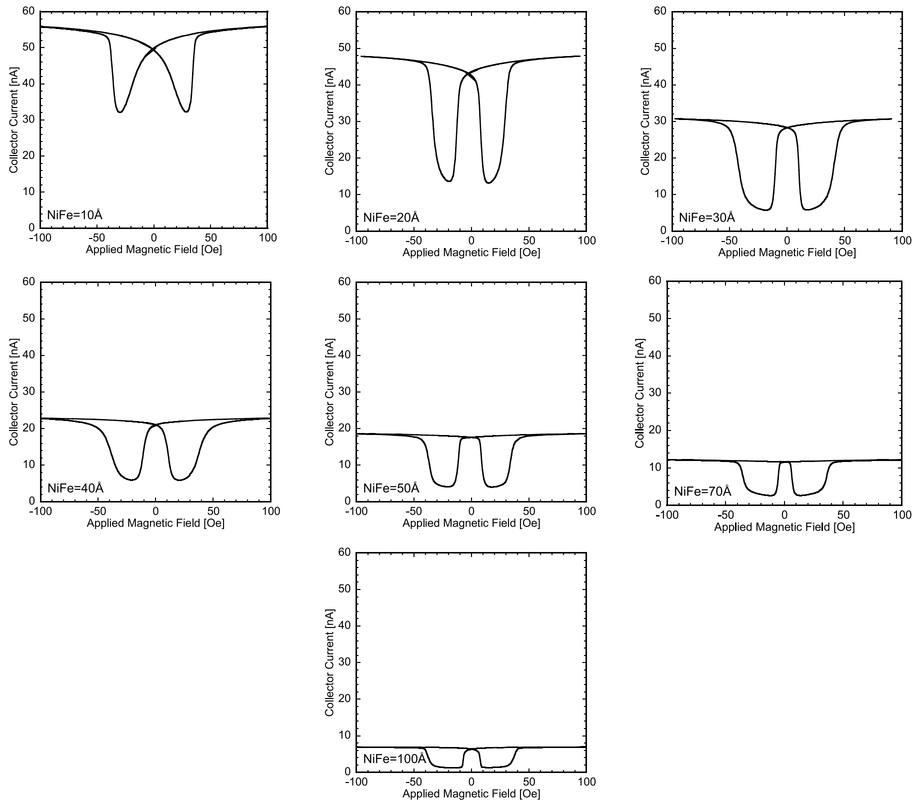

Figure 4.11: *The collector current vs. applied magnetic field for different spin-valve transistors at T=100K. All these transistors have the following structure: Si(100)/Pt 30Å/$Ni_{80}Fe_{20}$ $10 \sim 100$Å/Au 44Å/Co 30Å/Au 22Å//Au 22Å/Si(100) and emitter current of 2mA was injected into the base.*

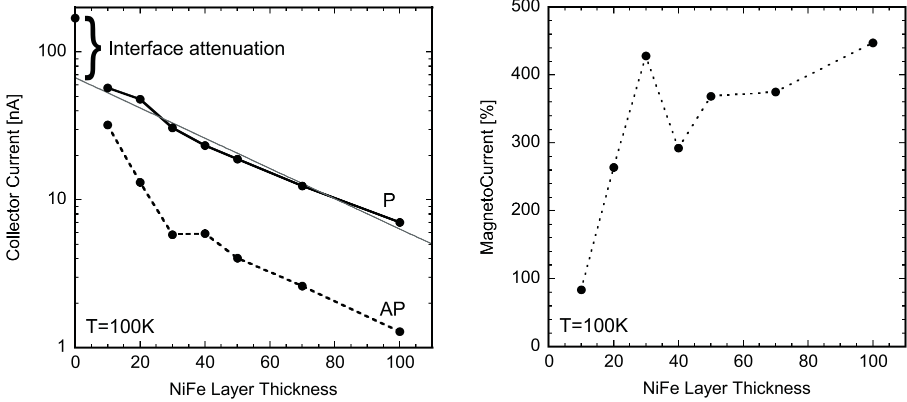

Figure 4.12: *The collector current in the parallel (P) and anti-parallel (AP) state (left) and the magnetocurrent (right) versus the NiFe layer thickness, which has been varied between 0 and 100Å (T=100K and I_e=2mA).*

might result in fluctuations of the sample quality. Therefore, the strange peek at 30Å and dip at 40Å are experimental artifacts, which are mainly due to differences in the magnetic switching properties between these two devices.

The influence of an interface on the current transfer can be seen in Fig. 4.12, from the drop in collector current between the sample (RSVT13) without NiFe (but still Pt/Au/Co/Au//Au) and the samples with this magnetic layer. In the sample without NiFe, a collector current of 169nA is measured at T=100K and I_e=2mA, and from the exponential interpolation from the samples with NiFe to zero thickness, a collector current of 67nA is obtained. This attenuation of ≈ 2.5 is due to the extra interface that is added when the NiFe layer is inserted (to be more precise, a Pt/Au interface is replaced by a Pt/NiFe and a NiFe/Au interface). It should be noted, that although not every interface is the same, there are 7 interfaces (metal-metal as well as metal-semiconductor) in the base and that $(2.5)^7 \approx 600$, so interface scattering might be an important reason why the collector current of the spin-valve transistor is relatively low.

In order to determine the spin-dependent scattering properties of NiFe, we have to fit the collector current measurements, as shown in Fig. 4.12, with theoretical curves based on Eq. 4.6 and 4.7. For this purpose a special Labview program has been developed, so that $\lambda^{\uparrow}$, $\lambda^{\downarrow}$ and $\Gamma^{\downarrow}/\Gamma^{\uparrow}$[6] in both the NiFe and Co layer can be modified and the resulting thickness dependence is recalculated interactively. This makes it very easy to see which parameter influences which part of the NiFe thickness dependence. Furthermore, the program automatically adapts the non-magnetic attenuation (α_{nm}) to result in the best possible fit.

Because we only have a limited amount of data, and many parameters, we start by supposing that the scattering properties in NiFe and Co are similar. The majority attenuation length ($\lambda^{\uparrow}$) for electrons with their spin aligned to the magnetization can be

6 We only use the relative transmission, the absolute part is put in α_{nm}.

extracted from the decrease of parallel collector current with increasing NiFe thickness. An attenuation length of 43 ± 3Å is obtained and appears to be independent of the other fit parameters. The minority attenuation length ($\lambda^{\downarrow}$) is more difficult to obtain, because different almost equally well fits can be made. In Fig. 4.13 we have made an overview of 3 different fits of the same experimental data. In all of these different fits, the attenuation in the Co layer is modelled to pass 5 times more majority electrons than minority electrons (this results in a maximum MC of 400% at high NiFe thickness').
In the top two plots of Fig. 4.13, there is no-interface contribution to the magnetocurrent, so the interface transmission is equal for spin-up and down electrons ($\Gamma^{\uparrow} = \Gamma^{\downarrow}$). In this case, the measurements can be perfectly explained by $\lambda^{\downarrow}_{NiFe}$=8Å.
But on the second row of Fig. 4.13 we have added a small amount of spin-dependent interface scattering ($\Gamma^{\downarrow}/\Gamma^{\uparrow}$=0.8), in which case the bulk contribution to the magnetocurrent can be slightly less, resulting in $\lambda^{\downarrow}_{NiFe}$=10Å.
When there is added even more spin-dependent interface scattering, the experiments can be fitted with $\lambda^{\downarrow}_{NiFe}$=12Å and $\Gamma^{\downarrow}/\Gamma^{\uparrow}$=0.6 as shown in the third row.
As can be seen, all these fits result in the same dependence at high NiFe thickness', but at low thickness there is a remarkable difference. In the 3 cases, the model predicts an MC of 95, 118 and 161%, respectively, for a NiFe thickness of 10Å. In the comparison with experiment, we should be very prudent, because the switching distribution of the 10Å NiFe layer in RSVTN12 is very broad, resulting in a partial anti-parallel state with a MC value of 78%. In contradiction to other transistors, the highest MC of RSVTN12 is measured around T=200K, because the increase of temperature makes it easier to switch the NiFe layer and this results in a better anti-parallel state with a higher MC. The best guess we can make is to take this highest value (97%) and correct it with the observed decrease in MC (due to spin-wave scattering) of the 20Å NiFe device (10% in RSVTN4) when it is heated up from 100 to 200K. This procedure results in a corrected MC of ≈110%, so that our measurements are between the first (95%) and second case (118%). Based on the precision of the measurement data and the sensitivity of the parameters on the fit, we conclude that the hot-electron scattering parameters at ≈ 0.9eV in NiFe are given by:

$\lambda^{\uparrow}_{NiFe}$	$\lambda^{\downarrow}_{NiFe}$	$\Gamma^{\downarrow}_{NiFe}/\Gamma^{\uparrow}_{NiFe}$
43 ± 3 Å	10 ± 2 Å	0.8 ± 0.2

In this practical situation this means that most of the magnetocurrent is coming from the spin-dependence in the bulk, and an MC of 100% might come from the interfaces alone.
In order to determine the minority attenuation length and the interface contributions with more precision, it is essential to use spin valves with magnetic layers that have more coercivity difference, so that over the whole range of NiFe thickness' a perfect anti-parallel state can be obtained. This means that the coercivity of the Co layer should be increased, which can be achieved by replacing Co with a different hard magnetic material, like CoFe, CoPt, CoCr etc.

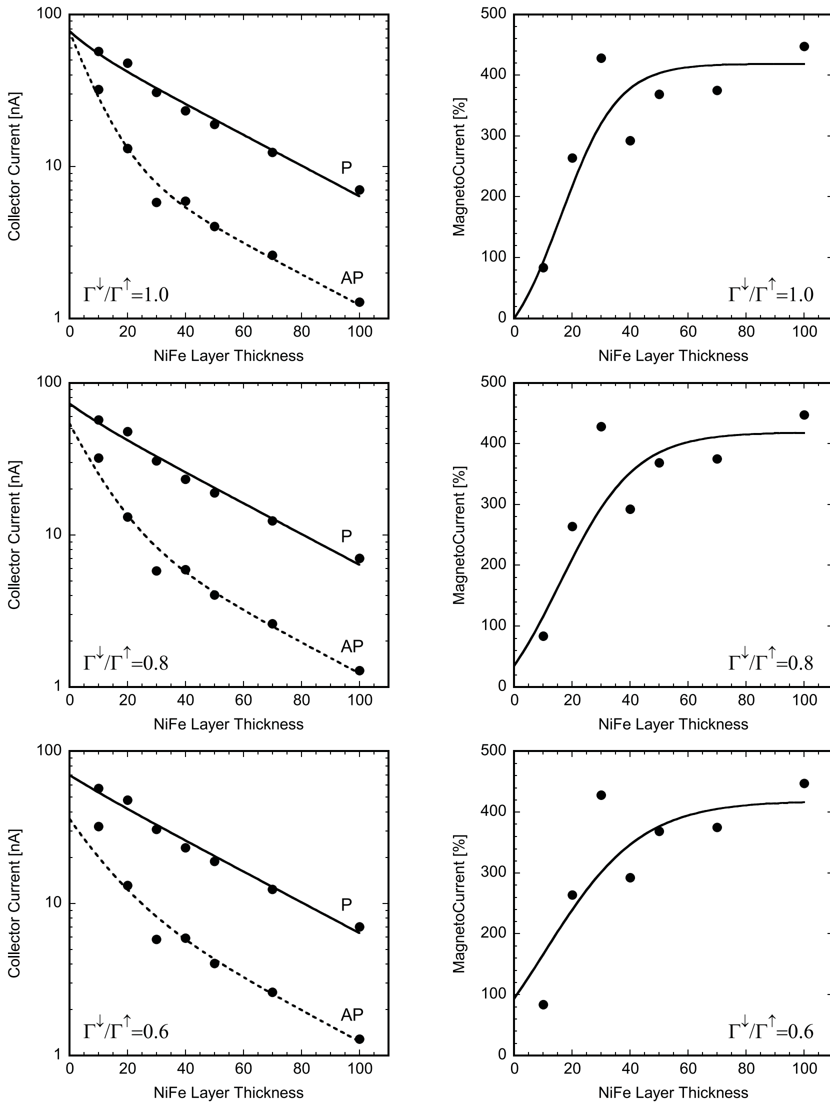

Figure 4.13: *The 3 different fits of the collector current and MC versus NiFe layer thickness as discussed in the text.* $\Gamma^{\downarrow}/\Gamma^{\uparrow}$ *has been set to 1, 0.8 and 0.6 and the bulk attenuation lengths has been adapted to result in the best fit. The experimental data points are measured at T=100K for an emitter current of 2mA.*

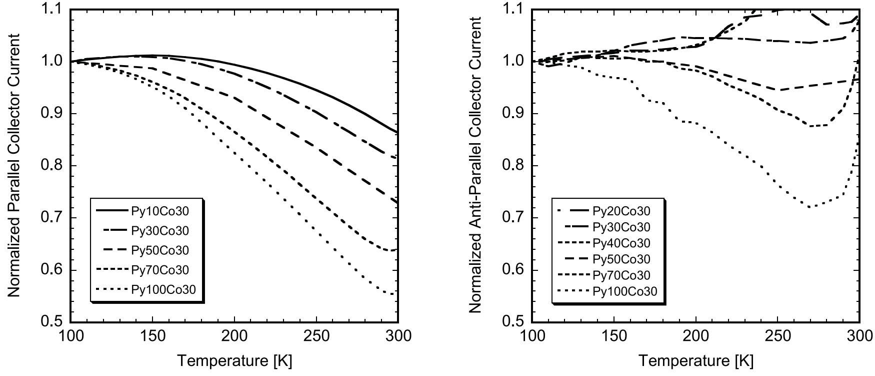

Figure 4.14: *The normalized collector current for the parallel (left) and anti-parallel (right) state versus temperature in spin-valve transistors with 10, 30, 50, 70 and 100Å of NiFe(≈Py) and 30Å of Co.*

4.3.2.2 Thermal hot-electron scattering in $Ni_{80}Fe_{20}$

Now the scattering parameters at T=100K are extracted, we can analyze the temperature dependence of the current transfer in the different transistors. Similar as done for the metal base transistors, we normalize the collector current to the value at T=100K, as shown in Fig. 4.14, and analyze how the NiFe layer thickness influences the temperature dependence. For the normalized collector current in the parallel state, a clear increase in temperature dependence with increase in NiFe thickness can be seen. This means that there is temperature dependent scattering in the bulk. For the normalized collector current in the anti-parallel state, only devices with $t_{NiFe} \geq$ 50Å show the bulk related temperature dependence, because only these devices have reasonable magnetic switching properties. The apparent noise in these measurements is due to the discrete steps (of 0.6 Oe in the magnetic field and 10K in temperature) at which these measurements are done, and at every measurement, a slightly different *partial* anti-parallel state is obtained. In the parallel state this problem doesn't exist, because the parallel state can always be obtained by applying a high enough magnetic field.
As shown in the previous section (page 72), the temperature dependence of the MC is due to spin-wave scattering, therefore we attribute the attenuation of the collector current also due to spin-waves[7].
Coming back to the temperature dependence of the normalized collector current in the parallel state, one can determine the bulk spin-wave attenuation length from these measurements by making comparisons between the different devices. Based on the base transmission formula (Eq. 4.6 [8]) we can write for majority electrons (minor-

7 Although spin-wave scattering contributes to the temperature dependence, thermal phonon scattering reducing the collection probability can not be excluded. Therefore, this is one of the effects contributing to β as described in the modeling section of this chapter.

8 This formula can only be used when there is a negligible influence from the spin-wave (flip) scattering of the spin-down electrons into the spin-up channel (in-scattering is ignored by Eq. 4.6).

ity electrons hardly contribute to the parallel state) the temperature dependent base transmission as:

$$\alpha_b^P(T) = \alpha_{nm}(T)\frac{\left(\Gamma_{NiFe}^{\uparrow}(T)\Gamma_{Co}^{\uparrow}(T)\right)^2\left[e^{-t_{NiFe}/\lambda_{NiFe}^{\uparrow T=0}}e^{-t_{NiFe}/\lambda_{NiFe}^{SW}(T)}\right]\left[e^{-t_{Co}/\lambda_{Co}^{\uparrow T=0}}e^{-t_{Co}/\lambda_{Co}^{SW}(T)}\right]}{2} \tag{4.9}$$

In which we have, based on Matthiesen's law, written the attenuation length in the bulk in a part which is temperature independent (the T=0K value) and a thermal part due to spin-wave scattering: $1/\lambda_{NiFe}^{\uparrow} = 1/\lambda_{NiFe}^{\uparrow T=0} + 1/\lambda_{NiFe}^{SW}(T)$. If we now calculate the base transmission normalized to T=100K, one can write:

$$\alpha_b^{PN}(T) = \frac{\alpha_{nm}(T)\left(\Gamma_{NiFe}^{\uparrow}(T)\Gamma_{Co}^{\uparrow}(T)\right)^2}{\alpha_{nm}(100)\left(\Gamma_{NiFe}^{\uparrow}(100)\Gamma_{Co}^{\uparrow}(100)\right)^2}\frac{\left[e^{-t_{NiFe}/\lambda_{NiFe}^{SW}(T)}\right]}{\left[e^{-t_{NiFe}/\lambda_{NiFe}^{SW}(100)}\right]}\frac{\left[e^{-t_{Co}/\lambda_{Co}^{SW}(T)}\right]}{\left[e^{-t_{Co}/\lambda_{Co}^{SW}(100)}\right]} \tag{4.10}$$

If we now compare two devices with a different NiFe layer thickness ($t1$ and $t2$), but the same interfaces and Co layer thickness, we can express the ratio ($R(T)$) as:

$$R(T) = \frac{\alpha_b^{PN}(T)|_{t_{NiFe}=t1}}{\alpha_b^{PN}(T)|_{t_{NiFe}=t2}} = \frac{\left[e^{-(t1-t2)/\lambda_{NiFe}^{SW}(T)}\right]}{\left[e^{-(t1-t2)/\lambda_{NiFe}^{SW}(100)}\right]} = e^{-(t1-t2)\left[\frac{1}{\lambda_{NiFe}^{SW}(T)}-\frac{1}{\lambda_{NiFe}^{SW}(100)}\right]} \tag{4.11}$$

Finally, in order to determine the spin-wave scattering length (λ_{NiFe}^{SW}) as function of temperature, we can plot $-ln(R(T))/(t1-t2)$ as shown in Fig. 4.15, which in formula form is given by:

$$-\frac{\ln[R(T)]}{(t1-t2)} = \left[\frac{1}{\lambda_{NiFe}^{SW}(T)} - \frac{1}{\lambda_{NiFe}^{SW}(100)}\right] \tag{4.12}$$

So this is the extra amount of spin-wave scattering compared to T=100K. By assuming that the spin-wave scattering length can be described by a power law: $\lambda_{NiFe}^{SW}(T) = \frac{a_0}{T^m}$, we can obtain a_0 and m from the fit of the experimental curve with $(T^m - 100^m)/a_0$ and with these parameters we can determine the spin-wave attenuation length for spin-up electrons in NiFe. In Fig. 4.15, the ratio is determined between a device with t_{NiFe}=100Å and t_{NiFe}=30Å, other combinations give similar results, like NiFe100/NiFe20 and NiFe70/NiFe10. The temperature dependence of spin-wave scattering is near quadratic (m=2.25) and the experimental curve can also be reasonably fitted with $\lambda^{SW} = a_0/T^2$ (with $a_0 = 1.28 \cdot 10^7$). This finally results in a λ^{SW} of $\approx$ 140 Å at 300K, which is relatively strong compared to the T=0K majority-spin attenuation length of 43Å in NiFe.
It should be noted that the above method makes hugh errors at low temperatures (T<150K), because when there is little effect of spin-wave scattering on the collector current it will be hard to extract λ^{SW} from these measurements. At higher temperatures the error is much smaller, because the spin-wave scattering has a profound effect on the measurements, and so λ^{SW} can be determined with more precision. Furthermore, there can be deviations due to differences in the temperature dependence of the

Based on the short attenuation length for spin-down electrons this assumption can be made.

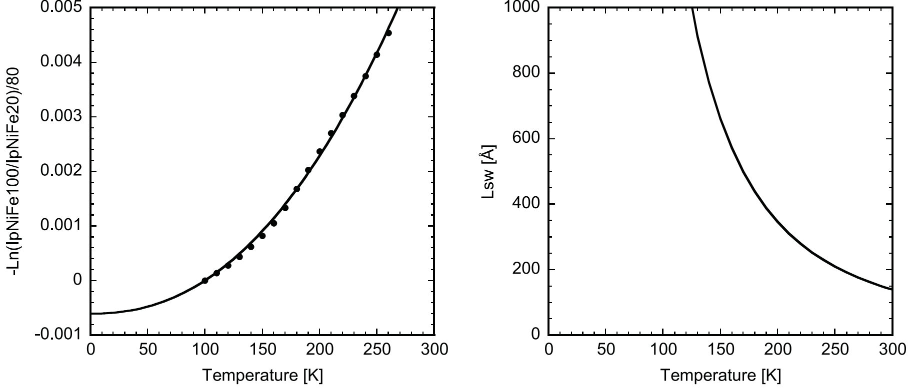

Figure 4.15: *The fit of the spin-wave scattering in NiFe (left) from which we extract $\lambda^{SW}_{NiFe}(T) = 5.3 \cdot 10^7/T^{2.25}$. On the right we show the spin-wave attenuation length based on this formula.*

other α's, especially $\alpha_e^{hot}(T)$ can be different between two devices due to differences in Schottky barrier quality.
With this method we have determined the thermal spin-wave attenuation length for spin-up electrons. The attenuation length for spin-down electrons can directly be obtained, because in theory [94] it is shown that $\tau^{\downarrow}_{SW} = \tau^{\uparrow}_{SW}$, so in principle we can write $\lambda^{\downarrow}_{SW} = (v^{\downarrow}/v^{\uparrow}) \times \lambda^{\uparrow}_{SW}$, in which $v^{\uparrow(\downarrow)}$ denotes the velocity of the respective hot spin-up (down) electrons.
Furthermore, in order to explain the reduction of the MC with temperature, we have to incorporate the mixing of the spin-channels by spin-wave scattering. This can not be done by Eq. 4.6, therefore a new model that includes spin-mixing is proposed in the modeling section of this chapter.

4.3.3 Hot-electron scattering in Co

Similar to the series with changing NiFe layer thickness, we have made several spin-valve transistors with different Co layer thickness' to characterize the scattering properties of Co. In Fig. 4.16, one can see the collector current vs. magnetic field for 4 devices with a Co thickness between 20 and 50Å, all with a NiFe layer thickness of 30Å. As can be seen in Fig. 4.16, the 20 and 30Å Co devices have good switching properties, resulting in a well defined anti-parallel state. But when the Co thickness is increased to 40 and 50Å, the switching of the NiFe layer becomes harder, probably due to a ferromagnetic coupling with the Co, resulting in a somewhat non-ideal anti-parallel alignment. Due to this switching properties, we are limited in the range over which we can change the Co layer thickness, making it hard to determine the scattering parameters in Co with the same precision as could be done for NiFe. Making the Co layer even thinner than 20Å has also been tried, but a 10Å Co layer shows super-paramagnetic behavior. This is probably due to cluster formation during the growth

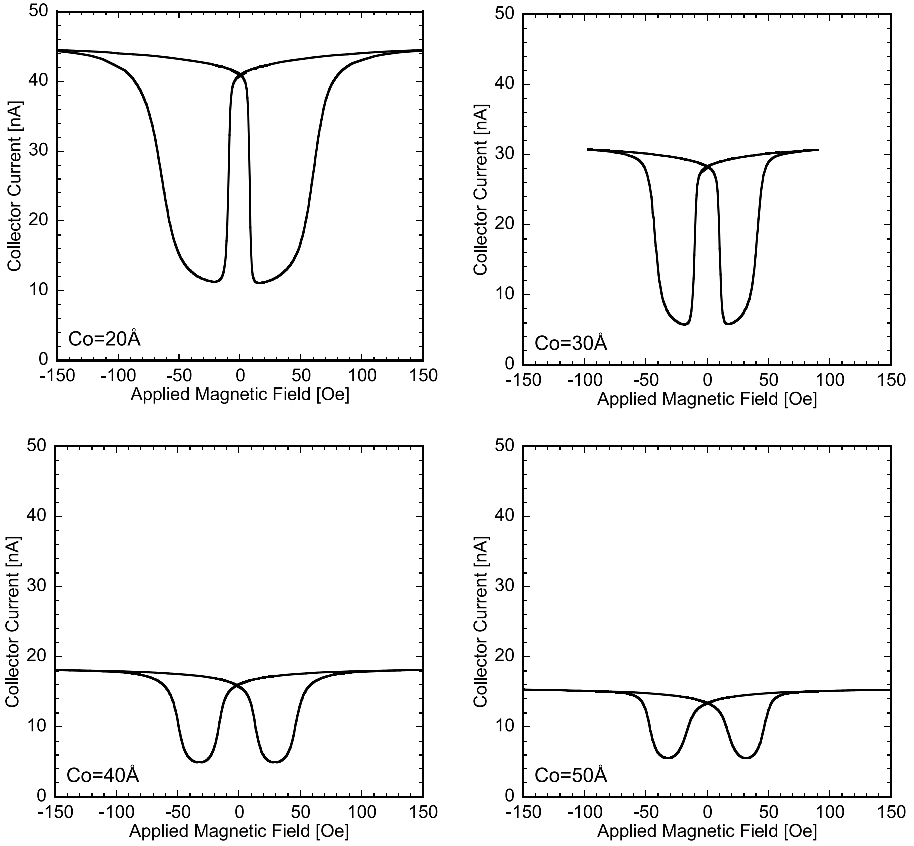

Figure 4.16: *The collector current vs. applied magnetic field for different spin-valve transistors with the following structure: Si(100)/Pt 30Å/$Ni_{80}Fe_{20}$ 30Å/Au 44Å/Co 20∼50Å/Au 22Å//Au 22Å/Si(100). An emitter current of 2mA was injected into the base at T=100K.*

on the much rougher 'buffer' (Pt/NiFe/Au) compared to a NiFe layer with the same thickness (only Pt as buffer).
In Fig. 4.17 the collector current and the magnetocurrent versus Co layer thickness are shown, from the exponential attenuation of the collector current in the parallel state, we can extract the majority spin attenuation length of: $\lambda^{\uparrow}_{Co} \approx 25 \pm 6$Å. This is in nice agreement with the value reported by Rippard and Buhrman [79], who have measured a majority attenuation length of 23Å and a minority of 8Å in BEEM experiments with hot-electrons at 1eV in Co. From our experiments it is impossible to extract also the minority spin attenuation length based on the behavior of the collector current and magnetocurrent at very low thickness as done for NiFe, as explained above. It is only possible to deduce from the maximum MC in the NiFe series, that is should at least be ≈ 5 times easier for majority electrons than minority electrons to pass the Co layer.
Like in NiFe, there is thermal spin-wave scattering in Co, as can be seen from the temperature dependence of the collector current in the parallel and anti-parallel state (Fig.

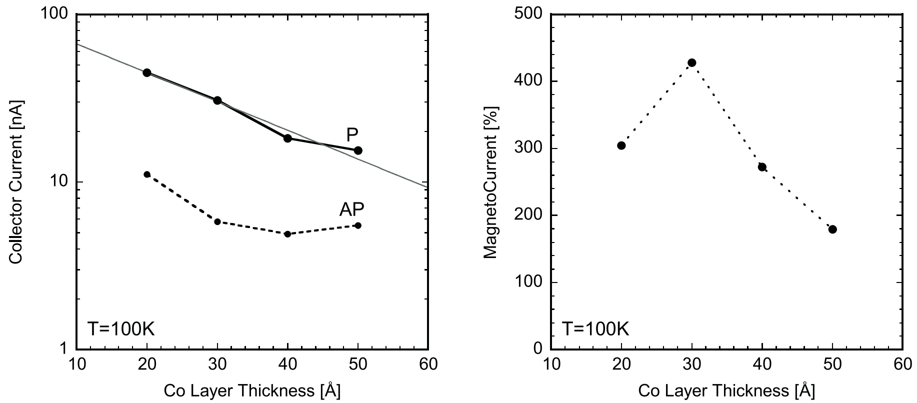

Figure 4.17: *The collector current (left) in the parallel (P) and anti-parallel (AP) state and the magnetocurrent (right) versus the Co layer thickness in a Si(100)/Pt 30Å/NiFe 30Å/Au 44 Å/Co xÅ/Au 22Å//Au 22Å/Si(100) transistor (T=100K and I_e=2mA).*

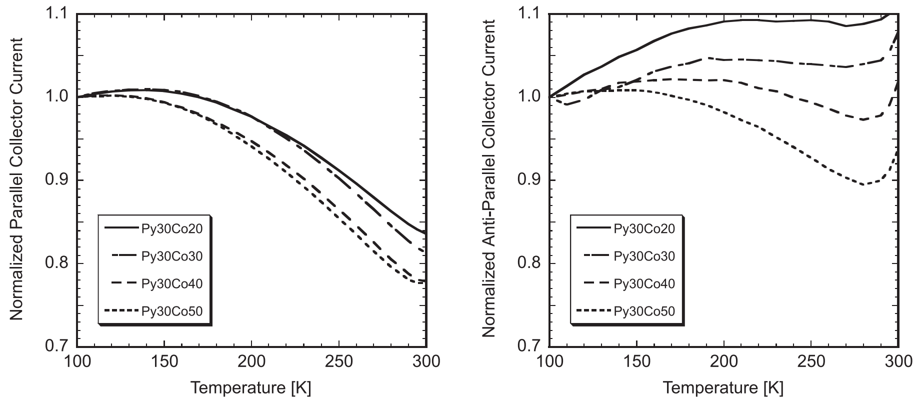

Figure 4.18: *The normalized collector current in the parallel (left) and anti-parallel (right) state versus temperature in spin-valve transistors with 20, 30, 40 and 50Å of Co and 30Å of NiFe.*

4.18). When the temperature dependence for these devices is compared with those in the NiFe series, we see that an increase of 20Å in the NiFe thickness results in more temperature dependence than an increase of 20Å in the Co thickness. This shows that there is less spin-wave scattering in Co compared to NiFe, which can be confirmed quantitatively, by extracting the spin-wave attenuation length for majority-spin electrons in Co by comparing the thermal attenuation in a device with 50Å and 20Å of Co, as shown in Fig. 4.19. A thermal spin-wave attenuation length of λ_{Co}^{SW} ≈270Å is obtained at T=300K. This spin-wave attenuation length is longer in Co than in NiFe, because Co has a higher Curie temperature (T_c^{Co}=1388K and T_c^{NiFe}=873K). As shown in the theory chapter (page 34), the number of spin-waves is directly related to the relative temperature ($\propto (T/T_c)^{3/2}$), as does the relative decrease in magnetization ($\Delta M/M(0)$) due to these spin-waves.

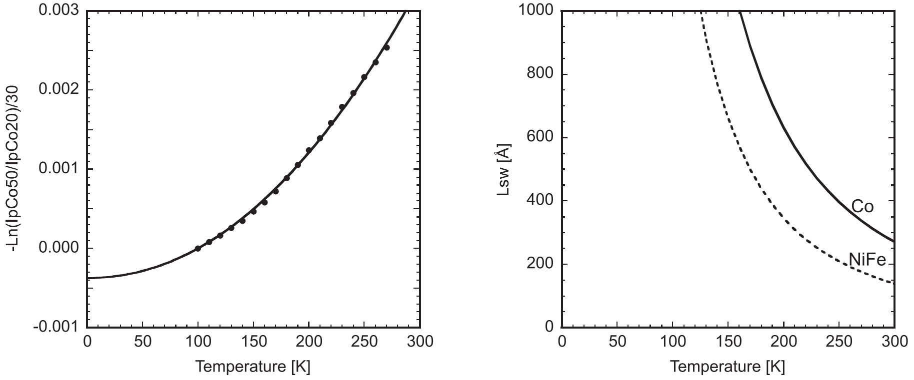

Figure 4.19: *The fit of the spin-wave scattering in Co (left) from which we extract $\lambda^{SW} = 4.0 \cdot 10^7/T^{2.09}$ (or $a_0 = 2.5 \cdot 10^7$ with m=2). On the right we show the spin-wave attenuation length based on this formula in solid, the dashed line denotes the spin-wave attenuation length for NiFe.*

4.4 Modeling the experimental results

After these two series of spin-valve transistors with different magnetic layer thickness', we have shown that there is spin-dependent transport. Furthermore, in the magnetic layers there is thermal spin-wave scattering, resulting not only in an extra thermal attenuation, but also in the mixing of the spin-up and down electrons. In order to properly take this mixing into account, one has to solve the Boltzmann equation for both spin-up and spin-down electrons simultaneously, as explained in the Appendix A.2.3 (page 114). In this model, we introduce the β parameter, which models the amount of electrons that scatter on a spin-wave and contribute to the other spin-channel, divided by the total amount of electrons that scatter on a spin-wave (so β=spin-mix/total spin-wave, and $(1-\beta)$ is the attenuating fraction due to spin-waves). Physically is β related to the fact that spin-waves will change both energy and momentum (and spin of course) of the hot-electron. After a small (E,k)-transfer, the hot electron can still be collected, and so this electrons adds to the spin-mixing part, but when there is a large (E,k)-transfer, the hot-electron can not be collected anymore, and so adds to the attenuating part. Also other temperature dependent attenuation mechanisms, like thermal phonon scattering might slightly change the value of β.
Here we will show an example of how well our measurements agree with this model. In Fig. 4.20, we show the calculated collector current (normalized at T=100K) vs. temperature for devices with different NiFe layer thickness'.

As can be seen, there is more temperature dependence in the parallel state as in the anti-parallel state, and so the magnetocurrent will reduce with temperature. In Fig. 4.21, we have plotted the resulting temperature dependence of the magnetocurrent.

In these calculations we have used β=0.4, what means that from the thermal spin-wave scattering events, only 40% will contribute to the other spin-channel, the other 60% will be lost. From Fig. 4.21, one can see that beta is directly related to the decrease in MC, as it determines the fraction of thermally scattered electrons that spin-mix. When

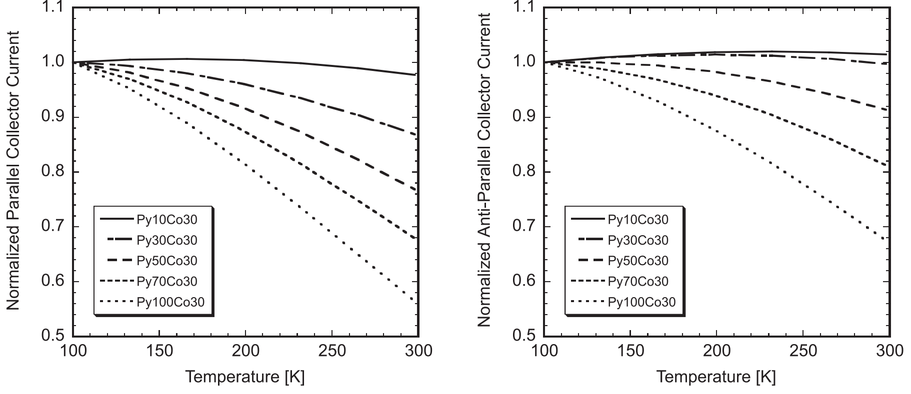

Figure 4.20: *The normalized collector current in the parallel (left) and anti-parallel (right) state as function of temperature, **calculated** with spin-dependence in the bulk ($\lambda^{\uparrow}_{NiFe}$=43Å, $\lambda^{\downarrow}_{NiFe}$=8Å, $\lambda^{\uparrow}_{Co}$=25Å, $\lambda^{\downarrow}_{Co}$=10.5Å) and spin-wave scattering ($\lambda_{sw} = a_0/T^2$) in the NiFe ($\lambda^{\uparrow-SW}_{NiFe} = \lambda^{\downarrow-SW}_{NiFe}$=140Å at T=300K) and in the Co ($\lambda^{\uparrow-SW}_{Co} = \lambda^{\downarrow-SW}_{Co}$=270Å at T=300K) and with β=0.4 and t_{Co}=30Å. Furthermore, a linear increase of 10% in collector current due to the Schottky barriers is included.*

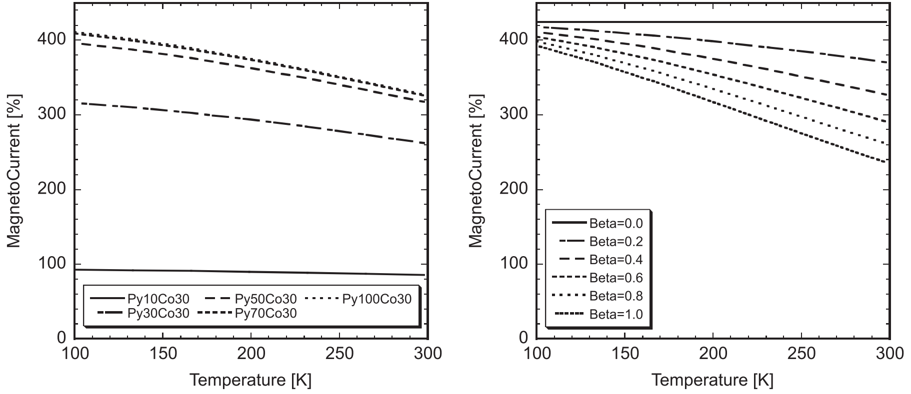

Figure 4.21: *On the left, the reduction in magnetocurrent for different NiFe thickness' as function of temperature as modelled with the same parameters as mentioned in Fig. 4.20. And on the right, the same simulation for different β values (t_{NiFe}=100Å).*

β=0 (no spin-mixing), the model as used before is obtained (Eq. 4.6 and Eq. 4.7), all thermal scattering events will remove the electron from the collector current, and the MC will remain constant. When β=1, all thermally scattered electrons will mix with the other spin-channel, and a maximum decrease in MC is obtained.

4.5 Conclusions

Although the I-V characteristics of our Si/Pt and Si/Au Schottky diodes are close to ideal, as described by the thermionic emission theory, the emission and collection properties by these Schottky diodes are different than expected. The current transfer in metal base transistors increases with temperature, as would not be expected based on thermal scattering in the base. The slope of the current transfer vs. temperature between different transistors appears to be directly related to the difference in Schottky barrier height between the emitter and collector. The main reasons behind this is the energy dependence of the acceptance cone, a higher hot-electron energy will result in a larger critical angle. Because the average hot-electron energy increases slightly with temperature (thermal broadening), this results in an increase of collector current. Furthermore, the energy of the hot-electrons can change even more when the Schottky barriers are not uniform but distributed, making the increase of collector current with temperature even stronger.

Spin-valve transistors, as made in this thesis, can operate at room temperature, and typically show a hugh magnetocurrent of 300% within a small magnetic field of several Oe's. This magnetocurrent can be so high due to the spin-dependent *exponential* attenuation in the two magnetic layers of the spin-valve. In the NiFe layer we have shown for majority-spin electrons that the exponential attenuation is 43Å and for minority-spin electrons about 8Å and in Co only the majority-spin attenuation length could be extracted ($\lambda_{Co}^{\uparrow}$=25Å). Although the experiments can be explained with spin-dependent scattering in the bulk, it can not be excluded that there is also spin-dependent interface scattering.

There are two effects that govern the temperature dependence of the spin-valve transistor, similar to the metal base transistor, there is the increase of collector current with temperature due to the emission and collection properties of the Schottky barriers. But more important, there is thermal spin-wave scattering in the magnetic layers, this scattering mechanism mixes the spin-up and spin-down electrons, resulting in a reduction of the magnetocurrent. By comparing devices with different magnetic layer thickness', the thermal attenuation lengths due to spin-wave scattering in NiFe and Co have been extracted ($\approx$ 140Å and $\approx$ 270Å, respectively, at T=300K). The spin-wave attenuation length in NiFe is shorter than in Co, because there are more spin-waves (number of spin-waves is directly related to the relative temperature, $\equiv T/T_c$) in NiFe than in Co at room temperature. Although hot-electron scattering with thermal spin-waves will flip the spin of the hot-electrons, also their energy and momentum will change. From the modelling in the last section, it is shown that the reduction of the magnetocurrent, agrees with the case that about 40% of the spin-wave scattered electrons contribute to the other spin-channel, and the other 60% are attenuated.

Chapter 5

Conclusion and Recommendations

5.1 Conclusions

The motion of electrons cannot only be controlled by its charge, but also by its spin. Research on this topic is done in the field of spin-electronics, in which the spin-valve transistor is one of the most promising devices. The spin-valve transistor is a 3-terminal device with, as used in this thesis, a Si emitter, a metallic Pt/NiFe/Au/Co/Au//Au base and Si collector. In these devices a huge relative change in collector current of typically 300% (=magnetocurrent) is obtained at room temperature, when the relative orientations of the two magnetic layers change. Because these magnetic layers switch within several Oe's, the spin-valve transistor is very suitable as magnetic field sensor.
The Si emitter serves to inject hot-electrons above the Fermi-level into the base, these electrons have a very narrow momentum distribution (only 5-10° from the normal, the so-called emission cone) and the energy is thermally distributed above the Schottky barrier, as explained in the theory chapter. Similar, the Si collector only accepts electrons with enough energy and with their momentum within the acceptance cone. Therefore, changes in either energy or momentum will influence the collector current. In the base, the hot-electrons can scatter inelastically, due to electron-electron interactions with electrons from below the Fermi-level, in which a large part of their excess energy is lost. The hot-electrons can also scatter elastically due to interactions with impurities, defects or phonons, and this results in a change of the hot-electron's momentum. In the description of the current transport in the base, the Boltzmann equation is used to describe the number of hot-electrons with the right momentum to contribute to the collector current. Solving this equation for elastic and inelastic scattering in a field free region (no electrical field), results in *exponential* attenuation. In the magnetic layers this exponential attenuation is *spin-dependent*, and therefore such a large magnetocurrent is observed. Elastic scattering, as found in the bulk, but especially at the interfaces, is most probably the reason of the low observed collector current.
The spin-valve transistor is made by depositing a Pt/NiFe/Au/Co spin valve by MBE on the Si emitter, after which on both the emitter and collector wafer, a Au layer is deposited that is used to bond the wafers together by in-vacuum metal bonding.
The Si/Pt ($q\Phi_e \approx$ 0.9eV) and Si/Au ($q\Phi_c \approx$ 0.8eV) Schottky diodes in these spin-valve transistors, show close to ideal I-V characteristics as described by the thermionic-emission theory. The emission and collection of hot-electrons by these Schottky diodes are investigated in metal base transistors (Si/Pt/Au/Si structures) by measuring the temperature dependence of the collector current. The collector current is a linearly increasing function of temperature, what can be explained by the increase of the acceptance cone angle with hot-electron energy, which increases with temperature. Furthermore, non-uniform Schottky barriers can also contribute to the observed temperature dependence of the collector current.
In the base, the exponential attenuation in the bulk has been experimentally confirmed. Scattering at the interfaces also reduce the collector current. In NiFe, we have extracted an attenuation length of 43Å for majority-spin electrons and 8Å for minority-spin electrons. In Co, we were only capable of extracting a majority-spin attenuation length of 25Å. Although the experiments can be explained with only spin-dependent scattering in the bulk, it can not be excluded that there is also spin-dependent interface

transmission.
Moreover, including magnetic materials in the base, results in more temperature dependence of the collector current. This appears to be related to thermal spin-wave scattering in the bulk of the magnetic layers. By comparing devices with different magnetic layer thickness', the thermal attenuation lengths due to spin-wave scattering in NiFe and Co have been extracted (140Å and 270Å, respectively, at T=300K). The spin-wave attenuation length in NiFe is shorter than in Co, because there are more spin-waves in NiFe than in Co at room temperature (the number of spin-waves is directly related to the relative temperature, $\equiv T/T_c$). At last, a model of the spin-valve transistor is presented that includes the effects of spin-wave scattering on the collector current, and shows that the experimental reduction in magnetocurrent agrees with the case that about 40% of the spin-wave scattered electrons contribute to the other spin-channel.

5.2 Recommendations and Discussion

In order to improve the current transfer of the spin-valve transistor, many changes can be made to the emitter, base and collector. In this section we will discuss these possibilities and make some general remarks regarding the spin-valve transistor.

At the emitter, one can increase the hot-electron energy. This will result in a larger acceptance cone at the collector and so more collector current. In order to give the electrons more energy, a different semiconductor, like SiC, can be used at the emitter (for example, SiC/Pd or SiC/Au Schottky diode have a barrier height of $q\Phi_b$=1.6, 1.2eV, respectively [95]). The disadvantage is that SiC wafers are extremely expensive, and the chemical cleaning and etching of these wafers might not be feasible. Another possibility is the use of an Al_2O_3 tunnel junction to inject electrons above the collector barrier ($V_{bias} \geq q\Phi_b$)[33]. Although this requires investments in a new plasma source, this seems the more viable option because plasma-oxidation has become common practice in many laboratories and the whole spin-valve transistor stack can be grown in one run without bonding. With this procedure we can use 3" inch wafers, resulting in better lithography and processing options than the current 1x1cm^2 samples.

In the base, only noble metals (i.e. Au, Ag, Cu) should be used instead of transition metals (like Pt or Pd) because the hot-electrons can only scatter with other s-electrons, and the more abundant d-electrons can not be excited by hot-electrons of ≈1eV. This might of course only work for the non-magnetic materials, because the ferromagnetic materials (Fe, Co, Ni and their alloys) rely on the 3d-bands for their magnetism. Therefore, it will be important to optimize (epitaxial growth, chemical composition and bandstructure) these materials to obtain the longest possible attenuation lengths. Also the structure (chemical/physical/electrical) of the interfaces should be studied in more detail, in order to find ways to decrease the interface scattering, because this seems to be one of the main reasons of the low current transfer (see for example [96], which shows the difference in transmission between two different stacking types of

Co on Cu).

At the collector (as well at the emitter), it is important that there is an abrupt interface with low scattering in the semiconductor, and when used as substrate it should promote a good growth of the metal layers. When the device needs to operate at higher temperatures, it is important that the collector barrier is as high and its surface as small as possible to decrease the leakage current of the collector diode, which rises enormously fast ($\approx$ 3 orders of magnitude with 50°C).

Bibliography

[1] G. A. Prinz. “Spin-polarized transport”. *Physics Today* **48**, 58 (1995).

[2] D.J. Monsma, J.C. Lodder, Th.J.A. Popma and B. Dieny. “Perpendicular hot electron spin-valve effect in a new magnetic field sensor:the spin-valve transistor”. *Phys. Rev. Lett.* **74**, 5260 (1995).

[3] R. Landauer and J.J. Hall. “Solid state physics as a source of modern electronics”. *Science* **160**, 736 (1968).

[4] R. Landauer. “The future evolution of the computer”. *Physics today* **23**, 22 (1970).

[5] M.N. Baibich, J.M. Broto, A. Fert, F. Nguyen van Dau, F. Petroff, P. Eitenne, G. Creuzet, A. Friederich and J. Chazelas. “Giant magnetoresistance of (001)Fe/(001)Cr magnetic superlattices”. *Phys. Rev. Lett.* **61**, 2472 (1988).

[6] G. Binasch, P. Grunberg, F. Saurenbach and W. Zinn. “Enhanced magnetoresistance in layered magnetic structures with antiferromagnetic interlayer exchange”. *Phys. Rev. B* **39**, 4828 (1989).

[7] R.J. Soulen et. al. “Measureing the spin polarization of a metal with a superconducting point contact”. *Science* **282**, 85 (1998).

[8] I.I. Mazin. “How to define and calculate the degree of spin polarization in ferromagnets”. *Phys. Rev. Lett.* **83**, 1427 (1999).

[9] S.P. Lewis, P.B. Allen and T. Sasaki. “Band structure and transport properties of CrO_2”. *Phys. Rev. B* **55**, 10253 (1997).

[10] R. A. de Groot, F. M. Mueller, P. G. van Engen and K. H. J. Buschow. “New class of materials: half-metallic ferromagnets”. *Phys. Rev. Lett.* **50**, 2024 (1983).

[11] K.I. Kobayashi, T. Kimura, H. Sawada, K. Terakura and Y. Tokura. “Room-temperature magnetoresistance in an oxide material with an ordered double-perovskite structure”. *Nature* **395**, 677 (1998).

[12] A.P. Ramirez and M.A. Subramanian. “Large enhancement of magnetoresistance in $Tl_2Mn_2O_7$: pyroclore versus perovskite”. *Science* **277**, 546 (1997).

[13] H. Ohno, F. Matsukura, T. Omiya and N. Akiba. “Spin-dependent tunneling and properties of ferromagnetic (Ga,Mn)As (invited)”. *J. Appl. Phys.* **85**, 4277 (1999).

[14] J. Konig, H.H. Lin and A.H. MacDonald. “Theory of diluted magnetic semiconductor ferromagnetism”. *Phys. Rev. Lett.* **84**, 5628 (2000).

[15] H. Akai. “Ferromagnetism and its stability in the diluted magnetic semiconductor (In, Mn)As”. *Phys. Rev. Lett.* **81**, 3002 (1998).

[16] N. Akiba, D. Chiba, K. Nakata, F. Matsukura, Y. Ohno and H. Ohno. “Spin-dependent scattering in semiconducting ferromagnetic (Ga,Mn) As trilayer structures”. *J. Appl. Phys.* **87**, 6436 (2000).

[17] T. Hayashi, H. Shimada, H. Shimizu and M. Tanaka. “Tunneling spectroscopy and tunneling magnetoresistance in (GaMn)As ultrathin heterostructures”. *J. Cryst. Grow.* **201/202**, 689 (1999).

[18] S. Gasiorowicz. “Quantum Physics”. John Wiley & Sons, inc. (1974).

[19] W.F. Egelhoff, Jr. P.J. Chen, C.J. Powell, M.D.Stiles, R.D. McMichael, J.H. Judy, K. Takano and A. E. Berkowitz. “Oxygen as a surfactant in the growth of giant magnetoresistance spin valves”. *J. Appl. Phys.* **82**, 6124 (1997).

[20] W.P. Pratt, S.F. Lee, J.M. Slaughter, R. Loloee, P.A. Schroeder and J. Bass. “Perpendicular giant magnetoresistance of Ag/Co multilayers”. *Phys. Rev. Lett.* **66**, 3060 (1991).

[21] M.A.M. Gijs and G.E.W. Bauer. “Perpendicular giant magnetoresistance of magnetic multilayers”. *Advan. Phys.* **46**, 285 (1997).

[22] M.A.M. Gijs, S.K.J. Lenczowski and J.B. Giesbers. “Perpendicular giant magnetoresistance of Fe/Cr magnetic multilayers from 4.2 to 300K”. *Phys. Rev. Lett.* **70**, 3343 (1993).

[23] P.M. Tedrow and R. Meservey. “Spin polarization of electron tunneling from films of Fe, Co, Ni and Gd”. *Phys. Rev. B* **7**, 318 (1973).

[24] M. Julliere. “Tunneling between ferromagnetic films”. *Phys. Lett.* **54a**, 225 (1975).

[25] J.S. Moodera, L.R. Kinder, T.M. Wong and R. Meservey. “Large magnetoresistance at room temperature in ferromagnetic thin film tunnel junctions”. *Phys. Rev. Lett.* **74**, 3273 (1995).

[26] T. Miyazaki and N. Tezuka. “Giant magnetic tunneling effect in Fe/Al_2O_3/Fe junction”. *J. Magn. Magn. Mater.* **139**, L231 (1995).

[27] M. Sharma, S.X. Wang and J.H. Nickel. “Inversion of spin polarization and tunnel magnetoresistance in spin-dependent tunneling junctions”. *Phys. Rev. Lett.* **82**, 616 (1999).

[28] D.J. Monsma, R. Vlutters and J.C. Lodder. “Room temperature-operating spin-valve transistors formed by vacuum bonding”. *Science* **281**, 407 (1998).

[29] P.S. Anil Kumar, R. Jansen, O.M.J. van ’t Erve, R. Vlutters, P. de Haan and J.C. Lodder. “Low-Field magnetocurrent above 200 percent in a spin-valve transistor at room temperature”. *J. Magn. Magn. Mater.* **214**, L1 (2000).

[30] T. Kinno, K. Tanaka and K. Mizushima. “Ballistic-electron-emission spectroscopy on an Fe/Au/Fe multilayer”. *Phys. Rev. B.* **56**, R4391 (1997).

[31] W.H. Rippard and R.A. Buhrman. “Ballistic electron magnetic microscopy: imaging magnetic domains with nanometer resolution”. *Appl. Phys. Lett.* **75**, 1001 (1999).

[32] A. Filipe, H.J. Drouhin, G. Lampel, Y. Lassailly, J. Nagle, J. Peretti, V.I. Safarov and A. Schuhl. “Spin-dependent transmission of electrons through the ferromagnetic metal base of a hot-electron transistorlike system”. *Phys. Rev. Lett.* **80**, 2425 (1998).

[33] K. Mizushima, T. Kinno, T. Yamauchi and K. Tanaka. “Energy-dependent hot electron transport across a spin-valve”. *IEEE Trans. Magn.* **33**, 3500 (1997).

[34] K. Mizushima, T. Kinno, K. Tanaka and T. Yamauchi. “Strong increase of the effective polarization of the tunnel current in Fe/AlO_x/Al junctions with decreasing Fe layer thickness”. *Phys. Rev. B.* **58**, 4660 (1998).

[35] G.A. Prinz. “Magnetoelectronic applications”. *J. Magn. Magn. Mat* **200**, 57 (1999).

[36] Symposium und Statusseminar in Wetzlar, Germany. “Magnetoresistive Sensoren IV”. University Erlangen-Nurnberg (1997).

[37] W.C. Black Jr. and B. Das. “Programmable logic using giant-magnetoresistance and spin-dependent tunneling devices”. *J. Appl. Phys.* **87**, 6674 (2000).

[38] K.E. Johnson. “Magnetic materials and structures for thin-film recording media”. *J. Appl. Phys.* **87**, 5365 (2000).

[39] http://www.research.ibm.com and http://www.storage.ibm.com.

[40] S. Araki, M. Sano, S. Li, Y. Tsuchiya, O. Redon, T. Sasaki, N. Ito, K. Terunuma, H. Morita and M. Matsuzaki. “Which spin valve for next giant magnetoresistance head generation?”. *J. Appl. Phys.* **87**, 5377 (2000).

[41] T.D. Howell, P. A. McEwen and A. Patapoutian. “Getting the information in and out: the channel”. *J. Appl. Phys.* **87**, 5371 (2000).

[42] S.S.P. Parkin et. al. “Exchange-biased magnetic tunnel junctions and application to nonvolatile magnetic random access memory”. *J. Appl. Phys.* **85**, 5828 (1999).

[43] P.P. Freitas, editor. “Spin tunnel junctions,TJ-RAMS and TJ-Read Heads” Rhodes (Greece) (1999). Summer School on "Mesomagnetism, Spin Dynamics and Spin Electronics" Summerschool Proceedings.

[44] S. Tehrani, J.M. Slaughter, E. Chen, M. Durlan, J. Shi and M. DeHerrera. “Progress and outlook for MRAM technology”. *IEEE Trans. Magn.* **35**, 2814 (1999).

[45] D.J. Monsma. “The spin-valve transistor”. PhD thesis Electrical Engineering Univ. of Twente, 7500AE Enschede, The Netherlands (1998).

[46] K. Dessein, H. Boeve, P.S. Anil Kumar, J. De Boeck, J.C. Lodder, L. Delaey and G. Borghs. “Evaluation of vacuum bonded GaAs/Si spin-valve transistors”. *J. Appl. Phys.* **87**, 5155 (2000).

[47] S.M. Sze. “Physics of semiconductor devices”. John Wiley & Sons, Inc 2nd edition (1981).

[48] C.R. Crowell. “The Richardson constant for thermionic emission in schottky barrier diodes”. *Solid. St. El.* **8**, 395 (1965).

[49] C.R. Crowell and S.M. Sze. “Current transport in metal-semiconductor barriers”. *Solid. St. El.* **9**, 1035 (1966).

[50] S.M. Sze. “Physics of Semiconductor Devices”. Wiley New York 1st edition (1969).

[51] L.D. Bell. “Evidence of Momentum Conservation at a Nonepitaxial Metal/Semiconductor Interface Using Ballistic Electron Emission Microscopy”. *Phys. Rev. Lett.* **77**, 3893 (1996).

[52] C.R. Crowell and S.M. Sze. "Electron–optical-phonon scattering in the emitter and collector barriers of semiconductor-metal-semiconductor structures". *Solid. St. El.* **8**, 979 (1965).

[53] D.K. Guthrie, L.E. Harrell, G.N. Henderson, P.N. First, T.K. Gaylord, E.N. Glytsis and R.E. Leibenguth. "Ballistic-electron-emission spectroscopy of Au/Si and Au/GaAs interfaces: Low-temperature measurements and ballistic models". *Phys. Rev. B* **54**, 16972 (1996).

[54] R. Ludeke and A. Bauer. "Electrical transport properties of hot electrons at metal, insulator and semiconductor interfaces". *J. Vac. Sci. Technol. A* **13**, 614 (1995).

[55] D.L. Smith, E.Y. Lee and V. Narayanamurti. "Ballistic Electron Emission Microscopy for Nonepitaxial Metal/Semiconductor Interfaces". *Phys. Rev. Lett.* **80**, 2433 (1998).

[56] E.Y. Lee and L.J. Schowalter. "Phonon scattering and quantum mechanical reflection at the Schottky barrier". *J. Appl. Phys.* **70**, 2156 (1991).

[57] C.R. Crowell and S.M. Sze. "Quantum-mechanical reflection of electrons at metal-semiconductor barriers: electrons transport in semiconductor-metal-semiconductor structures". *J. Appl. Phys.* **37**, 2683 (1966).

[58] Y. Ando and T. Itoh. "Calculation of transmission tunneling current across arbitrary potential barriers". *J. Appl. Phys.* **61**, 1497 (1987).

[59] S.M. Sze, C.R. Crowell, G.P. Carey and E.E. LaBate. "Hot-electron transport in semiconductor-metal-semiconductor structures". *J. Appl. Phys.* **37**, 2690 (1966).

[60] N.W. Ashcroft and N.D. Mermin. "Solid State Physics". Saunders College Publishing (1976).

[61] T. Valet and A. Fert. "Theory of the perpendicular magnetoresistance in magnetic multilayers". *Phys. Rev. B.* **48**, 7099 (1993).

[62] E. Zarate, P. Apell and P.M. Echenique. "Calculation of low-energy-electron lifetimes". *Phys. Rev. B.* **60**, 2326 (1999).

[63] R. Knorren, K. H. Bennemann, R. Burgermeister and M. Aeschlimann. "Dynamics of excited electrons in copper and ferromagnetic transition metals: Theory and experiment". *Phys. Rev. B* **61**, 9427 (2000).

[64] H-J. Drouhin. "Low-energy electron mean free path and its spin dependence in transition metals". *Phys. Rev. B.* **56**, 14886 (1997).

[65] H-J. Drouhin. "Total scattering cross section of spin-polarized low-energy electrons in transition metals". *Phys. Rev. B.* **62**, 556 (2000).

[66] Ph. Lambin and F. Herman. "Electronic and magnetic structure of metallic multilayers: Ni_3Fe-FeMn system". *Phys. Rev. B.* **30**, 6903 (1984).

[67] M. Aeschlimann, M. Bauer, S. Pawlik, W. Weber, R. Burgermeister, D. Oberli and H. C. Siegmann. "Ultrafast Spin-Dependent Electron Dynamics in fcc Co". *Phys. Rev. Lett.* **79**, 5158 (1997).

[68] M. Plihal, D. L. Mills and J. Kirschner. "Spin Wave Signature in the Spin Polarized Electron Energy Loss Spectrum of Ultrathin Fe Films: Theory and Experiment". *Phys. Rev. Lett.* **82**, 2579 (1999).

[69] C. Kittel. "Introduction to solid state physics". Wiley and Sons, inc. (1996 (original 1953)).

[70] R.H. Brown, D.M.C. Nicholson, Xindong Wang and T.C. Schulthess. "First principles theory of spin waves in Fe, Co, and Ni". *J. Appl. Phys.* **85**, 4830 (1999).

[71] J. Hong and D. L. Mills. "Theory of the spin dependence of the inelastic mean free path of electrons in ferromagnetic metals: A model study". *Phys. Rev. B.* **59**, 13840 (1999).

[72] J. Hong and D. L. Mills. "Spin dependence of the inelastic electron mean free path in Fe and Ni: Explicit calculations and implications". *Phys. Rev. B.* **62**, 5589 (2000).

[73] T. Yamauchi and K. Mizushima. "Theoretical approach to the spin-dependent hot-electron transport in a spin valve". *Phys. Rev. B.* **58**, 1934 (1998).

[74] T. Yamauchi and K. Mizushima. "Theoretical analysis of energy-dependent hot-electron transport in a magnetic multilayer". *Phys. Rev. B.* **60**, 8242 (2000).

[75] J. Garcia-Garcia, X. Oriols, F. Martin and J. Sune. "Comparison between the relaxation time approximation and the boltzmann collision operator for simulation of dissipative electron transport in resonant tunnelling diodes". *Solid-State El.* **39**, 1795 (1996).

[76] E.M. Lifshitz and L.P. Pitaevskii. "Physical kinetics" volume 10 of *Course of theoretical physics*. Pergamon (1981).

[77] R. Lake, G. Klimeck, R.C. Bowen and D. Jovanovic. "Single and multiband modeling of quantum electron transport through layered semiconductor devices". *J. Appl. Phys.* **81**, 7845 (1997).

[78] G.D. Mahan. "Hot electrons in one dimension". *J. Appl. Phys.* **58**, 2242 (1985).

[79] W.H. Rippard and R.A. Buhrman. "Spin-dependent hot-electron transport in Co/Cu thin films". *Phys. Rev. Lett.* **84**, 971 (2000).

[80] M.K. Weilmeier, W.H. Rippard and R.A. Buhrman. "Ballistic electron transport through Au (111)/Si(111) and Au(111)/Si(100) interfaces". *Phys. Rev. B.* **59**, R2521 (1999).

[81] P. Niedermann, L. Quattropani, K. Solt, I. Maggio-Aprile and O. Fischer. "Hot-carrier scattering in a metal: A ballistic-electron-emission microscopy investigation on PtSi". *Phys. Rev. B* **48**, 8833 (1993).

[82] J.C. Hensel, A.F.J. Levi, R.T. Tung and J.M. Gibson. "Transistor action in Si/$CoSi_2$/Si hetrostructures". *Appl. Phys. Lett.* **47**, 151 (1985).

[83] T. Shimatsu, R.H. Mollema, D.J. Monsma, E.G. Keim and J.C. Lodder. "Metal bonding during sputter film deposition". *J. Vac. Sci. & Tech. A* **16**, 2125 (1998).

[84] S.D. Kim, O.M.J. van 't Erve, R. Jansen, P.S. Anil Kumar, R. Vlutters and J.C. Lodder. "Fabrication technology for miniaturazation of the spin-valve transistor". *Sens. Actuators A.* (to be published).

[85] R.H. Norton. “Four-point magnetoresistance measurements”. *IEEE Trans. Magn.* **19**, 1579 (1983).

[86] F.E. Jones, B.P. Wood, J.A. Myers, G.Daniels-Hafers and M.C. Lonergan. “Current transport and the role of barrier inhomogeneities at the high barrier n-InP|poly(pyrrole) interface”. *J. Appl. Phys* **86**, 6431 (1999).

[87] G. Gomila. “Effects of interface states on the non-stationary transport properties of Schottky contacts and metal-insulator-semiconductor tunnel diodes”. *J. Phys. D: Appl. Phys.* **32**, 64 (1999).

[88] Keiji Maeda and Eiji Kitahara. “Metal-induced gap states model of nonideal Au/Si Schottky barrier with low defect density”. *Applied Surface Science* **130-132**, 925 (1998).

[89] R.T. Tung. “Electron transport at metal-semiconductor interfaces: General theory”. *Phys. Rev. B* **45**, 13509 (1992).

[90] R.F. Schmitsdorf, T.U. Kampen and W. Monch. “Explanation of the linear correlation between barrier heights and ideality factors of real metal-semiconductor contacts by laterally nonuniform Schottky barriers”. *J. Vac. Sci. & Tech. B* **15**, 1221 (1997).

[91] E.H. Rhoderick and R.H. Williams. “Metal-Semiconductor Contacts”. Clarendon Press Oxford 2nd edition (1988).

[92] L. D. Bell. “Momentum conservation for hot electrons at the Au/Si(111) interface observed by ballistic-electron-emission microscopy”. *J. Vac. Sci. Technol. A* **15**, 1358 (1997).

[93] R. Jansen, P.S.Anil Kumar, O.M.J. van ’t Erve, R. Vlutters, P. de Haan and J.C. Lodder. “Thermal spin-wave scattering in hot-electron magnetotransport across a spin valve”. *Phys. Rev. Lett.* **85**, 3277 (2000).

[94] J. Hong and D.L. Mills. “Theory of the spin dependence of the inelastic mean free path of electrons in ferromagnetic metals: A model study”. *Phys. Rev. B* **59**, 13840 (1999).

[95] J.R. Waldrop, R.W. Grant, Y.C. Wang and R.F. Davis. “Metal schottky barrier contacts to alpha 6H-SiC”. *J. Appl. Phys.* **72**, 4757 (1992).

[96] A. L. Vazquez de Parga, F. J. Garcia-Vidal and R. Miranda. “Detecting Electronic States at Stacking Faults in Magnetic Thin Films by Tunneling Spectroscopy”. *Phys. Rev. Lett.* **85**, 4365 (2000).

[97] C. Detavernier, R. L. Van Meirhaeghe, R. Donaton, K. Maex and F. Cardon. “Ballistic electron emission microscopy study of barrier height inhomogeneities introduced in Au/n-Si Schottky contacts by a HF pretreatment”. *J. Appl. Phys.* **84**, 3226 (1998).

[98] H. Sirringhaus, T. Meyer, E. Y. Lee and H. von Kanel. “Spatial variations of hot-carrier transmission across $CoSi_2$/Si interfaces on a nanometer scale”. *Phys. Rev. B* **53**, 15944 (1996).

[99] J. H. Werner and H. H. Gijttler. “Barrier inhomogeneities at Schottky contacts”. *J. Appl. Phys.* **69**, 1522 (1991).

[100] S. Chandrasekhar. “Radiative transfer”. New York etc. : Dover (1960).

[101] M. Labrune, J.C.S. Kools and A. Thiaville. “Magnetization rotation in spin-valve multilayers”. *J. Magn. Magn. Mat.* **171**, 1 (1997).

Appendices

A.1 Transport over the Schottky barriers

In this section of the appendix, several derivations to explain the current transport over Schottky diodes can be found. First, we will derive the energy spectrum of the injected electrons from a Schottky diode. Next, we derive the angular emission and collection spectrum, which are used as boundary conditions in the Boltzmann model. And finally we will show how the energy dependence of the collection spectrum and distributed Schottky barriers can explain the increase of current transfer with temperature, as found in metal base transistors.

A.1.1 Energy emission spectrum

The thermionic emission current integral (2.10) can be written with reduced variables as:

$$J_e = \left[A^* T^2 \exp(-\frac{qV_n}{kT})\right] \int_{x_{\min}}^{\infty} x \exp(-x^2) \times \int_{-\infty}^{\infty} \exp(-y^2) \int_{-\infty}^{\infty} \exp(-z^2) dxdydz \tag{A.1}$$

in which the following simplifying definitions were used:

$$x^2 \equiv \frac{m_{Si}^* v_x^2}{2kT} \qquad y^2 \equiv \frac{m_{Si}^* v_y^2}{2kT} \qquad z^2 \equiv \frac{m_{Si}^* v_z^2}{2kT} \tag{A.2}$$

And the under-limit of the x integration can be written as:

$$x_{\min} = \sqrt{\frac{q(V_{bi} - V)}{kT}} \tag{A.3}$$

By a transformation into cylindrical co-ordinates ($[x, y, z]$ into $[x, r, \theta]$ and integrating out θ and integrating over only the electrons with energy less than or equal to E, the current of electrons with energies upto E is obtained:

$$J_e^{upto} = \left[\frac{2A^* T^2}{\pi} \exp(-\frac{qV_n}{kT})\right] \int_{x_{\min}}^{x_{\max}} x \exp(-x^2) \times \int_{r_{\min}}^{r_{\max}} 2\pi r \exp(-r^2) dxdr \tag{A.4}$$

with:

$$x_{\min} = \sqrt{\tfrac{(q\Phi_B - qV_n - qV)}{kT}} \qquad r_{\min} = 0$$
$$x_{\max} = \sqrt{\tfrac{(E - qV_n - qV)}{kT}} \qquad r_{\max} = \sqrt{\tfrac{(E - qV_n - qV)}{kT} - x^2}$$

By a differentiation of J_e^{upto} to E, the energy resolved emission current ($J_e(E)$) of the Schottky diode is obtained:

$$J_e(E) = \frac{dJ_e^{upto}}{dE} = \left[\left(\frac{A^* q}{k^2}\right)(E - \Phi_B) \exp(-\frac{qE}{kT})\right] \exp(\frac{qV}{kT}) \tag{A.5}$$

As a check this formula can be integrated over the energy and the well-known forward current formula is obtained:

$$J_e = \int_{\Phi_b}^{\infty} J_e(E)dE = A^* T^2 \exp(-\frac{q\Phi_B}{kT}) \exp(\frac{qV}{kT}) \tag{A.6}$$

A.1.2 Angular emission spectrum

In order to calculate the dependence of the angular distribution in the metal of the injected electrons from a Schottky diode, we need to transform Eq. 2.10 from the semiconductor to the metal coordinate system of velocities. For this purpose, we use a free electron model without scattering in order to obtain simple formula that can be used as integral transformation rules. Out of parallel momentum conservation across the semiconductor–metal interface, v_{my} and v_{mz} can be expressed in v_{sy} and v_{sz} like:

$$\begin{aligned} v_{my} &= \frac{m_{si}^*}{m_m^*} v_{sy} \\ v_{mz} &= \frac{m_{si}^*}{m_m^*} v_{sz} \end{aligned} \tag{A.7}$$

And from the total energy conservation (see Eq. 2.19), one can obtain v_{mx}:

$$v_{mx} = \sqrt{\frac{m_{si}^*}{m_m^*}\left[v_{sx}^2 + \left(1 - \frac{m_{si}^*}{m_m^*}\right)\left(v_{sy}^2 + v_{sz}^2\right)\right] + \frac{2}{m_m^*}\left[q\Phi_B + E_C + qV - qV_{bi}\right]} \tag{A.8}$$

Which can be simplified into:

$$v_{mx} = \sqrt{\frac{m_{si}^*}{m_m^*} v_{sx}^2 + \frac{2}{m_m^*}\left[q\Phi_B + E_C + qV - qV_{bi}\right]} \tag{A.9}$$

because $\frac{1}{2}m_{si}^*\left(v_{sy}^2 + v_{sz}^2\right) \ll q(V - V_{bi}) \leq \frac{1}{2}m_{si}^* v_{sx}^2$, in other words, most of the kinetic energy of an electron in the conduction band has to be attributed to the x-velocity, otherwise the electron can not even come over the internal bandbending barrier, and any extra velocity in the y and z-direction will only become less probable due to the Fermi-Dirac statistics (2.2). With A.7 and A.9 we can transform the thermionic emission integral (2.10) from the velocity coordinates in the silicon to the velocity coordinates in the metal. Like the minimum velocity in the x-direction in the silicon, there is a similar minimum velocity in the x-direction in the metal, given by:

$$v_{mx-min} = \sqrt{\frac{2}{m_m^*}(q\Phi_B + E_C)} \tag{A.10}$$

from which we have to integrate upward (and over $-\infty..\infty$ for v_{my} and v_{mz}) to obtain the total amount of current again.

Next, these velocities can be transformed from the cartesian coordinates into spherical coordinates by replacing (v_{mx}, v_{mz} and v_{mz}) with the following relations:

$$v_{mx} = v_{mR}\mu \tag{A.11}$$

$$v_{my} = v_{mR}\sqrt{1-\mu^2}\cos\phi \tag{A.12}$$

$$v_{mz} = v_{mR}\sqrt{1-\mu^2}\sin\phi \tag{A.13}$$

in which v_{mR} is the absolute velocity in the metal, μ the directional cosine, and ϕ the angle of the projection on the y-z plane with the y axis. The integral function can then be integrate over only ϕ and v_{mR} , so that one obtains $I_e(\mu)$. ϕ has to be integrated from 0 to 2π, and v_{mR} from v_{mx-min}/μ (in order to ensure enough velocity in the x-direction) to infinity.
By calculating the angular distribution with integral transformations, the total amount of current is still given by:

$$J_e = \int_0^1 J_e(\mu)d\mu = A^*T^2\exp(-\frac{q\Phi_B}{kT})\exp(\frac{qV}{kT}) \tag{A.14}$$

Furthermore, we can not only calculate the angular current distribution, but also the Boltzmann distribution (defined as the number of electrons per second) belonging to the injected electrons, because we can write:

$$f_e(\mu) = \frac{I_e(\mu)}{q\mu} \tag{A.15}$$

In this way we can use the above calculation as a boundary condition at the emitter side in our base transport calculations. In Fig. A.1, we show the angular distribution function of the emitted electrons vs. μ. As can be seen, all the current is injected in a very small angle close to the normal of the silicon/metal interface. Most of the current is injected at 0°, and the angular current density drops down rapidly with increasing angle. The angular distribution becomes wider with temperature, because the electrons will have more energy (see Fig. 2.4), resulting in a higher critical angle (see Fig. 2.5).

A.1.3 Angular acceptance spectrum

By using a free electron model with an isotropic effective mass, it is possible to relate the velocity in the collector with the velocity in the metallic base, which are given in formula form by Eq. 2.22 and 2.23. As explained in the theory chapter, the velocity in x-direction (v_{sx}) should remain positive, otherwise the electron is reflected (classical reflection) back into the base (resulting in an imaginary v_{sx}) .

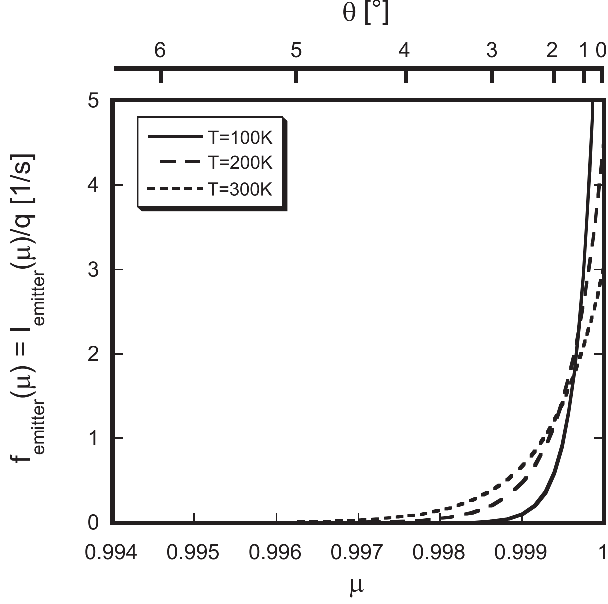

Figure A.1: *The angular emission spectrum for the emitter ($F_{emitter}$) as function of $\mu = \cos\theta$ for T=100, 200 and 300K. The electrons are emitted over an 0.9 eV Schottky barrier with E_{FM}=5.5 eV and $\sum_i a_i \mu_i f(\mu_i) = 2 \cdot 10^{-3}$. Because all electrons are injected where $\mu \approx 1$ we can write: $f_e(\mu) \approx I_e(\mu)/q$.*

In order to calculate the quantum mechanical reflection, we model the Schottky barrier as an abrupt step from the minimum of the conduction band in the metal (E_C below the Fermi-level) to the maximum of the conduction band in the silicon ($q\Phi_C$ above the Fermi-level). In this case there exists a simple formula for the quantum mechanical reflection [53, 63]. The total reflectivity R (classical+quantum mechanical) is then given by:

$$R = \left\{ \begin{array}{cc} 1 & \text{if} \quad (v_{sx})^2 \leq 0 \\ \left| \dfrac{(v_{mx} - v_{sx})}{(v_{mx} + v_{sx})} \right|^2 & \text{if} \quad (v_{sx})^2 > 0 \end{array} \right\} \tag{A.16}$$

After which the transmission is simply $T = 1 - R$. With this model, the collection probability of an electron with a certain speed vector in the metal can be calculated ($T(v_{mx}, v_{my}, v_{mz})$). Next, we can use the same spherical coordinates as in our Boltzmann approach, given by:

$$v_{mx} = v_{mR}\mu \tag{A.17}$$

$$v_{my} = v_{mR}\sqrt{1-\mu^2}\cos\phi \tag{A.18}$$

$$v_{mz} = v_{mR}\sqrt{1-\mu^2}\sin\phi \tag{A.19}$$

In this way, we obtain $T(v_{mR}, \mu)$ (independent of ϕ, due to cylindrical symmetry of the problem). Because the transmission is dependent on the velocity (v_{mR}) of the incoming electrons, we use a velocity-resolved emission spectrum from the emitter (similar like Eq. A.5 but with v_{mR} instead of E). So we sample the transmission function with the normalized v_{mR}-resolved emitter current and this finally results in the angular dependence of the collection factor:

$$T(\mu) = \int T(v_{mR}, \mu) \cdot I_e^{norm}(v_{mR}) dv_{mR}. \tag{A.20}$$

This function is plotted in Fig. A.2 for an 0.8 eV collector barrier when the electrons are emitted from an 0.9 eV emitter barrier at 3 different temperatures. When we compare Fig. A.1 and A.2, it can be see that the collection spectrum is broader than the emission spectrum. This ensures the collection of electrons that are not elastically scattered, but will cause reflection of most of the elastically scattered electrons. The shown temperature dependence is due to the higher energy of the emitted electrons at higher energies, and is not related to the quantum mechanical transmission.
The angular transmission as shown in Fig. A.2 is used in the transport calculations as boundary condition. From the incoming distribution ($f^>(\mu)$) at the collector side, only $T(\mu) \cdot f^>(\mu)$ is transmitted and contributes to the collector current. The other part ($[1 - T(\mu)] \cdot f^>(\mu)$) will be reflected back into the base.

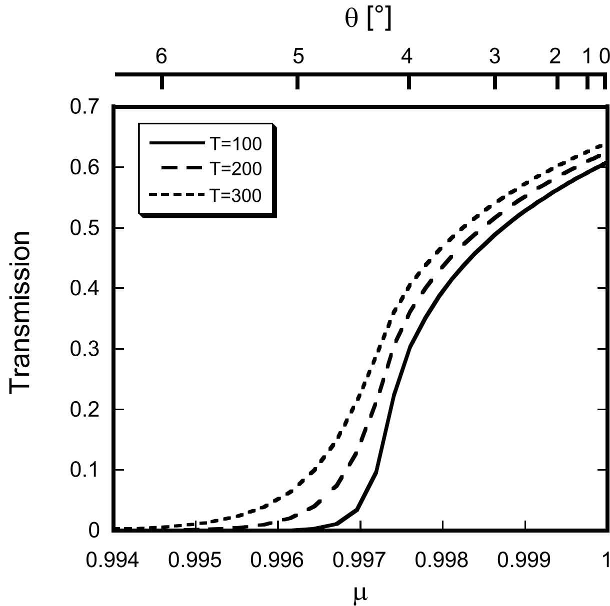

Figure A.2: *The angular transmission of a Schottky collector, when electrons are emitted out of a 0.9eV Schottky barrier and collected in a 0.8eV Schottky barrier at 3 different temperatures.*

A.1.4 Temperature dependent current transfer

The increase in current transfer with temperature as observed in our MBT/ SVT's, is due to the properties of the Schottky barriers. Two different mechanism have been identified that lead to this effect. The main contribution is the increase of acceptance cone angle with hot-electron energy, the second is current transport over non-uniform Schottky barriers. Both these effect are theoretically explained in this section.

A.1.4.1 Emission energy-Acceptance cone effects

When there is strong elastic scattering in the base of a MBT/SVT, the momentum distribution ($f^{>}(\mu)$) will become isotropic and the collector current will depend on the acceptance cone angle θ_c (Eq. 2.24). To be more precise, the collector current will scale linearly with the spherical angle Ω, which is related to collection cone angle by: $\sin(\theta_c/2)^2$. Because the angle θ_c is practically always below 10°, we may write Ω as function of the hot-electrons energy as:

$$\Omega = \sin(\theta_c/2)^2 \simeq \frac{1}{4}\sin(\theta_c)^2 = \frac{m_{si}^*}{4m^*}\left(\frac{E - q\Phi_c}{E + E_C}\right) \tag{A.21}$$

This hot-electron energy will change as function of the temperature. If the (normalized) energy spectrum from the Schottky emitter (Eq. A.5 / Eq. A.6) is not changed in the base, one can calculate the resulting temperature dependence of Ω (which is proportional to I_c) by:

$$\Omega(T) = \int_{q\Phi_e}^{\infty}\left[\frac{m_{si}^*}{4m^*}\left(\frac{E - q\Phi_c}{E + E_C}\right)\right]\frac{J_e(E)}{J_e}dE \tag{A.22}$$

One can calculate this integral analytically, and after some arrangements $\Omega(T)$ can be written as:

$$\Omega(T) = \frac{m_{si}^*}{4m^*}\left(1 + X_c\left[X_e\,\mathrm{Ei}(1, X_e)\exp(X_e) - 1\right]\right) \tag{A.23}$$

In which $X_e = \frac{q}{kT}(E_C + q\Phi_e)$, $X_c = \frac{q}{kT}(E_C + q\Phi_c)$ and Ei(n,x) is the exponential integral, defined as $\int_1^{\infty}\left[e^{-xt}/t^n\right]\,dt$. With Eq. A.23, one can now calculate the increase in collector current compared to T=100K (i.e. $\Omega(T)/\Omega(100K)$). This has been done in Fig. A.3, which shows the relative increase with temperature of the spherical angle Ω for different devices in which the difference between the emitter and collector Schottky barrier has been varied. As can be seen, this theory explains the linear increase of I_c with temperature, and the steeper slope with smaller Schottky barrier difference, exactly as observed in our experiments.
It should be noted that this effect can also calculated by the Boltzmann transport model, because the boundary conditions at the collector are calculated with the energy spectrum from the emitter (see Eq. A.20). Furthermore, calculations with the Boltzmann model show that the slope is related to how isotropic the momentum

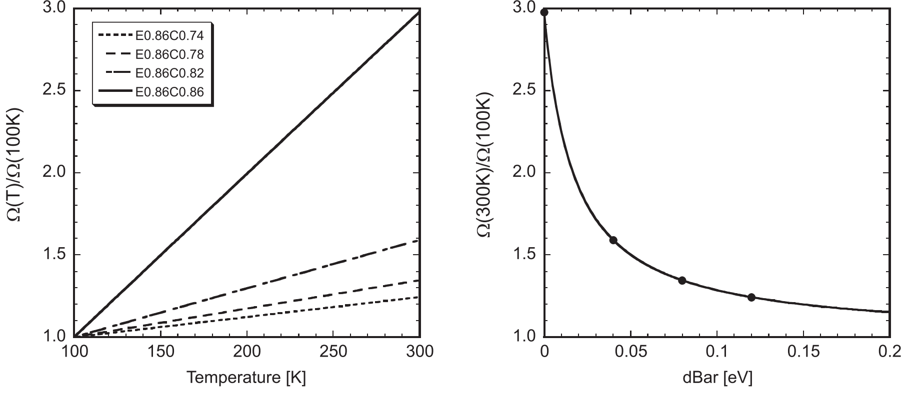

Figure A.3: *On the left, the normalized* Ω *vs. temperature for* $q\Phi_e$*=0.86eV and* $q\Phi_c$*=0.86, 0.82, 0.78 and 0.74eV. On the right, the* $\Omega(300)/\Omega(100)$ *vs. dBar (*$= q(\Phi_e - \Phi_c)$*) (*E_c*=5.5eV).*

distribution has become (the more isotropic, the higher the slope, with a maximum slope defined by the analytical model).

A.1.4.2 Schottky barrier distribution effects

The increase in current transfer in a metal base transistor can also be explained when there is an overlap of the Schottky barrier distribution from the emitter and the collector. That Schottky barriers aren't uniform can be experimentally verified by BEEM [97, 98] and several current transport theories were developed to explain the I-V characteristics of non-uniform Schottky barriers [89, 99].
Here, we calculate how many electrons that are emitted from a Schottky diode with a gaussian distribution have enough energy to come over a distributed collector diode. Although a gaussian distribution might not be realistic, it shows many aspects of the hot-electron transport over these distributed barriers.
The capability of injecting hot-electrons with the distributed emitter diode is expressed by: α_e^{hot}, which can be inserted as extra attenuation factor in Eq. 4.5. α_e^{hot} is defined as the fraction of the total emitter current (I_e) that has enough energy to overcome the collector barrier (I_e^{hot}), i.e.:

$$\alpha_e^{hot} \equiv \frac{I_e^{hot}}{I_e} \tag{A.24}$$

In the case of a perfect Schottky diode with only one barrier height, the energy distribution of the emitted electrons is given by (Eq. A.5):

$$I_e(E, \Phi_e) = \left[\left(\frac{AreaA^* q}{k^2} \right) (E - \Phi_e) \exp(-\frac{qE}{kT}) \right] \exp(\frac{qV}{kT}) \tag{A.25}$$

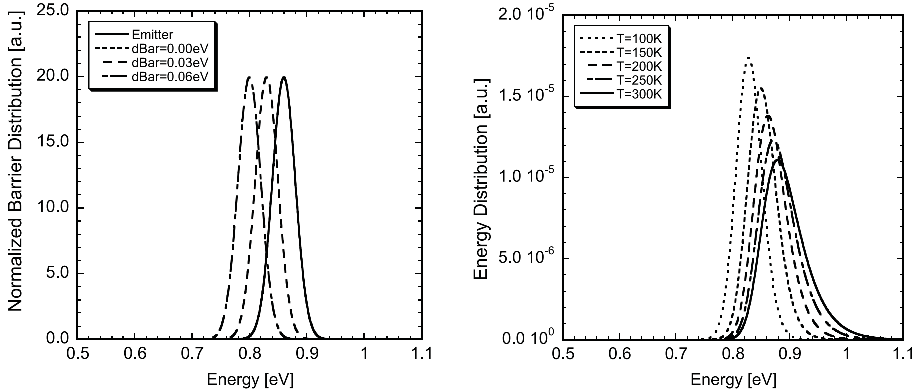

Figure A.4: *On the left, the Schottky barrier distribution of the emitter ($\bar{\Phi}_e = 0.86eV$ and $W_e = 0.02$) and the collector ($\bar{\Phi}_c$ =0.86, 0.83 and 0.80eV and $W_c = 0.02$) . On the right, the energy dependence of the injected electrons at different temperatures for the same emitter.*

So if we do not have a sharp barrier but a distribution, given by:

$$f(\Phi, \bar{\Phi}, W) = \frac{1}{\sqrt{2\pi}W} \exp^{-\frac{\left(\Phi - \bar{\Phi}\right)^2}{2W^2}} \tag{A.26}$$

we can calculate the energy of the electrons that are injected over this distributed barrier. As shown in Fig. 2.4, electrons are only injected over a sharp barrier with an energy larger than the Schottky barrier height. This means that if we want to calculate the number of electrons that is injected from a distributed emitter at, for example, 1.0eV, we have to look at how many ($f(\Phi_e, \bar{\Phi}_e, W_e)$) local barriers there are below 1.0eV and from every of these local barriers, how many electrons are injected ($I_e(1.0eV, \Phi_e)$) at 1.0eV [1]. This can be written in integral form as:

$$I_e(E) = \int_0^E d\Phi_e \left[f(\Phi_e, \bar{\Phi}_e, W_e) I_e(E, \Phi_e) \right] \tag{A.27}$$

This function and the Schottky barrier distribution of the emitter diode are shown in Fig. A.4, which shows clearly that by cooling down a diode, most of the current will pass over the lower parts of the barrier, resulting in a lower average energy.

Next, one has to determine how many of these injected electrons have more energy than the local collector barrier (I_e^{hot}), which is also distributed (see Fig. A.4). This can be done by integrating over the collector barrier distribution, and determine at every position on the collector distribution how many electrons are emitted above this

1 This is only true in the case of pure thermionic transport over the top of the barrier. There might be transport through the barrier, which in that case, should be taken into account

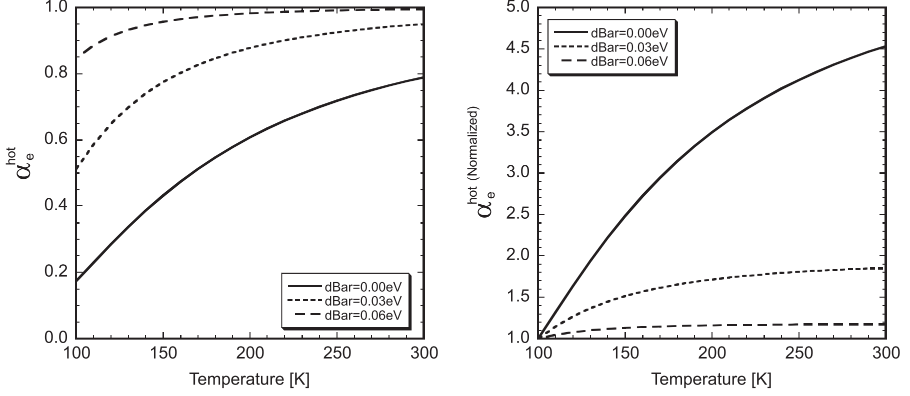

Figure A.5: *On the left: the calculated α_e^{hot} as function of the temperature for a broad emitter barrier at 0.86eV and a collector at dBar below (so at 0.86, 0.83 and 0.80 eV, all with $W_e = W_c$=0.02). On the right this α_e^{hot} is normalized at T=100K.*

barrier, which can be written in integral form as:

$$I_e^{hot} = \int_0^{\infty} d\Phi_c \left[f(\Phi_c, \bar{\Phi}_c, W_c) \right] \int_{\Phi_c}^{\infty} dE \left[I_e(E) \right] \tag{A.28}$$

Now we know the total emitter current and how many of these electrons are emitted above the collector barrier, we can calculate α_e^{hot}:

$$\alpha_e^{hot} \equiv \frac{I_e^{hot}}{I_e} = \frac{\int_0^{\infty} d\Phi_c \left[f(\Phi_c, \bar{\Phi}_c, W_c) \right] \int_{\Phi_c}^{\infty} dE \left[I_e(E) \right]}{\int_0^{\infty} dE \left[I_e(E) \right]} \tag{A.29}$$

With this formula, we can plot α_e^{hot} vs. temperature and can normalize it at the T=100K, resulting in Fig. A.5.

A.2 Transport through the base

In this section of the appendix we will summarize the various solutions and methods to describe the current transport through the base. First we show how to obtain an analytical solution to the 3-dimensional Boltzmann equation, and after that, how to do this numerically. At the end we take the 1-directional model and derive how we can include spin-wave scattering that mixes the spin-up and down channels.

A.2.1 Analytical solution of the 3-D Boltzmann equation

For the 3-dimensional Boltzmann equation as derived in the theory chapter (page 37):

$$\mu\frac{\partial f(x,\mu)}{\partial x} = -\left[\frac{1}{\lambda_e}+\frac{1}{\lambda_i}\right]f(x,\mu)+\frac{1}{2\lambda_e}\int_{-1}^{1} f(x,\mu)d\mu, \tag{A.30}$$

it is possible to find an analytic solution. The derivation, and the resulting attenuation length as function of the elastic and inelastic scattering are shown below.
As known, there will most probably be an exponential attenuation with thickness, so we make the following ansatz:

$$f(x,\mu) = A(\mu)e^{-\frac{x}{\lambda_{eff}}}. \tag{A.31}$$

When this is substituted into Eq. A.30 and the expressions are divide by the common $e^{-\frac{x}{\lambda_{eff}}}$ factor, we obtain:

$$-\frac{\mu A(\mu)}{\lambda_{eff}} = -\frac{A(\mu)}{\lambda_e}-\frac{A(\mu)}{\lambda_i}+\frac{1}{2\lambda_e}\int_{-1}^{1} A(\mu)d\mu \tag{A.32}$$

By collecting all the $A(\mu)$'s on the left and putting all the prefactors below the integral on the right we can write:

$$A(\mu) = \frac{1}{2\lambda_e}\frac{\int_{-1}^{1} A(\mu)d\mu}{\left(\frac{1}{\lambda_e}+\frac{1}{\lambda_i}-\frac{\mu}{\lambda_{eff}}\right)} \tag{A.33}$$

Next, we integrate both sides over μ from -1 to 1 and divide the common integral out of Eq. A.33:

$$1 = \int_{-1}^{1}\frac{1}{2\lambda_e}\frac{1}{\left(\frac{1}{\lambda_e}+\frac{1}{\lambda_i}-\frac{\mu}{\lambda_{eff}}\right)}d\mu \tag{A.34}$$

After calculating the integral, we obtain:

$$1 = \frac{\lambda_{eff}}{2\lambda_e}\ln\left[\frac{(\lambda_e+\lambda_i)\lambda_{eff}+\lambda_e\lambda_i}{(\lambda_e+\lambda_i)\lambda_{eff}-\lambda_e\lambda_i}\right] \tag{A.35}$$

For a given value of λ_e and λ_i, there is a special λ_{eff} that makes Eq. A.35 true. There is no analytical formula to obtain λ_{eff}, but numerically it can be easily obtained with Maple. Next, this numerical solution of λ_{eff} can be used in Eq. A.31. In Fig.

A.6, the different combinations of λ_e and λ_i resulting in a constant λ_{eff} are shown. Furthermore, we can calculate the angular distribution $A(\mu)$ that belongs to the found value of λ_{eff}. This angular distribution can be written in normalized (at $\mu = 1$) form as:

$$A^N(\mu) = \frac{\left(\frac{1}{\lambda_e} + \frac{1}{\lambda_i} - \frac{1}{\lambda_{eff}}\right)}{\left(\frac{1}{\lambda_e} + \frac{1}{\lambda_i} - \frac{\mu}{\lambda_{eff}}\right)} \tag{A.36}$$

This angular distribution function is plotted in Fig. A.7 for different combinations of λ_e and λ_i. This plot shows that the found solution is one that resembles the broadening of the angular distribution, when one increases the (possible) number of elastic scattering events, before an electron is lost in an inelastic scattering event. Although the above equations are a solution of the Boltzmann equation, they are only valid for a certain type of angular distribution for given values of λ_e and λ_i. This makes them useless if we want to apply special boundary conditions due to Schottky barriers, include different scattering lengths in the base and take care of the interfacial scattering. For this general case, the only method left is to solve the entire problem with a numerical procedure. See also [100] for other analytical/numerical methods of solving Eq. A.30.

A.2.2 Numerical solution of the 3-D Boltzmann equation

Having derived the Boltzmann equation, we have to solve it. It is however not trivial to find a general solution of Eq. 2.45 for arbitrary boundary conditions and locally different scattering parameters in the base. So we use the following numerical solving procedure. Essential is that we split Eq. 2.45 into two equations, one for electrons moving in the positive x-direction ($f^{>}(x, \mu)$) and one for electrons moving

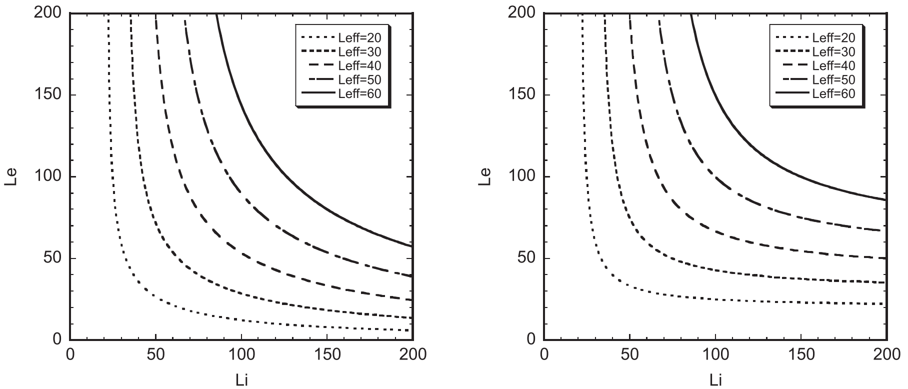

Figure A.6: *On the left the iso-λ_{eff} plot for the above mentioned 3-D case. On the right, the same but for the 1-D case ($\lambda_{eff}^{-1} = \lambda_i^{-1} + \lambda_e^{-1}$).*

in the negative x-direction ($f^<(x,\mu)$):

$$\mu\frac{\partial f^>(x,\mu)}{\partial x} = -\left[\frac{1}{\lambda_e}+\frac{1}{\lambda_i}\right] f^>(x,\mu) + \frac{1}{2\lambda_e}\int_0^1 f^>(x,\mu)d\mu + S^>(x), \tag{A.37}$$

$$\mu\frac{\partial f^<(x,\mu)}{\partial x} = -\left[\frac{1}{\lambda_e}+\frac{1}{\lambda_i}\right] f^<(x,\mu) + \frac{1}{2\lambda_e}\int_{-1}^0 f^<(x,\mu)d\mu + S^<(x). \tag{A.38}$$

Here, $S^>(x)$ and $S^<(x)$ are seen as backward source terms that represent in-scattering of electrons that after an elastic scattering event move in the opposite direction (from moving to the left to moving to the right, or vise versa). The $S^>(x)$ and $S^<(x)$ are defined as:

$$S^>(x) = \frac{1}{2\lambda_e}\int_{-1}^0 f^<(x,\mu)d\mu, \tag{A.39}$$

$$S^<(x) = \frac{1}{2\lambda_e}\int_0^1 f^>(x,\mu)d\mu. \tag{A.40}$$

In order to solve the set of coupled equations (A.37-A.40) for a single base layer of thickness W, we start with Eq. A.37 and solve it numerically for $x = 0 \rightarrow W$ without taking into account $S^>(x)$, because it is unknown, but in every step calculating

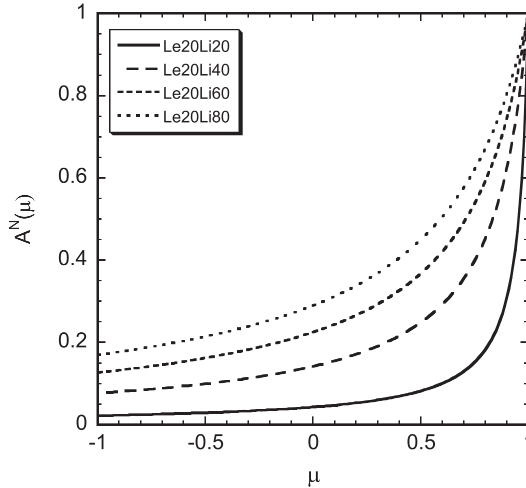

Figure A.7: *The normalized angular distribution $A^N(\mu)$ for 4 different combinations of λ_i(=20, 40, 60 and 80Å) and λ_e(=20Å).*

$S^<(x)$ and storing it into the computer memory. Next, we use Eq. A.38 to calculate $f^<(x,\mu)$ for $x = W \to 0$ while now using the previously stored values of $S^<(x)$ and calculating $S^>(x)$ at all positions. After the whole loop ($x = 0 \to W \to 0$), the procedure is repeated until a self-consistent solution is obtained.
In order to numerically solve Eq. A.37 we first discretize μ into n directions ($\mu_{1..n}$), with $n = 64$, so that $f^>(x,\mu)$ becomes $f_i^>(x)$. We can then convert the integral term in Eq. A.37 into a sum as:

$$\int_0^1 f^>(x,\mu)d\mu \approx \sum_{i=1..n} a_i f^>(x,\mu_i) = \sum_{i=1..n} a_i f_i^>(x), \tag{A.41}$$

in which a_i are the coefficients for numerical integration. We have used a trapezoid like integration rule with optimally chosen μ values and $a_1 = \mu_1 + (\mu_2 - \mu_1)/2$, $a_i = (\mu_{i+1} - \mu_{i-1})/2$ and $a_n = (\mu_n - \mu_{n-1})/2$. Now Eq. A.37 can be written in a matrix form, in which the numerical integration coefficients are the elements of a matrix:

$$\begin{bmatrix} \mu_1 \\ \mu_2 \\ \vdots \\ \mu_n \end{bmatrix} \cdot \frac{\partial}{\partial x} \begin{bmatrix} f_1^>(x) \\ f_2^>(x) \\ \vdots \\ f_n^>(x) \end{bmatrix} = -\left(\frac{1}{\lambda_e} + \frac{1}{\lambda_i}\right) \begin{bmatrix} f_1^>(x) \\ f_2^>(x) \\ \vdots \\ f_n^>(x) \end{bmatrix} + \frac{1}{2\lambda_e} \begin{bmatrix} a_1 & a_2 & \cdots & a_n \\ a_1 & a_2 & \cdots & a_n \\ \vdots & \vdots & \ddots & \vdots \\ a_1 & a_2 & \cdots & a_n \end{bmatrix} \begin{bmatrix} f_1^>(x) \\ f_2^>(x) \\ \vdots \\ f_n^>(x) \end{bmatrix} + \begin{bmatrix} S_1^>(x) \\ S_2^>(x) \\ \vdots \\ S_n^>(x) \end{bmatrix} \tag{A.42}$$

or in a more compact notation:

$$\frac{\partial}{\partial x} \begin{bmatrix} f_1^>(x) \\ f_2^>(x) \\ \vdots \\ f_n^>(x) \end{bmatrix} = \left[\mu^{-1}\right] \left(([W_{in}] - [W_{out}]) \begin{bmatrix} f_1^>(x) \\ f_2^>(x) \\ \vdots \\ f_n^>(x) \end{bmatrix} + \begin{bmatrix} S_1^>(x) \\ S_2^>(x) \\ \vdots \\ S_n^>(x) \end{bmatrix} \right), \tag{A.43}$$

in which we have introduced the in- and out-scattering matrices $[W_{in}]$ and $[W_{out}]$, respectively, defined as: $[W_{in}] = (2\lambda_e)^{-1} [M_{int}]$ and $[W_{out}] = (\lambda_e^{-1} + \lambda_i^{-1}) [M_{id}]$, with the identity matrix $[M_{id}]$ and the special integration matrix $[M_{int}]$:

$$[M_{int}] = \begin{bmatrix} a_1 & a_2 & \cdots & a_n \\ a_1 & a_2 & \cdots & a_n \\ \vdots & \vdots & \ddots & \vdots \\ a_1 & a_2 & \cdots & a_n \end{bmatrix}. \tag{A.44}$$

The next step is to discretize x, so that the differential can be written as the difference of $f_\mu^>(x)$ and $f_\mu^>(x + dx)$, in which care should be taken that dx is small enough to

justify this procedure (in our case $dx = 0.1$ Å). This results in the following iteration formulas:

$$\begin{bmatrix} f_1^> \\ f_2^> \\ \vdots \\ f_n^> \end{bmatrix}_{x+dx} = \begin{bmatrix} f_1^> \\ f_2^> \\ \vdots \\ f_n^> \end{bmatrix}_{x} + dx \left[\mu^{-1}\right] \left(([W_{in}] - [W_{out}]) \begin{bmatrix} f_1^> \\ f_2^> \\ \vdots \\ f_n^> \end{bmatrix}_{x} + \begin{bmatrix} S_1^> \\ S_2^> \\ \vdots \\ S_n^> \end{bmatrix}_{x} \right), \tag{A.45}$$

$$\begin{bmatrix} S_1^< \\ S_2^< \\ \vdots \\ S_n^< \end{bmatrix}_{x+dx} = [W_{in}] \begin{bmatrix} f_1^> \\ f_2^> \\ \vdots \\ f_n^> \end{bmatrix}_{x}, \tag{A.46}$$

and similarly for $f^<$ and $S^>$, which are used in the calculations for $x = W \rightarrow 0$.
In order to model elastic interface scattering, that occurs at the metal-metal *as well as at the silicon-metal interfaces*, we will introduce a parameter D that represents the interface diffusivity. From the incident distribution of electrons, a fraction $(1 - D)$ crosses the interface without being scattered, while a fraction D will be scattered elastically. The elastic interface scattering is assumed to be isotropic, such that a fraction $D/2$ of the electrons will still move in the forward direction, but the other $D/2$ will be scattered in the backward direction, so that we have to incorporate these as a backward source. In the matrix formalism developed above, this can be written as:

$$\begin{bmatrix} f_1^> \\ f_2^> \\ \vdots \\ f_n^> \end{bmatrix}_{\substack{layer \\ i+1}} = (1 - D)\,[M_{id}] \begin{bmatrix} f_1^> \\ f_2^> \\ \vdots \\ f_n^> \end{bmatrix}_{\substack{layer \\ i}} + \frac{D}{2}\,[M_{int}] \begin{bmatrix} f_1^> \\ f_2^> \\ \vdots \\ f_n^> \end{bmatrix}_{\substack{layer \\ i}} + \begin{bmatrix} S_1^> \\ S_2^> \\ \vdots \\ S_n^> \end{bmatrix}_{\substack{layer \\ i}}, \tag{A.47}$$

$$\begin{bmatrix} S_1^< \\ S_2^< \\ \vdots \\ S_n^< \end{bmatrix}_{\substack{layer \\ i}} = \frac{D}{2}\,[M_{int}] \begin{bmatrix} f_1^> \\ f_2^> \\ \vdots \\ f_n^> \end{bmatrix}_{\substack{layer \\ i}}, \tag{A.48}$$

and again similarly for $f^<$ and $S^>$, which are used in the calculations for $x = W \rightarrow 0$.

A.2.3 1-D transport model including spin-wave scattering.

Until now, we have used equations (Eq. 4.6 and 4.7) to compare our experiments with, but it appears impossible to explain the reduction of magnetocurrent due to

spin-waves with these formula. Therefore, we first go back to the basis of this model and explain how to include spin-wave scattering.

If we describe the number of hot-electrons ($f(x)$) at position x inside the base of the spin-valve transistor with the 1-directional Boltzmann equation (Eq. 2.47):

$$\frac{\partial f(x)}{\partial x} = -\left[\sum_s \frac{1}{\lambda_s}\right] f(x) \tag{A.49}$$

We obtain as solution $f(x) = f(0)\exp(-x/\lambda_0)$, which describes an exponential attenuation with a characteristic length of λ_0. The characteristic length in this model is simply the sum of all the different scattering possibilities (i.e. $\lambda_0^{-1} = \sum_s[\lambda_s^{-1}]$), because every scattering events is assumed to remove a hot-electron.
If we now want to include spin-wave scattering, in which the electron is not lost, but added to the other spin-channel, we have to write $f(x)$ into a spin-up part ($f^{\uparrow}(x)$) and spin-down part ($f^{\downarrow}(x)$). Next, we have to model the spin-wave scattering by a term that removes the electron from the spin-channel $\uparrow$ ($\downarrow$), which can be written as:$-(1/\lambda_{SW})f^{\uparrow(\downarrow)}(x)/$ and a term that adds a fraction β of these spin-wave scattered electrons to the other spin-channel (i.e. $+(\beta/\lambda_{SW})f^{\uparrow(\downarrow)}(x)$, so that the Boltzmann equation for both spin-channels can be written as:

$$\frac{\partial f^{\uparrow}(x)}{\partial x} = -\left[\frac{1}{\lambda_0^{\uparrow}} + \frac{1}{\lambda_{SW}^{\uparrow}(T)}\right] f^{\uparrow}(x) + \frac{\beta}{\lambda_{SW}^{\downarrow}(T)} f^{\downarrow}(x) \tag{A.50}$$

$$\frac{\partial f^{\downarrow}(x)}{\partial x} = -\left[\frac{1}{\lambda_0^{\downarrow}} + \frac{1}{\lambda_{SW}^{\downarrow}(T)}\right] f^{\downarrow}(x) + \frac{\beta}{\lambda_{SW}^{\uparrow}(T)} f^{\uparrow}(x) \tag{A.51}$$

As written down here, at T=0K, all the scattering is described by $\lambda_0^{\uparrow}$ and $\lambda_0^{\downarrow}$. And the temperature dependence in the attenuation is described by $\lambda_{SW}^{\uparrow(\downarrow)}(T)$ from which only a fraction β is contributing to the other spin-channel. The reason we have introduced the fraction β is that not after every spin-wave scattering event, the spin-flipped electron will have enough energy and the correct momentum to be collected.
When these coupled linear differential equations are used to describe the electron transport in the bulk of the spin valve, we can make a similar model as Eq. 2.52 and 2.53, but with spin-wave scattering included.
In order to solve the coupled differential equations, we use MAPLE and this result in very long (but still analytic) formula for the collector current and the magnetocurrent. A nice feature of this analytical solution is that it can be copied into a Labview program. With this program we can change scattering parameters and see how it influences the thickness and temperature dependence of the collector current.

A.3 Magnetic switching of a spin valve

Essential for the GMR effect on which the spin-valve transistor and normal spin valves are based, is that the magnetization of adjacent magnetic layers can be controlled between the parallel and anti-parallel state. This can be done by applying an external magnetic field, on which the spin valve reacts. In this section we will briefly describe the underlying magnetics, that describe this switching behavior.
With the Stoner-Wolhfarth theory, the switching of two different magnetic layers, as found in a spin valve, with anisotropy and coupling can be described relatively easy. When a external magnetic field H (under an angle ϕ) is applied in such a system, the two magnetic layers will try to minimize their total energy by rotating [2] their magnetization. This total energy consists of several contributions:

$$E_{total} = E_{zeeman} + E_{coupling} + E_{anisotropy} \tag{A.52}$$

Which can be written in the case of a spin valve with two magnetic layers as (per unit area in CGS !):

$$E_{zeeman} = -t_1 M_1^s H \cos(\phi - \theta_1) - t_2 M_2^s H \cos(\phi - \theta_2) \tag{A.53}$$

$$E_{coupling} = -A_{12} \cos(\theta_1 - \theta_2) \tag{A.54}$$

$$E_{anisotropy} = t_1 K_1 \sin^2(\theta_1) + t_2 K_2 \sin^2(\theta_2) \tag{A.55}$$

The thickness of magnetic layer 1 is denoted by t_1, its saturation magnetization by M_1^s (508, 1729, 1434, 745 erg/Oe/cm^3 for Ni, Fe, Co and NiFe respectively), θ_1 is the angle with the x-axis and similar for layer 2. The coupling energy A_{12} between two magnetic layers can be either positive (ferromagnetic coupling) or negative (anti-ferromagnetic coupling) and depends on the thickness of the interlayer (spacer). Furthermore, the magnetization has a favorable direction (here x-direction) due to the elements shape or crystal structure, this is expressed by the anisotropy constant K.
In spin valves like NiFe/Au/Co, the two magnetic layers have a different anisotropy (K), and therefore they switch at a different field. Although there is generally also some coupling (A_{12}) between the layers, the anisotropy energy is much larger, and so the switching properties are determined by how the Zeeman energy interacts with the anisotropy energy. When the magnetic field is applied in the x-direction (easy-axis), every layer switches independently at its own coercive field, which dependent on the individual coercivity (K) of the layer, as shown for NiFe/Au/Co in Fig. A.8.
In most spin valves the hard magnetic layer is pinned, this means that it is coupled to an anti-ferromagnetic layer, like FeMn or NiO. This results in a case where the anisotropy energy for the Co layer is very high, and so the Co layer hardly doesn't

2 The magnetization remains in the plane, due to shape anisotropy. An other mechanism to reduce the energy is by breaking up into a domain pattern, but this can not be modelled in a Stoner-Wolhfarth model.

rotate at all (it is also possible to include the pinning of the Co layer by adding an extra energy contribution in the Stoner-Wolhfarth model, see [101]), while the NiFe layer 'freely' follows the applied field.
With the above model, the switching properties of anti-ferromagnetically coupled GMR multilayers can also be explained, although we have to use t_1=x/2 and t_2=x/2 to model a (NiFe(xÅ)/Au)$_n$ multilayer. In anti-ferromagnetically coupled layers there are mainly two energy contributions: the Zeeman energy and the coupling energy. When there is no applied field, these layers are oppositely magnetized (because A_{12} is negative). Applying a field will force the two magnetic layers to be more parallel. In Fig. A.9, this gradual rotation of the two magnetic layers versus magnetic field and the resulting MR are shown.

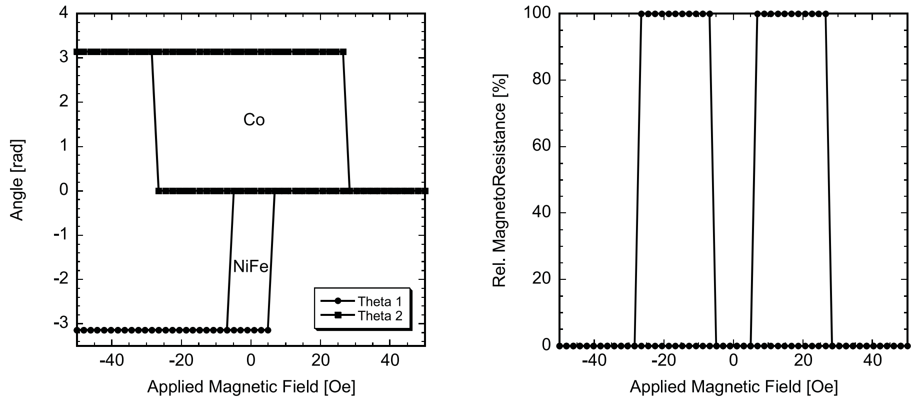

Figure A.8: *On the left, the angle θ_1 and θ_2 vs. the applied magnetic field in a NiFe(30Å)/Au/Co(30Å) spin-valve ($K_1^{NiFe} = 2 \cdot 10^3 erg/cm^3$ and $K_2^{Co} = 2 \cdot 10^4 erg/cm^3$. On the right, the hereby belonging calculated normalized CIP-MR($= 1/2 - 1/2\cos(\theta_1 - \theta_2)$) vs. the applied magnetic field.*

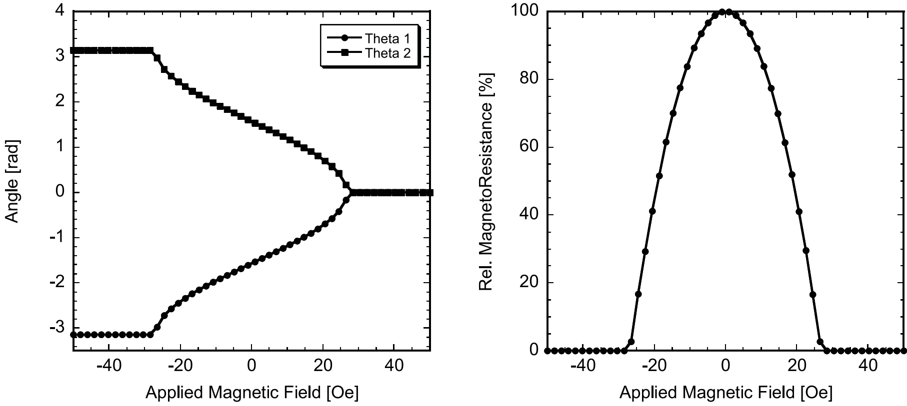

Figure A.9: *On the left, the angle θ_1 and θ_2 vs. the applied magnetic field in a (NiFe (30Å/Au)$_n$ multilayer with $A_{12} = -1.5 \cdot 10^{-3} erg/cm^2$. On the right, the hereby belonging calculated normalized CIP-MR vs. the applied magnetic field.*

A.4 Processing schemes

In this section of the appendix, all the used cleanroom processing steps to make a spin-valve transistor are summarized with a short description.

Silicon wafer oxidation

- Standard wafer cleaning
  Standard procedure consisting of: 10 min HNO_3 100% at room temperature, De-ionized and cleaned water (DI) rinse, 10 min HNO_3 70% at 95°C, DI rinse
- Dry oxidation
  1 hour O_2 at 950°C and 30 min N_2 at 1150°C, resulting in a flat ≈ 30nm thick oxide.
- Photoresist protection
  Thick 3.5μm photoresist (OiR 908/35 from Olin Microelectronic materials) with 20 min bake at 95°C.
- Sawing into pieces
  Wafers are sawn into 17.9x11.9mm^2 or 20.9x11.9mm^2 for use on the bonding robot.

Backside protection of the collector wafer

As collector wafers we use double sided polished (DSP) wafers on which after the thermal oxide and before photoresist protection a chemically inert Si_3N_4 can be

deposited by PECVD on the backside. This prevents the collector wafer from being etched away during the TMAH thinning stage.

- PECVD of Si_3N_4
  During 60 min at a power of 60W (LF) and at pressure of 650mTorr at 300°C, we add 2000 sccm of 2% SiH_4/N_2 and 6 sccm of NH_3, resulting in $\approx 1\mu$m of Si_3N_4.

Silicon cleaning procedure

- 5 min HNO_3
  This removes the protecting photoresist and all organic contaminations.
- 8 min DI
  This long water rinse is needed to prevent cross-contamination between HNO_3 and HF
- 1 min HF 1%
  This HF etch removes only the $\approx$ 2nm of native oxide on the sides of the two wafers, and on all the Si particles that emerged from the sawing.
- 15 sec DI
- 8 min TMAH 5% at 85°C.
  TMAH is an IC-compatible anisotropic Si etchant, and is very selective on SiO_2. This step etches all the Si particles and the sides at a rate of $\approx 1\mu m/min$.
- 3 min DI
- 1 min HF 50%
  With this HF etch all SiO_2 is etched away, and a pure hydrogen-terminated Si surface is obtained. HF 50% is used to have the highest purity.
- 15 sec DI
- N_2 dry

Bonding

- Put cleaned wafers on robot with vacuum tweezers from the back
  It's not allowed to handle the samples with a normal pair of tweezers, because this will touch (and damage) the silicon surface that will be bonded.
- Protect collector wafer with the small shutter
- Put robot in the load-lock of the MBE system and pump for at least 3 hours.
  The pressure in the load-lock should at least be less than $1 \cdot 10^{-6}$ torr before the robot can be transferred to the deposition chamber.
- Transfer robot to the main chamber

- Heat-up the effusion cells and turn on the e-gun
- Deposit the layers of the spin-valve on the emitter wafer
- Trigger robot to open the shutter
  (The next layer will be grown on both substrates at the same time)
- Deposit the bond layer
- Trigger robot to move the two wafers together, resulting in the bond
- Cool down the effusion cells and turn off the e-gun
- Remove robot from the system, remove the sample and rewind the robot.
- Pump down the load-lock.

TMAH thinning down

- BHF dip
  To remove native oxide from the wafers, so that the TMAH etch can start easily and uniform.
- DI dip
  In order to prevent cross-contamination of the TMAH and the BHF, what results in a lower etchrate and a black surface while etching.
- 6 hours of TMAH 10% at 85°C.

Emitter photoresist

- 1 min bake at 95°C
  To remove water so that the photoresist sticks better.
- spin HMDS for 20 sec at 4000 rpm.
  To promote the adhesion of the photoresist to the wafer.
- spin photoresist (OiR 907/12) for 20 sec at 4000 rpm.
  Positive photoresist of $\approx 1.2\ \mu$m thick.
- 1 min pre-exposure bake at 95°C.
  To evaporate the solvent in the photoresist.
- Expose 4 seconds (integrated) in contact mode (align separation 46) with mask 1 (see Fig. A.10).
  Exposing the photoresist everywhere except where the oxide of the SOI wafer should remain to form the emitter.
- 1 min post-exposure bake at 120°C.
  In order to brake the exposed polymers in the photoresist.
- 1 min developing in OPD 4262 (positive resist developer from Arch chemicals).
  Removes the exposed photoresist, and leaves the unexposed.

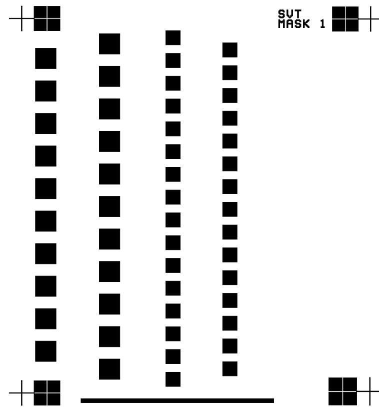

Figure A.10: *Mask 1: Emitter definition*

- DI rinse and spin dry.
- 20 min bake at 120°C.
  To harden the photoresist against a 20 min BHF etch in the next step.

Emitter oxide etch

- 20 min BHF.
  To etch through the SOI oxide of about 0.5μm and leave the photoresist
- DI rinse.
- Strip the photoresist with acetone, so that only the oxide under it is left
- DI rinse and spin dry.

Emitter etch

- 30 sec BHF.
  To remove native oxide, so that the TMAH etching will start properly.
- DI dip
- +3 min of TMAH 10% at 85°C. Etch through the 2.5μm Si device layer of the SOI wafer, while leaving the emitters which are protected by the oxide. The etch stops on the metallic base and should be stopped 20 seconds after reaching the metal layer.
- DI rinse and spin dry.

Base photoresist

- 1 min bake at 95°C.
- spin HMDS for 20 sec at 4000 rpm.
- spin photoresist (Oil 907/12) for 20 sec at 4000 rpm.
- 1 min pre-exposure bake at 95°C.
- Expose 4 seconds (integrated) in contact mode (align separation 46) with mask 2 (see Fig. A.11).
  Exposing the photoresist everywhere except where the base should remain in the metal layer.

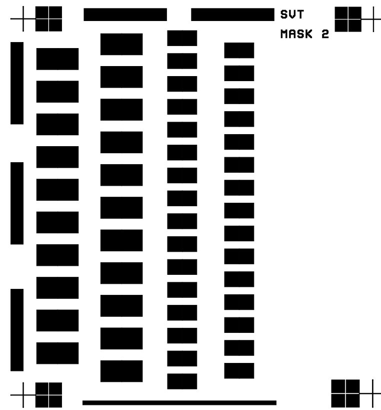

Figure A.11: *Mask 2: Base definition*

- 1 min post-exposure bake at 120°C.
- 1 min developing in OPD 4262.
- DI rinse and spin dry.
- 20 min bake at 120°C.
  To harden the photoresist against the ion beam in the next step.

IBE etch of the base

- mount sample on 3"-wafer with thermally conducting paste and 'vacuum' compatible adhesive tape.
- 20 min ion beam etch
  IBE for 20 min with an acceleration voltage of 250V and a current of 5mA and an argon flow of 300 resulting in a pressure of $5 \cdot 10^{-4}$bear.

- 2.5 min technical acetone + 2.5 min MOS (ultra pure) acetone in an ultrasonic bath
  To remove photoresist and thermally (and electrically $\rightarrow$ bad for the collector properties) conductive paste, first in normal acetone after that in a second clean beaker with ultra pure acetone.

- DI rinse and spin dry

Repairing process

By etching the metallic base with an ion beam, we damage the underlying silicon, this results in very bad diode characteristics (it even looks almost like an ohmic contact directly after the ion beam etch). This can be improved to almost a perfect diode by etching the damaged silicon away with TMAH, as done in the repairing process.

- 30 sec BHF + DI dip.
  To de-oxidize the silicon that has to be etched away. DI dip is important to prevent cross-contamination.

- 2 min TMAH 10% at 85°C + DI dip
  This step etches the damaged silicon and doesn't etch the metallic base. (when TMAH doesn't start: DI dip and put for another 30 sec in the BHF and clean it in a short DI dip before trying to start the TMAH again, sometimes this is needed several times).

- 30 sec BHF + DI dip
  De-oxidizes also those parts that didn't work the first time.

- 1 min TMAH 10% at 85°C
  Now really all the bad silicon is etched away, with this 2-step procedure diodes were repaired downto a leakage current level of $\approx 1.0 \cdot 10^{-10} A$ for the Au-Si collector barrier at RT.

- DI rinse and spin dry

Emitter + collector contacts photoresist

- 1 min bake at 120°C.
  This higher temperature will result in a better sticking, which is important at the sides of the holes that will be made in the emitter oxide.

- spin HMDS for 20 sec at 4000 rpm.

- spin photoresist (OiR 907/12) for 20 sec at 4000 rpm.

- 1 min pre-exposure bake at 95°C.

- Expose 4 seconds (integrated) in contact mode (align separation 46) with mask 3 (see Fig. A.12).

Exposing only the photoresist where there should come holes to make a metallization.

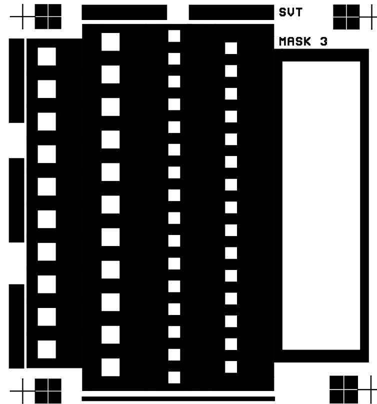

Figure A.12: *Mask 3: Emitter + Collector contacts.*

- 1 min post-exposure bake at 120°C.
- 1 min developing in OPD 4262
- DI rinse and spin dry.
- 20 min bake at 120°C.
  To harden the photoresist against a 20 min BHF etch in the next step.

Emitter + collector metallization

- 20 min BHF.
  To etch a small hole through the oxide on top of the emitter to make an ohmic contact.
- DI rinse and spin dry.
- Sample into sputtering system (sputterke)
- Deposit 15nm Cr and 100nm Au.
  At 200W DC and an Ar pressure of $\approx 7.5 \cdot 10^{-3}$mbar, Cr is deposited during 1 min and Au for 2.5 min.
- 2.5 min technical acetone + 2.5 min MOS acetone in an ultrasonic bath.
  Lift-off of the metallization where there was photoresist under the metal. The emitter and collector contacts are left.
- DI rinse and spin dry.

PCB mounting and wirebonding

- clean PCB with abrasive paper and make it dust free afterwards.
- glue sample on the PCB with acrylate glue.
- wirebond emitter and collector contacts with aluminium wires.
- wirebond base contacts with gold wires.
  Using aluminium wires results in a bad diode, because the wirebonding will always punch through the base, and this results in too much leakage current when a low Schottky barrier material, like Al, is used.

A.5 Sample overview

Sample	Emitter	Base (material + thickness in Å)	Collector
SVTK1	Si (100)	Pt Au Au 40 20 20	Si (111)
SVTK6	SOI	Pt Au Au 40 20 20	Si (100)
OSVT10	SOI	Au Au 30 30	Si (100)
OSVT15	SOI	Pt Cu Cu 30 20 20	Si (100)
SVTR8	Si (100)	Pt NiFe Au Co Au Au 20 60 35 30 20 20	Si (111)
RSVTN1	SOI	Pt NiFe Au Co Au Au 30 30 43.5 30 21.8 21.8	Si (100)
RSVTN2	SOI	Pt NiFe Au Co Au Au 30 40 43.5 30 21.8 21.8	Si (100)
RSVTN3	SOI	Pt NiFe Au Co Au Au 30 60 43.5 30 21.8 21.8	Si (100)
RSVTN4	SOI	Pt NiFe Au Co Au Au 30 20 43.5 30 21.8 21.8	Si (100)
RSVTN5	SOI	Pt NiFe Au Co Au Au 30 50 43.5 30 21.8 21.8	Si (100)
RSVTN6	SOI	Pt NiFe Au Co Au Au 30 70 43.5 30 21.8 21.8	Si (100)
RSVTN7	SOI	Pt NiFe Au Co Au Au 30 30 43.5 40 21.8 21.8	Si (100)
RSVTN8	SOI	Pt NiFe Au Co Au Au 30 30 43.5 20 21.8 21.8	Si (100)
RSVTN9	SOI	Pt NiFe Au Co Au Au 30 30 43.5 50 21.8 21.8	Si (100)
RSVTN10	SOI	Pt NiFe Au Co Au Au 30 30 43.5 10 21.8 21.8	Si (100)
RSVTN11	SOI	Pt NiFe Au Co Au Au 30 100 43.5 30 21.8 21.8	Si (100)
RSVTN12	SOI	Pt NiFe Au Co Au Au 30 10 43.5 30 21.8 21.8	Si (100)
RSVTN13	SOI	Pt NiFe Au Co Au Au 30 0 43.5 30 21.8 21.8	Si (100)

(SOI stands for Silicon On Insulator, with a Si (100) device layer.)

A.6 Material parameters

Metal	Si	Ge	GaAs
Ag	0.78	0.54	0.88
Al	0.72	0.48	0.80
Au	0.80	0.59	0.90
Cr	0.61		
Cu	0.58	0.52	0.82
Hf	0.58		0.72
Mg	0.40		
Mo	0.68		
Ni	0.61	0.49	
Pd	0.81	0.38	
Pt	0.90		0.84
Ti	0.50		
W	0.67	0.48	0.80

Table A.1: *The Schottky barrier heights in eV for various metal contacts on Silicon, Germanium and Gallium Arsenide [47]*

Summary

This thesis discusses research on the hot-electron transport in the spin-valve transistor (SVT). This 3-terminal device consists of a silicon emitter and collector with in between a base consisting of magnetic (NiFe and Co) and non-magnetic (Au) metal layers, a so-called spin-valve multilayer. Furthermore, the base includes thin layers of Pt and Au to form two different Schottky barriers with the Si emitter and collector.
The collector current is dependent on the amount of current that is injected from the emitter into the Pt/NiFe/Au/Co/Au base, and on the magnetic state of the spin-valve multilayer. When the NiFe and Co layers are magnetized in the same direction (parallel), more collector current is measured, than when the layers are magnetized oppositely (anti-parallel).
As described in this thesis, the spin-valve transistor can operate at room temperature and shows a large relative change in collector current (magnetocurrent $> 300\%$) within small magnetic fields of only some Oe's. Therefore, the spin-valve transistor is extremely suited to measure magnetic fields.
In the introduction (chapter 1), a brief overview of the spin-electronic research field is given, in which the spin-valve transistor is one of the promising devices. In this chapter, materials and devices are discussed in which the electron properties (especially transport) are dependent on the spin-state (up/down).
In the 2nd chapter, the spin-dependent current transport in the spin-valve transistor is theoretically analyzed. In the first part, the electron transport over the two Schottky diodes is described. At the emitter side, the injected electrons pass over the first Schottky barrier and this results in *hot*-electrons with an energy of $q\phi_B + 2 \sim 3kT$ ($\approx$ 0.95eV for Si/Pt at T=300K) above the Fermi level. These electrons need to travel through the base, where they scatter spin-dependently. Only electrons that arrive with enough energy ($E > q\Phi_B$) and the right momentum (within the acceptance cone angle $\theta_c \approx 5°$) can finally come over the second Schottky barrier and contribute to the collector current.
The second part of this chapter deals with the various scattering mechanisms that change the energy and momentum of the hot-electrons. The main difference between the scattering of hot-electrons and conduction electrons at the Fermi-level is the possibility for hot-electrons to loose large parts of their excess energy by Stoner excitations (electron-electron interactions) and the availability of a larger empty (E, k) phase-space to scatter into. Next, the Boltzmann equation is used to calculate how elastic and inelastic scattering mechanisms affect the transport of the hot-electrons through the base. Because there is no electrical field in the base that helps the hot-electrons to move from the emitter to the collector, there is exponential attenuation in the base. In the magnetic layers, this exponential attenuation is spin-dependent, and therefore a large magnetocurrent is experimentally observed.
In chapter 3, an overview is given of the deposition system (MBE) that is used to grow the metallic layers in the base of the spin-valve transistor. In this system, metallic layers are deposited on two silicon substrates, after which these are moved to each

other, resulting in an in-vacuum metal bond of the two substrates with the metal layer in between. Next, these samples are lithographically processed and etched to obtain spin-valve transistors, which can be electrically characterized in the measurement setup.
In chapter 4, the device characteristics of experimental spin-valve transistors are analyzed. First, the I-V characteristics of single Schottky diodes are measured and agree well with the thermionic emission theory. After that, the hot-electron transport in metal base transistors is investigated. These transistors have only two non-magnetic metals in the base, so the influence of these two different Schottky barriers on the magnitude of the collector current can be studied. Analyzes show that the change of acceptance cone angle θ_c with hot-electron energy results in the observed increase of collector current with temperature. In the spin-valve transistor, the magnetic (NiFe and Co) layer thickness' are varied and the influence on the collector current and magnetocurrent and their temperature dependence is measured. At low temperatures (T=100K), the spin-dependent attenuation lengths for hot-electrons in NiFe ($\lambda^{\uparrow}$=43Å and $\lambda^{\downarrow}$=8Å) and the majority attenuation length in Co ($\lambda^{\uparrow}$=25Å) are extracted. At room temperature, additional thermal scattering in the bulk of the magnetic layers is observed and appears to be related to thermal spin-wave scattering that mixes the spin-up and spin-down electrons, resulting in a slight reduction of the magnetocurrent. From the variation of the collector current with temperature, the thermal spin-wave attenuation length in NiFe and Co (140Å and 270Å, respectively at room temperature) are deduced.
In chapter 5, the conclusions of this thesis are given and the possibilities to improve the spin-valve transistor in future research are discussed.

Résumé

Le travail accompli dans cette thèse a été consacré à l'étude du transistor à base de la vanne de spin, d'un point de vue aussi bien expérimental que théorique. Ce système à 3 bornes se compose d'un émetteur et d'un collecteur en silicium entre lesquels est insérée une base faite d'une série de couches magnétiques et non-magnétiques et qui joue le rôle de la vanne de spin. En opération normale, un courant constant est injecté entre l'émetteur de silicium et la base de Pt/NiFe/Au/Co/Au. Le courant du collecteur est fortement dépendant de l'orientation relative de l'aimantation de la couche magnétique douce (NiFe) par rapport à celle du Cobalt. En effet, un alignement parallèle des aimantations des 2 couches favorise le passage de plus de courant que dans l'état antiparallèle.
Comme indiqué dans cette thèse, un spin-valve transistor (SVT) capable de fonctionner à température ambiante a été mis au point. Avec des champs faibles (quelques Oersteds), il est possible d'obtenir un grand changement relatif du courant du collecteur (le magnétocourant > 300%). Par conséquent, tous ces avantages font du SVT un système potentiel dans des applications de détection des champs magnétiques.
Dans l'introduction (chapitre 1), un bref rappel sur l'électronique de spin est dressé. Dans ce domaine de recherche, dont le spin-valve transistor fait partie, les matériaux et leurs propriétés de transport sont étudiés pour leurs différences selon l'état de spin des électrons (haut et bas).
Dans le deuxième chapitre, une analyse théorique a été réalisée sur la dépendance en spin du transport des électrons dans le spin-valve transistor. La première partie analyse le transport des électrons dans les diodes Schottky, qui sont formées par la combinaison d'un émetteur, d'un collecteur de silicium et d'une base métallique. Du côté de l'émetteur, les électrons sont injectés au dessus de la première barrière Schottky, ce qui donne naissance à des électrons chauds avec une énergie de $q\Phi_B + 2 \sim$ 3kT ($\approx$ 0.95eV pour Si/Pt à T=300K) au dessus du niveau de Fermi. Ces électrons doivent traverser la base où ils seront l'objet de diffusions dépendant de leurs états du spin. Seuls les électrons qui arrivent avec une énergie suffisante ($E > q\Phi_B$) et un moment cinétique bien défini (compris dans l'angle du cône d'acceptation $\theta_c \approx 5^\circ$) peuvent passer au dessus de la deuxième barrière Schottky et contribuer au courant du collecteur. Dans la deuxième partie de ce chapitre, les mécanismes de diffusion capables d'influencer l'énergie et le moment des électrons chauds sont étudiés. La principale différence entre la diffusion des électrons sur le niveau de Fermi et les électrons chauds réside dans la possibilité de perdre une part considérable d'excès d'énergie par des excitations Stoner (interaction électron-électron) et la disposition d'un espace de phase (E, k) plus important pour la diffusion. Puis, l'équation de Boltzmann est utilisée pour calculer comment les diffusions élastiques et inélastiques affecteront le transport des électrons chauds à travers la base. A cause de l'inexistence d'un champ électrique dans la base (lequel devrait permettre aux électrons un parcours plus facile de l'émetteur au collecteur) le courant se trouve alors fortement atténué (exponentiellement). Dans les couches magnétiques, cette atténuation exponentielle est dépendante du spin et résulte

d'un magétocourant géant.
Dans le chapitre 3, une rapide description est présentée sur la machine de dépôt (évaporation par jet moléculaire). Celle-ci est utilisée pour croître les couches métalliques qui sont supposées constituer la base du SVT. Avec cette machine, le dépôt s'effectue sur deux substrats qui sont rapprochés puis collés sous vide avec la couche métallique. Après un processus de photolithographie et de gravure chimique, le SVT est obtenu ; il fera ensuite l'objet d'analyses électriques.
Dans le chapitre 4, les caractéristiques de SVT sont analysées expérimentalement. Dans une première phase, la dépendance I-V d'une simple diode Schottky semble être en bon accord avec le théorie de l'émission thermionique. Plus loin, le transport des électrons dans les transistors de base métallique a été examiné. Ces transistors ne possèdent que deux métaux non-magnétiques dans la base ; ils permettent donc d'étudier l'influence des deux barrières Schottky sur la grandeur du courant du collecteur. Ces analyses ont prouvé que le changement d'angle d'acceptation θ_C avec l'énergie de l'électron chaud résulte d'une augmentation du courant du collecteur avec la température. Dans le SVT, on a varié l'épaisseur des couches magnétiques (NiFe et Co) et mesuré leurs influences sur le courant du collecteur, sur le magnétocourant et leurs dépendances avec la température. A basse température (T=100K), la dépendance en spin du parcours d'atténuation a été déduite pour les électrons chauds en NiFe ($\lambda^{\uparrow}$=43Å et $\lambda^{\downarrow}$=8Å) et pour les électrons majoritaires en Co ($\lambda^{\uparrow}$=25Å). A température ambiante, une diffusion additionnelle est observée dans le massif des couches magnétiques. Cette diffusion est liée aux ondes du spin thermiques qui mélangent les électrons spin-haut avec spin-bas et provoquent une petite baisse dans le magnétocourant. La variation du courant du collecteur, en fonction de la température, permet d'obtenir le parcours d'atténuation thermique de 140Å et 270Å respectivement pour NiFe et Co, à température ambiante.
Pour terminer, le dernier chapitre de cette thèse conclut par un bilan du travail mené sur l'étude de spin-valve transistor ainsi que sur les possibilités envisagées pour l'améliorer.

Samenvatting

In dit proefschrift wordt onderzoek op het gebied van het hete elektron transport in de spin-valve transistor beschreven. Dit device met 3 contacten bestaat uit een emitter en collector van silicium met daartussen een basis van dunne magnetische (NiFe en Co) en niet-magnetische metaal (Au) lagen, een zogenaamde spin valve multilaag. Ook wordt er in de basis gebruik gemaakt van Pt en Au metaallagen die, samen met het Si van de emitter en collector, twee verschillende Schottky barrières vormen.
De collector stroom is afhankelijk van de hoeveelheid stroom die vanuit de emitter in de Pt/NiFe/Au/Co/Au basis word geïnjecteerd, en van de magnetische toestand van de NiFe en Co lagen. Wanneer deze lagen in dezelfde richting (parallel) gemagnetiseerd zijn, zal er meer collector stroom worden gemeten dan wanneer de lagen tegenover gesteld (anti-parallel) gemagnetiseerd zijn.
De in dit proefschrift beschreven spin-valve transistor werkt op kamertemperatuur en laat een grote relatieve verandering van de collector stroom (magnetostroom $> 300\%$) in kleine magneet velden van enkele Oersted's zien. Hierdoor kan de spin-valve transistor goed worden gebruikt om magnetische velden te meten.
In de introductie (hoofdstuk 1), word een kort overzicht gegeven van het onderzoeksgebied dat zich richt op de spin-elektronica, waarbinnen de spin-valve transistor een van de veelbelovende devices is. In dit hoofdstuk worden materialen en devices besproken waarin de transport eigenschappen niet hetzelfde zijn voor de twee verschillende spin toestanden (omhoog/omlaag).
In het tweede hoofdstuk, wordt een theoretische beschrijving van het spin afhankelijke transport in de spin-valve transistor gegeven. In het eerste deel wordt het elektron transport over de twee Schottky diodes geanalyseerd. De geïnjecteerde elektronen gaan aan de emitter kant over de Schottky barrière, en dit resulteert in hete elektronen met een energie van $q\Phi_B + 2 \sim 3$kT ($\approx$ 0.95eV voor Si/Pt bij T=300K) boven het Fermi niveau. Deze elektronen moeten door de basis bewegen, waar ze spin afhankelijk worden verstrooid. Alleen elektronen met genoeg energie ($E > q\Phi_B$) en de juiste impuls (binnen de acceptatie kegel $\theta_c \approx 5^\circ$) kunnen over de tweede Schottky barrière komen en bijdragen aan de collector stroom.
Het tweede deel van dit hoofdstuk behandelt de verschillende verstrooiingsmechanismen die de energie en impuls van de hete elektronen veranderen. Het belangrijkste verschil tussen verstrooiing van elektronen op het Fermi niveau en hete elektronen is dat hete elektronen de mogelijkheid hebben om een groot deel van hun overtollige energie te verliezen door Stoner excitaties (elektron-elektron interacties). Verder is er een grotere (E, k) fase ruimte beschikbaar om in te verstrooien. Vervolgens wordt met behulp van de Boltzmann vergelijking berekend hoe elastische en inelastische verstrooiings-processen het transport van de hete elektronen door de basis beïnvloeden. Omdat er geen elektrisch veld in de basis is dat de hete elektronen helpt om van de emitter naar de collector te komen, valt de collector stroom exponentieel af. In de magnetische lagen is deze exponentiële afval spin afhankelijk en daarom wordt er een grote magnetostroom geobserveerd.

In hoofdstuk 3 wordt een korte beschrijving van de depositie machine (MBE) gegeven, die wordt gebruikt om de metaallagen in de basis van de spin-valve transistor te groeien. In dit systeem kan met behulp van een bondrobot op twee wafers tegelijk een metaallaag worden aangebracht. Door deze substraten daarna naar elkaar toe te brengen, ontstaat een metaalbinding tussen de twee silicium wafers. Na enkele photolithografie en ets stappen, kunnen uiteindelijk de spin-valve transistors elektrisch gekarakteriseerd worden.
In hoofdstuk 4, worden de elektrische eigenschappen van de spin-valve transistor geanalyseerd. Allereerst, worden de I-V karakteristieken van enkele Schottky diodes gemeten, die in goede overeenstemming zijn met de thermionische-emissie theorie. Daarna wordt het transport van hete elektronen in metaal basis transistoren onderzocht. Deze transistoren hebben maar twee niet-magnetische metalen in de basis, zodat de invloed van de twee verschillende Schottky barrières op de grote van de collector stroom bepaalt kan worden. Uit analyses blijkt dat de vergroting van de acceptatie kegel hoek met de hete elektronen-energie verantwoordelijk is voor het oplopen van de collector stroom met temperatuur. Door de magnetische (NiFe en Co) laagdiktes in de spin-valve transistor te varieren, is de invloed op de collector stroom, magnetostroom en de temperatuur-afhankelijkheid daarvan in kaart gebracht. Op lage temperaturen (T=100K) is de specifieke *spin afhankelijke* afval lengte voor hete elektronen in NiFe bepaald ($\lambda^{\uparrow}$=43Å en $\lambda^{\downarrow}$=8Å) en in Co is een meerderheids spin afval lengte van 25Å bepaald. Op kamer temperatuur is er additionele thermische verstrooiing door interacties van de hete elektronen met thermische spin-waves. Verstrooiing aan spin-waves resulteert in het mixen van de spin-omhoog en omlaag elektronen, en dit heeft een reductie van de magnetostroom als gevolg. Aan de hand van de temperatuurs-afhankelijkheid van de collector stroom is de thermische spin-wave afval lengte bepaald, welke op kamer temperatuur respectievelijk 140 en 270Å is voor NiFe en Co.
In hoofdstuk 5 worden de conclusies gegeven en de mogelijkheden bediscussieerd om in vervolg onderzoek de eigenschappen van de spin-valve transistor verder te verbeteren.

Acknowledgements

During the 4 years of my Ph.D. thesis, I have enjoyed working at two different laboratories. I would like to thank everyone from both the Information Storage Technology Group in Enschede and the Nanostructure and Magnetism group in Grenoble for their technical and scientific assistance. Many people have contributed to my research and have helped me to realize this thesis, therefore I would like to send my special thanks to:

- Prof. J.C. Lodder and Prof. Th.J.A. Popma for being my promotors. And of course Prof. A.V. Vedyayev, Dr. B. Dieny, Prof. R. Coehoorn, Prof. P. Woerlee and Prof. P.J. Kelly for being part of my committee.
- Cock Lodder for being my daily supervisor in Twente, taking care that everything remained on track.
- Bernard Dieny, for his hospitality during my visits at CEA/Grenoble. Together with Anatoly Vedyayev, many fruitfull discussions have lead to a better insight in the hot-electron transport in the spin-valve transistor.
- Ronnie Jansen for his careful proof-reading of my thesis and Abdellah Lisfi for his help with the résumé. Furthermore, I also would like to thank Douwe Monsma, Olaf van 't Erve, Sungdong Kim and Anil Kumar for their contributions on the experimental side of this thesis.
- Gerard Casali for his discussions and efforts to show the physical surroundings of Grenoble. Together with Jean-Christophe Pillet, Stephanne Auffret, Stephan Landis and Mathilde Cartier, it was very pleasant to work at the CEA.

And last but not least, I would like to thank my parents, my family and Béatrice for their general support during my thesis.

About the author

The author was born on April 16, 1974 in Enschede, the Netherlands. He graduated from the "Gemeentelijke Scholengemeenschap-Zuid"in Enschede, 1992. At the University of Twente, he studied applied physics, and after a practical training in Manchester on magnetic force microscopy, he obtained in 1997 his M.Sc. title with the thesis: "Realising Spin Valve and Metal Base Transistor Structures".
In May 1997 he continued his experimental work on the spin-valve transistor as a Ph.D. student in the Information Storage Technology Group of Prof. J.C. Lodder at the Mesa+ Research Institute. As part of the European HOTSEAMS project, the author has worked for about $1\frac{1}{2}$ years on the theoretical aspects of the spin-valve transistor in the laboratory of Dr. B. Dieny in Grenoble, France.
This Ph.D. thesis summarizes the principle results of 4 years of experimental and theoretical research on the hot-electron transport in the spin-valve transistor.

List of publications

Published articles:

- D.J. Monsma, R. Vlutters, T. Shimatsu, E.G. Keim, R.H. Mollema and J.C. Lodder, "Development of the spin valve transistor", *IEEE Trans. Magn.* **33**, 2495 (1997)

- D. J. Monsma, R. Vlutters and J. C. Lodder, "Room Temperature-Operating Spin-Valve Transistors Formed by Vacuum Bonding", *Science* **281**, 407 (1998)

- A. Vedyayev, N. Ryzhanova, R. Vlutters and B. Dieny , "Giant tunnel magnetoresistance in multilayered metal/oxide structures comprising multiple quantum wells", *J. Phys.: Condens. Matter* **10**, 5799 (1998)

- J.C. Lodder, D.J. Monsma, R. Vlutters and T. Shimatsu, "The spin-valve transistor: technologies and progress", *J. Mag. Magn. Mat.* **198-199**, 119 (1999)

- A. Vedyayev, N. Ryzhanova, R. Vlutters and B. Dieny, "Effect of interfacial scattering on the magnetoresistance of magnetic tunnel junctions", *Europhys. Lett.* **46**, 808 (1999)

- P.S. Anil Kumar, R. Jansen, O.M.J. van 't Erve, R. Vlutters, P. de Haan and J.C. Lodder, "Low-Field magnetocurrent above 200% in a spin-valve transistor at room temperature", *J. Mag. Magn. Mat.* **214**, L1 (2000)

- A. Vedyayev, N. Ryzhanova, R. Vlutters, B. Dieny and N. Strelkov, "Voltage dependence of giant tunnel magnetoresistance in triple barrier magnetic systems", *J. Phys.: Condens. Matter* **12**, 1797 (2000)

- R. Jansen, P.S. Anil Kumar, O.M.J. van 't Erve, R. Vlutters,P. de Haan and J.C. Lodder, "Thermal spin-wave scattering in hot-electron magnetotransport across a spin valve", *Phys. Rev. Lett.* **85**, 3277 (2000)

- P.S. Anil Kumar, R. Jansen, O.M.J. van 't Erve, R. Vlutters, S.D. Kim and J.C. Lodder, "300% magnetocurrent in a room temperature operating spin-valve transistor", *Physica C* **350** 166 (2001)

Accepted articles:

- O.M.J. van 't Erve, P.S. Anil Kumar, R. Jansen, S.D. Kim, R. Vlutters, J.C. Lodder, A.A. Smits and W.J.M. de Jonge, "Noise properties of the spin-valve transistor", *Sens. Actuators A.* (2001)

- S.D. Kim, O.M.J. van 't Erve, R. Jansen, P.S. Anil Kumar, R. Vlutters and J.C. Lodder, "Fabrication technology for miniaturazation of the spin-valve transistor", *Sens. Actuators A.* (2001)

- R. Jansen, O.M.J. van 't Erve, S.D. Kim, R. Vlutters, P.S. Anil Kumar and J.C. Lodder, "The spin-valve transistor: fabrication, characterization and physics", *J. Appl. Phys.* (2001)

- R. Vlutters, R. Jansen, O.M.J. van 't Erve, S.D. Kim, and J.C. Lodder, "Hot-electron transport through $Ni_{80}Fe_{20}$ in a spin-valve transistor", *J. Appl. Phys.* (2001)

Submitted aricles:

- R.Vlutters, O.M.J.van 't Erve, R. Jansen, S.D.Kim, J.C.Lodder, A.Vedyayev and B.Dieny, "Modeling of spin-dependent hot-electron transport in the spin-valve transistor"

- A. Vedyayev, R. Vlutters, N. Ryzhanova, J.C. Lodder and B. Dieny, "Interpretation of the magnetoresistance in doped magnetic tunnel junctions"

Conference presentations:

- R. Vlutters, D.J. Monsma and J.C. Lodder, "Latest developments of the spin-valve transistor", Symposium on Magneto-electronics in Regensburg on the 26th of March 1998. (invited)

- R. Vlutters, O.M.J. van 't Erve, P.S.A. Kumar, R. Jansen en J.C. Lodder, "Spin-valve transistors prepared by ultra-high vacuum bonding", SF2M autumn meeting in Paris on the 3rd of November 1999. (invited)

- R. Vlutters, O.M.J. van 't Erve, R. Jansen, S.D. Kim and J.C. Lodder, "Current transport in the Spin-Valve Transistor", Joint MMM-Intermag in San Antonio on the 9th of January 2001.